

*University of Bologna “Alma Mater Studiorum”, Naples “Federico II” and “Roma III”,
in convention with the “Istituto Nazionale di Geofisica e Vulcanologia”*



Ph.D Thesis in Geophysics

XXIV Cycle

04/04 - GEO/10

Year 2012

***Refined Estimation of
Earthquake Source Parameters:
Methods, Applications and Scaling Relationships***

Ph.D. Thesis of: *Antonella Orefice*

Coordinator

Prof. Michele Dragoni

Tutor

Prof. Aldo Zollo

Table of contents

Acknowledgments	7
Introduction.....	8
❖ Section A Seismic source theory	10
1. The representation theorem	10
2. Kinematic description of seismic source	11
2.1 Seismic spectrum to the high frequency	13
❖ Section B Frequency domain.....	15
Chapter 1 Modeling of displacement spectra	15
1.1 Spectral model	15
1.1.1 Source spectrum $S_0(\omega)$	15
1.1.2 Path attenuation model $Q(\omega)$	17
1.1.3 Site transfer function $R(\omega)$	18
1.1.4 Instrumental response curve $I(\omega)$	20
1.2 From spectral to seismic parameters.....	24
Chapter 2 Multi-step inversion of displacement spectra	26
2.1 Inversion strategy: iterative, multi-step approach	26
2.1.1 Influence of noise	28
2.2 Introduction to inverse theory.....	31
2.3 Non linear inverse problem	34
2.4 The Levenberg-Marquardt algorithm	37
Chapter 3 Applications	42
3.1 Resolution test: Laviano sequence.....	42
3.2 Scaling laws	50

3.2.1	Data collecting and processing	50
3.2.2	P- and S- path attenuation.....	54
3.2.3	P- and S- site transfer functions.....	57
3.2.4	Seismic moment, source radius and static stress drop.....	59
3.2.5	Moment and local magnitude	63
3.3	Conclusion	64
❖	Section C Time domain	65
Chapter 4 Empirical Green Function's (EGF) Approach.....		65
4.1	Introduction.....	65
4.2	Theory of EGF analysis	66
4.3	Projected Landweber method	67
4.4	Conditions of applicability EGF method's.....	69
4.4.1	Difference in magnitude between master event and EGF: synthetic test	70
4.4.2	Processing of near-source data	74
Chapter 5 Source parameters from RSTFs		77
5.1	Introduction.....	77
5.2	Effects of directivity: rupture duration and seismic moment	77
5.3	Corner frequency and rupture velocity	80
Chapter 6 Applications		84
6.1	L' Aquila sequence	84
6.1.1	M_w 6.3 L' Aquila mainshock	88
6.1.2	Cluster of events with $M_w \geq 3.0$	94
6.2	M_w 2.9 Laviano mainshock.....	100
6.3	Conclusions.....	103

❖ Summary.....	104
References.....	106

Acknowledgments

This work would not have been possible without the help and encouragement of many people and I would like to take this opportunity to express my thankfulness to them.

First of all I would like to thank my tutor Prof. Aldo Zollo for having followed me in these years and for his valuable teachings. Thanks to him I learned to love research in seismology and I understand how to work for and with a research group. So I take all the researchers, post-docs and students of “Laboratorio di Ricerca in Sismologia Sperimentale e Computazionale” (RISSC-Lab) for their constructive comments, valuable discussions and support. In particular, I thank Emanuela Matrullo, Simona Colombelli and Claudio Martino who made this experience unforgettable.

I wish to express my profound gratitude to my family, and in particular my parents, Annunziata and Alfonso, for all they have given me in life and for encouraging me to pursue my education.

Finally, I would like to thank my boyfriend (soon my husband) Gianni for encouraging me during our life together.

Thanks to everyone!

Introduction

The large majority of microearthquake source parameter estimations now available in literature have been obtained from measurements performed in the frequency domain. The seismic moment, for example, is derived from the low frequency level of displacement spectra and the rupture length (radius of circular ruptures) is obtained from the spectral corner frequency, according to kinematic and dynamic source models (Brune, 1970; Madariaga, 1976). The analysis of the source parameters is often complicated by their spectral properties at high frequencies, where path and site effects are not easily distinguished from the source characteristics. One way to overcome this problem is to use the Empirical Green Functions (EGFs) that allow to represent the contribution of propagation and site effects to signal without using approximate velocity models (e.g., Mori and Frankel, 1990; Hough, 1997; Ide et al., 2003; Abercrombie and Rice, 2005). The method requires two earthquakes having a similar hypocenter and focal mechanism but different size. The smaller earthquake, preferably 1 to 2 magnitudes smaller than the other, will act as a medium transfer function. Assuming that the path, site, and instrument effects are the same for both earthquakes, the time deconvolution of the two earthquakes will give the relative source time functions (RSTFs) of the larger earthquake at each considered station. The durations of each RSTF are then examined to retrieve some interesting properties regarding the extent and the rupture velocity of the event. They are essential to obtain accurate estimates of the source size and therefore of corner frequency. Thus, in the frequency domain, where the seismic moment is estimated by low-frequency level of displacement spectra, one major issue to be afforded is the adequate correction of observed ground motion for path attenuation and site response effects. Different approaches can be used which can be classified as parametric when both seismic source and attenuation models are selected a-priori (e.g., de Lorenzo et al., 2010; Edwards et al., 2008) or as non-parametric when data are analyzed to infer the source properties and attenuation models (e.g., Prieto et al., 2004; Bindi et al., 2006).

In this study we estimate the source parameters using a parametric approach, based on a physical description of the different effects which modify the signal radiated by the seismic sources. We use observations in time and/or frequency domain in order to

estimate the model parameters accounting for source, path attenuation and site effects. Moreover we apply the deconvolution method of Vallée (2004) to calculate the RSTFs and to get accurate estimates source size and rupture velocity.

This thesis is divided in three sections:

- Section A. We will give a brief review of the theory of seismic source, starting from the representation integral. This theorem is the basis of the arguments explained in the next sections: in section B it will be used in the frequency domain, while in section C we will discuss its applicability in the time domain.
- Section B. In this section the spectral model used to estimate the source parameters in the frequency domain will be explained, as well as the multi-step, non-linear inversion strategy. To test the iterative multi-step procedure the resolution test on Laviano sequence (Southern Italy) is applied. Finally we will discuss about the scaling relationships of source parameters which have been estimated for a database with local magnitude [0.1:3.7] both from P- and S-wave signals.
- Section C. In the third section we will focus on the time domain deconvolution method of EGFs. We will first outline the physical constraints on the RSTFs. Then, we will describe in detail how to compute the deconvolution. Moreover we will discuss the advantage of using RSFs to obtaine accurate estimates of source parameters and information on rupture process. In conclusion the applications of EGFs method are shown for large, moderate and small events.

Section A Seismic source theory

1. The representation theorem

The representation theorem is a formula for the ground displacement, at general point in space and time, in terms of the quantities that originated the motion: these are body forces and/or applied tractions over surface of the elastic body.

In a kinematic description of the seismic source, the theory that links the source and propagation is the representation theorem: the displacement u generated by a discontinuity across a internal surface Σ has components:

$$u_i(\vec{x}, t) = \int_{-\infty}^{+\infty} d\tau \int_{\Sigma} [u_j(\xi, t)] C_{jkpq} G_{ip,q}(\vec{x}, t; \xi, \tau) v_k d\Sigma(\xi) \quad (1.1)$$

where C_{jkpq} is a tensor of an elastic constant, $G_{ip,q}$ are the Green's functions and v_k is the normal to the surface Σ . The function $G_{ip,q}(\vec{x}, t; \xi, \tau)$ represents the effect of the propagation of elastic waves through the medium.

The only case in which the Green's function can be written explicitly is when the medium is homogeneous, isotropic and unlimited, and its expression is given by:

$$G_{ip}(\xi, \tau; x, t) = \frac{1}{4\pi\rho} (3\gamma_i\gamma_p - \delta_{ip}) \frac{1}{r^3} \int_{r/\alpha}^{r/\beta} t' \delta(t - \tau - t') + \frac{1}{4\pi\rho\alpha^2} \gamma_i\gamma_p \frac{1}{r} \delta\left(t - \tau - \frac{r}{\alpha}\right) - \frac{1}{4\pi\rho\beta^2} (\gamma_i\gamma_p - \delta_{ip}) \frac{1}{r} \delta\left(t - \tau - \frac{r}{\beta}\right) \quad (1.2)$$

where γ is the unit vector pointing from the source ξ to the receiver x and $r = |x - \xi|$. α and β are the P- and S-wave velocity, respectively, ρ is the medium density. The term that is attenuated with distance as $1/r^3$ is said *near field* while the terms that are attenuated as $1/r$ are called as *far field*.

From the representation theorem and the expression of the Green's function in a homogeneous, isotropic and unlimited medium, some theoretical tools used in the course

of work will be discussed.

2. Kinematic description of seismic source

The far field condition is equivalent to the Fraunhofer condition for linear optics ($L \ll \lambda$). If the distance between source and station is much greater than the linear dimension of the fault Σ , we can assume that both distance r and the direction cosines γ_i do not depend on the coordinates on the fault plane. Substituting the terms of equation (1.2) in the far field representation theorem we obtain the expressions for the displacement associated with P and S phase:

$$\begin{aligned} u_i^P &= \frac{\gamma_i}{4\pi\rho\alpha^3 r_0} C_{jkpq} \gamma_p \gamma_q v_k n_j \iint_{\Sigma} \Delta \dot{u} \left(\xi, t - \frac{r}{\alpha} \right) d\Sigma \\ u_i^S &= \frac{\delta_{in} - \gamma_i \gamma_n}{4\pi\rho\beta^3 r_0} C_{jkpq} \gamma_p \gamma_q v_k n_j \iint_{\Sigma} \Delta \dot{u} \left(\xi, t - \frac{r}{\beta} \right) d\Sigma \end{aligned} \quad (1.3)$$

where

$$u_j(\xi, t) = n_j \cdot \Delta u(\xi, t) \quad (1.4)$$

The scalar function $\Delta u(\xi, t)$ is the source function. Since in general $\Delta \dot{u}(\xi, t)$ can change quickly in time and space, the delay in the integrands of (1.2) must include variations of r with ξ . The factor r_0^{-1} is based on the distance of the receiver from each point r_0 of the fault. Equation (1.3) allows to obtain in a very simple way the characteristics of motion of seismic waves in the far field condition. From relationships $\gamma_i \gamma_i = 1$ and $\gamma_i(\delta_i - \gamma_i \gamma_p) = 0$ it is clear that the motion of particles hit by a P wave (particle motion) is perpendicular to the fault plane (parallel to the normal γ), while it is parallel for those hit by a wave S. The amplitude of the wave is attenuated as the inverse of the distance and it is inversely proportional to the cube of wave velocity. Then the amplitude of S-waves is a factor $(\alpha/\beta)^3$ greater than amplitude of P-waves. The factor $C_{jkpq} \gamma_p \gamma_q v_k n_j$ represents the radiation pattern of P-waves, determined by the orientation of the plane (v_k), the direction of the discontinuity of displacement (n_j) and the direction of the station relative to the fault (γ_p). Similarly if we consider the vectors γ' and γ'' orthogonal to surface

perpendicular to γ , the amplitude of the radiation of issued S waves is equal to $C_{jkpq}\gamma'_p\gamma'_q v_k n_j$ in the direction γ' and $C_{jkpq}\gamma''_p\gamma''_q v_k n_j$ in the direction γ'' . The shape of the displacement for the P and S waves is described by a term that expresses the time dependence; this has the form:

$$\Omega(\mathbf{x}, t) = \iint_{\Sigma} \Delta \dot{u} \left(\xi, t - \frac{|\mathbf{x} - \xi|}{c} \right) d\Sigma(\xi) \quad (1.5)$$

where c is the velocity of propagating wave. Developing in Taylor series the expression of distance between the receiver located in \mathbf{x} and source $d\Sigma|\mathbf{x} - \xi|$ and neglecting the terms of order higher than 1 we get:

$$r \approx r_0 - (\xi \cdot \gamma) \quad (1.6)$$

Replacing (1.6) in (1.5) we obtain:

$$\Omega(\gamma, t) = \iint_{\Sigma} \Delta \dot{u} \left(\xi, t - \frac{r_0 - (\xi \cdot \gamma)}{c} \right) d\Sigma \quad (1.7)$$

whose Fourier transform is:

$$\Omega(\gamma, t) e^{-\frac{i\omega r_0}{c}} = \iint_{\Sigma} \Delta \dot{u}(\xi, \omega) e^{-i\omega(\xi \cdot \gamma/c)} d\Sigma \quad (1.8)$$

The right side has the form of a double Fourier transform in space, expressed by:

$$\iint_{\Sigma} \Delta \dot{u}(\xi, \omega) e^{-i(\xi \cdot \mathbf{k})} d\Sigma = f(\mathbf{k}) \quad (1.9)$$

If the transform was known for all \mathbf{k} in the space of wave numbers, it would be possible to reverse the double integral and determine $\Delta \dot{u}(\xi, \omega)$ as a function of ξ completely, from

far-field observations. Unfortunately the Fourier transform is not known for all wave numbers \mathbf{k} but only for the projection of $\omega\gamma/c$ on Σ . Then the range of unsearchable wave numbers is restricted to \mathbf{k} parallel to Σ and $|\mathbf{k}| \leq \omega/c$. It follows that it is not possible to study the details of seismic source at length scales smaller than the shortest observed wavelength.

2.1 Seismic spectrum to the high frequency

When the frequency ω is close to zero, the Fourier spectrum $\Omega(\mathbf{x}, \omega)$ of the far field displacement tends to a constant value:

$$\Omega(\mathbf{x}, \omega \rightarrow 0) = \iint_{\Sigma} \Delta \dot{u}(\xi, t \rightarrow 0) d\Sigma \quad (1.10)$$

because

$$\dot{u}(\xi, \omega \rightarrow 0) = \int \Delta \dot{u}(\xi, t) \exp(i\omega t) dt \quad (1.11)$$

and moreover

$$\Delta \dot{u}(\xi, \omega \rightarrow 0) = \int \Delta \dot{u}(\xi, t) dt = \Delta u(\xi, t \rightarrow \infty) \quad (1.12)$$

So we obtain that:

$$\Omega(\mathbf{x}, \omega \rightarrow 0) = \iint_{\Sigma} \Delta u(\xi, \omega \rightarrow \infty) d\Sigma \quad (1.13)$$

Then $\Omega(\mathbf{x}, \omega \rightarrow 0)$ tends to the integral of the final slip on the fault plane. In other words, the far-field displacement spectrum at low frequencies tends to a constant value proportional to the seismic moment which is defined as:

$$M_0 = \mu \bar{u} A = \mu \times \text{average dislocation} \times \text{Area of the fault}$$

This result is true for any function of the dislocation on fault plane and asserts that the spectral trend at low frequencies is independent of the details of the process that led to the final value of dislocation. If the area of the fault surface is infinitesimal and the dislocation varies as a step in time, the far-field waveform is a Dirac delta function and then the spectrum is flat in the whole frequency range.

Section B Frequency domain

Chapter 1 Modeling of displacement spectra

1.1 Spectral model

The earthquake displacement spectrum can be described by the relationship:

$$U(\omega) = S_0(\omega)Q(\omega)R(\omega)I(\omega) \quad (1.14)$$

where $U(\omega)$ is the observed ground motion displacement spectrum, $S_0(\omega)$ is the source spectrum, $Q(\omega)$ is the path attenuation model, $R(\omega)$ is the site transfer function, and $I(\omega)$ is the instrumental response.

Now we will see in details these functions and their characteristics.

1.1.1 Source spectrum $S_0(\omega)$

S_0 is the source spectrum, which includes the frequency-independent radiation pattern and the geometrical spreading factors:

$$S_0(\omega) = C_s \frac{\Omega_0}{1 + \left(\frac{\omega}{\omega_c}\right)^\gamma} \quad (1.15)$$

Ω_0 is low-frequency spectral level ($\omega \ll \omega_c$) (related to seismic moment M_0), ω_c is the corner frequency (related to source radius, r) (Fig. 1.1) and

$$C_s = \frac{R_{\theta\phi}^c F_s}{4\pi\rho c^3 R} \quad (1.16)$$

where R is the hypocentral distance, c is the S- or P-wave velocity, ρ is the medium density, $R_{\varphi\varphi}^c$ is the radiation pattern coefficient, and F_S is the free-surface coefficient ($=2$). The above equations assume that the propagation medium can be described by a uniform velocity model. γ is a constant that control the shape of the spectrum curvature around the corner frequency.

In order to account for direct P- and S-wave amplification due to a vertically varying velocity structure, we replaced the constant in (1.16) with the more general expression (Aki and Richards,1980):

$$C'_S = \frac{R_{\varphi\varphi}^c F_S}{4\pi\rho_h^{1/2} c_h^{5/2} c_0^{1/2} R'} \quad (1.17)$$

where the sub-scripts h and o are for density and velocity values at the hypocenter and receiver depths, respectively. The geometrical spreading R' is estimated for a linear variation of velocity with depth (Ben-Menhaem and Singh, 1981):

$$R' = \sqrt{\frac{\rho_0 c_0}{\rho_h c_h}} R \quad (1.18)$$

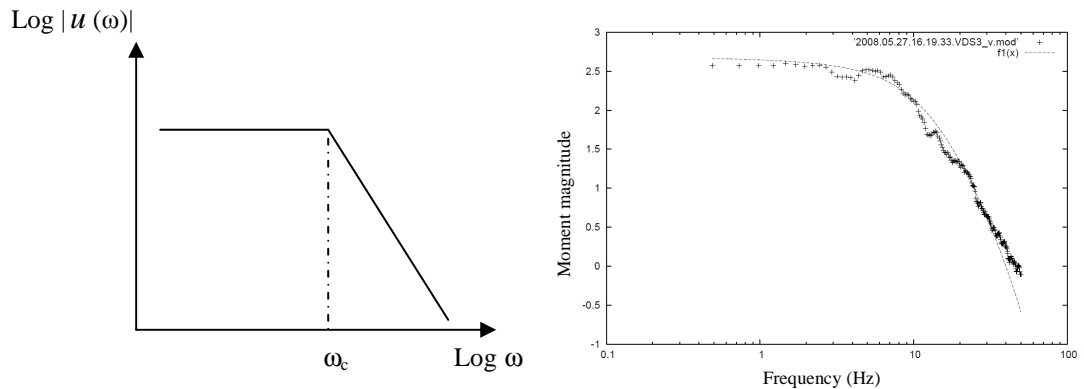


Figure 1.1: Left: theoretical variation of spectral amplitude in homogeneous medium as function of frequency. Right: example of observed displacement spectrum. The dashed line represents the theoretical spectrum $f_1(x)$.

1.1.2 Path attenuation model $Q(\omega)$

$Q(\omega)$ is the function which accounts for the anelastic body-wave attenuation along the travel path:

$$Q(\omega) = e^{-\alpha t^*} \quad (1.19)$$

with $t^* = T/Q$ is the attenuation parameter, depending on the travel time and the quality factor, which can be constant or frequency dependent.

The quality factor Q is defined by the relation

$$\frac{1}{Q(\omega)} = -\frac{\Delta E}{2\pi E} \quad (1.20)$$

where the second member is the fraction of energy (energy variation / total energy) dissipated in a cycle by a wave that propagates in an anelastic medium. Under this definition, highly attenuating media are characterized by small values of Q , and conversely, high values of Q correspond to weakly attenuating media.

In the most general formulation of the anelastic attenuation model, the coefficient t^* in equation (1.19) is frequency-dependent, thus it can be written as:

$$t^*(\omega) = \frac{T}{Q_0 \omega^n} \quad (1.21)$$

where n is a positive real number and Q_0 is the quality factor evaluated at a reference frequency, often fixed to 1 Hz (e.g. Morozov, 2008).

It has been shown that the quality factor Q has to depend on the frequency in order to satisfy the causality requirements (Aki-Richards, 1980). However, the same authors state that the attenuation law can be chosen to make Q effectively constant over the seismic frequency range. This is also the result of Azimi et al. (1968) which proposed a Q model which depends on frequency but is constant in the seismic frequency range. This result is more or less equivalent to that inferred by Kjartansson (1979), even if its

mathematical development could be partially questioned (in fact he was unable to derive the time domain expression of the impulse response).

Based on these theoretical developments, many studies have assumed that Q does not depend on the frequency in the typical frequency range of recorded waveforms. It is worth note that an important reason for the difficulty of assuming a frequency dependent Q model is that if Q is frequency dependent, for instance through a power law, then a strong dependence of body wave velocities on frequency should be inferred from the analysis of seismic data, whereas only exceptionally a dispersion relationship for P waves has been inferred.

The data selection is critical in terms of physical quantities (acceleration, velocity or displacement) and in terms of analyzed seismic phase, that is, P -wave, S -wave, surface wave or coda waves. In fact, due to the different frequency content, each of the listed phases can lead to a different result on the behavior of Q . However, particularly for body waves, the inability of accurately separate direct waves from secondary contributions, can lead to controversial results.

Another problem to be faced in estimating the anelastic attenuation properties of a study area concern its intrinsic correlation with source parameters and, in particular, the corner frequency and high frequency spectral fall-off γ . In fact γ is responsible of decay of spectrum to high frequency as well as the parameter t^* correlated with corner frequency and seismic moment. To high values of t^* (small values of Q) correspond small values of γ . This means that a robust strategy has to be adopted to reduce the correlation between t^*/Q and (M_0, f_c) .

1.1.3 Site transfer function $R(\omega)$

Site response functions represent the station-specific effect on the record.

The term $R(\omega)$ in equation (1.14) is the site transfer function that is a generally unknown function and, in the present study, has been determined by an iterative procedure. In fact, as detailed in the next chapter, the site transfer functions for P- and S-waves are determined through an iterative procedure based on the computation of displacement spectra residuals and stack at each receiver site.

There are several definitions of site term in literature, for example:

➤ Edwards et al. (2008) define the site transfer function for station j as $T_j(f) = A_j a_j(f) \exp(-\pi f k_j / f^a)$, where A_j is a frequency-independent correction factor, κ_j is a constant site-related attenuation operator (e.g., Anderson and Hough, 1984), f_a determines the frequency dependence of Q and $a_j(f)$ is the frequency-dependent site amplification function that takes into account resonant frequencies due to the layered, fractured subsurface (e.g., Steidl et al., 1996). In figure 1.2 the flowchart of method used by Edwards et al. (2008) is shown.

➤ The site transfer function $R_j(f)$ defined by de Lorenzo et al. (2010) is given by product of near site attenuation (described in terms of the k_j attenuation factor) $K_j(f) = \exp(-\pi f k_j)$ and local site amplification $A_j(f)$. $A_j(f)$ is not described by a particular mathematical relationship and depends on the elastic and geometrical properties of the rocks near the recording site (e.g. Tsumura et al., 1996). Considering the residual $\text{Res}_{ij}(f) = |U_{ij}^{obs}(f) - U_{ij}^{teo}(f)|$, where U_{ij}^{obs} and U_{ij}^{teo} are the observed and theoretical spectrum respectively, the site response $R_j(f)$ at station j is obtained minimizing, at each station, the quantity $\sum_{i=1}^{N_i} |\text{Res}_{ij}(f) - \ln R_j(f)|$. N_i is the number of spectra available for the event i .

➤ In Prieto et al. (2004), the source contribution is isolated by receiver contributions to the spectra following the method described by Warren and Sheare (2002). This method assume that the observed spectrum $D_{ij}(f)$ from each source S_i and receiver R_j (denoted S_i for the i th earthquake and R_j for the j th station) is a product of source effects and path-site effects. They iteratively stack all log spectra from each station, after removing the source term S_i , to obtain the path-station term R_j .

So attenuation and site responses are crucial parameters to obtain accurate estimates of source parameters. Therefore, it is necessary to adopt a multi-step inversion method to separate source, attenuation and site terms.

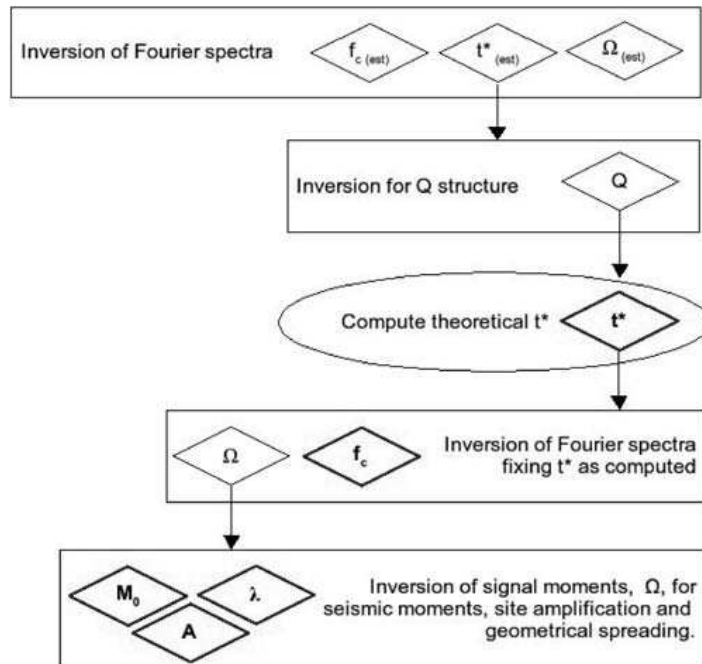


Figure 1.2: (from Edwards et al., 2008) A flowchart of the method used. From top to bottom: (1) the initial spectral inversion, (2) t^* estimates are then used to construct a Q model using a tomographic method, (3) theoretical t^* values are computed for each spectrum using the new Q model, (4) the spectral inversion is repeated, this time fixing the theoretical t^* value, and (5) finally, the signal moment is decomposed into seismic moment, a site amplification term, and a geometrical decay value. Parameters in bold diamonds indicate the final values of each parameter.

1.1.4 Instrumental response curve $I(\omega)$

The function $I(\omega)$ is the response curve of the specific instrument recording the earthquakes analyzed. For our analysis we consider the data recorded by Irpinia Seismic Network (ISNet) (Weber et al., 2007), network developed with the aim of permanently monitoring the Irpinia faults system in Southern Italy (Fig. 1.3).

Southern Apennines (Italy) are among the regions with highest seismic potential in the Mediterranean area. They have been interested by large earthquakes with magnitude up to M 7 generated as a consequence of a rather complex geodynamic which produces an anticlockwise motion of the Italian Peninsula (Scandone et al., 1979). The observed stress regime is mainly extensional (e.g., Montone et al., 2004) and, as a consequence, the dominant fault mechanism is normal, although there have been some

(e.g., May 5, 1990, Potenza, M 5.4; October 31–November 1, 2002, Molise, M 5.4) strike-slip earthquakes, the origin of which are still debated (Fracassi and Valensise, 2003; Valensise et al., 2003). The last destructive seismic event occurred in the area was the November 23, 1980 M 6.9 Irpinia earthquake which caused severe damage and about 3,000 deaths. The November 23, 1980 M 6.9 Irpinia earthquake was characterized by a complex normal fault mechanism involving three fault segments which ruptured in three distinct episodes 20 seconds apart (0s, 20s and 40s) with a total seismic moment of 18×10^{18} Nm (Bernard and Zollo, 1989).

ISNet network is composed by 30 stations covering an area of about 100×70 km². It is organized in “sub-nets”, each of them composed by a maximum of seven seismic stations and managed by a data concentrator (LCC, Local Control Center). All of the stations are equipped with a strong-motion accelerometer (Guralp CMG-5T) and a three-component velocimeter (Geotech S-13J), with a natural period of one second, thus ensuring a high dynamic recording range. Moreover, five stations host broad-band 40 s velocimeter for a better recording of regional and teleseismic events (Nanometrics Trillium 40S). The full recording dynamic range is ± 1 g, and the sensitivity is sufficient to record M_w 1.5 events at a distance of more than 40 km and down to M_w 0.2 at smaller distances.



Figure 1.3: Green squares indicate seismic stations. Yellow lines symbolize wireless radio links between each seismic station and its nearest Local Control Center (LCC, blue circles). Gray lines represent higher bandwidth, wireless connections among LCCs and the Network Control Center (red star). The latter transmission system is conceived as a redundant double ring.

Data acquisition at the seismic stations is performed by an innovative data-logger produced by Agecodagis, the Osiris-6 model (<http://www.agecodagis.com>).

In figure 1.4 the overall (sensor + data logger) instrumental response curve $I(\omega)$ for accelerometer Guralp CMG-5T, velocimeter Geotech S-13J and velocimeter Trillium 40S. We can observe that all curves present a cut-off high frequency of about 50 Hz. So we cannot obtain in frequency domain estimates of corner frequency $f_c \geq 50$ Hz.

The data are carefully corrected for instrument response such that $I(\omega)=1$.

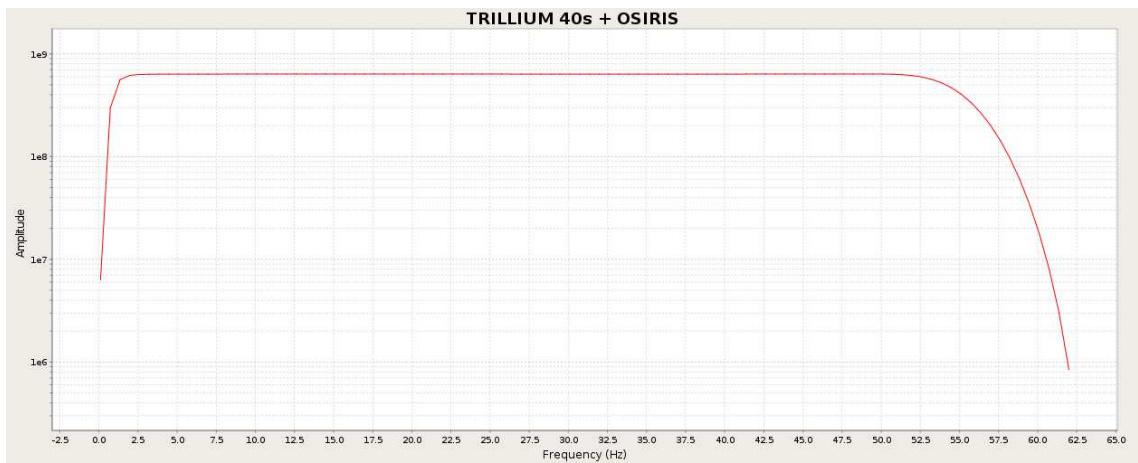
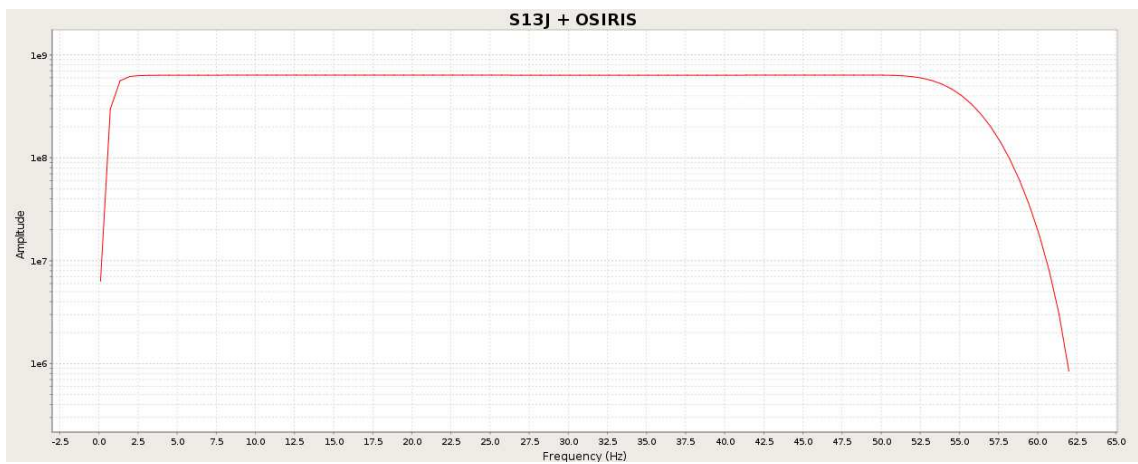
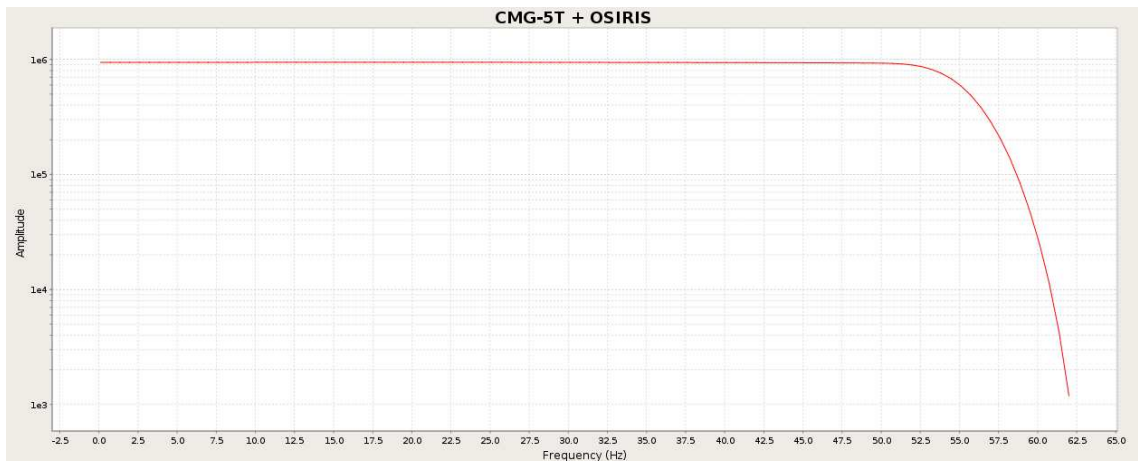


Figure 1.4: Overall (sensor + data logger) instrument frequency bandwidth for accelerometer Guralp CMG-5T, velocimeter Geotech S-13J and velocimeter Trillium 40S.

1.2 From spectral to seismic parameters

In this paragraph we will see the parameters that can be calculated by estimation of spectral parameters, that is spectral amplitude and corner frequency.

Given the estimation of spectral parameter Ω_0 and ω_c from the inversion of displacement spectra, the source parameters seismic moment M_0 and source radius r can be estimated through the formulae:

$$M_0 = C'_s \Omega_0 \quad (1.22)$$

$$r = k_c \cdot \frac{c}{f_c} \quad (1.23)$$

where c is the P- or S-wave velocity and f_c is the corner frequency ($f_c = \omega_c/2\pi$). k_c is a coefficient which depends on the adopted circular rupture model and wave type, e.g., assuming the Madariaga (1976)'s model $k_P = 0.32$ for P-waves and $k_S = 0.21$ for S-waves, while according to the Brune (1970)'s model $k_S = 0.37$.

The seismic moment and radius of a circular fault rupture from equations (1.22) and (1.23) are used to estimate the static stress drop (Keilis-Borok, 1959):

$$\Delta\sigma = \mu \frac{7\pi}{16} \bar{u} = \frac{7}{16} \frac{M_0}{r^3} \quad (1.24)$$

where μ is the rigidity and \bar{u} is the average earthquake slip.

Since the term r^3 in equation (1.24) is high, small errors associated with it will produce large errors in the determination of the stress drop. If we replace the area of the fault ($S = \pi r^2$) in equation (1.24), we obtain:

$$M_0 = \frac{16\Delta\sigma}{7\pi^{3/2}} S^{3/2} \quad (1.25)$$

or, considering the logarithm,

$$\log M_0 = \frac{3}{2} \log S + \log \left(\frac{16 \Delta \sigma}{7 \pi^{3/2}} \right) \quad (1.26)$$

From this equation it follows that, if the stress drop is constant for all earthquakes, then $\log S$ is proportional to $\frac{2}{3} \log M_0$. It has been shown empirically that this assumption is valid for a wide range of magnitude (Kanamori and Anderson, 1975). For moderate and large earthquakes ($M > 5$), $\Delta \sigma$ takes values in the range [1:10] MPa and an average value of 6 MPa (Fig. 1.5).

From estimates of seismic moment M_0 the moment magnitude is calculate through the relationship (Hanks and Kanamori, 1979):

$$M_w = \frac{2}{3} (\text{Log} M_0 - 9.1) \quad (1.27)$$

where M_0 is expressed in N·m.

The advantage of the M_w scale is that it is clearly related to a physical property of the source and it does not saturate for even the largest earthquakes.

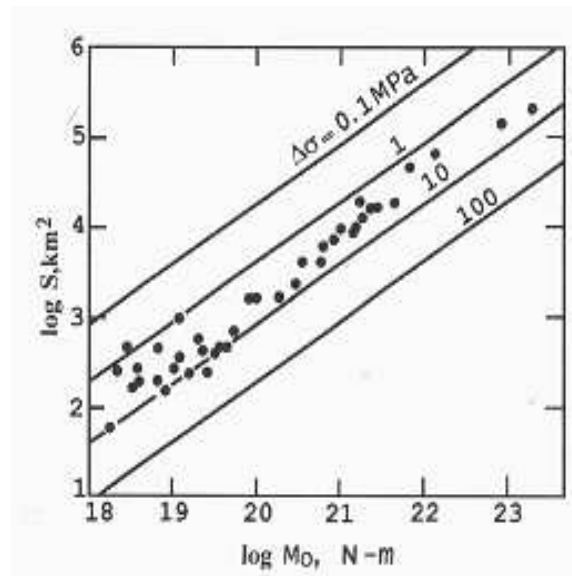


Figure 1.5: The relation between the fault area S and the seismic moment M_0 with lines of constant stress drop (Udias, 1999).

Chapter 2 Multi-step inversion of displacement spectra

This chapter provides a description of the inversion procedure used in this study and the principles of the theory of inversion. First a parametric modeling approach combined with a multi-step, non-linear inversion strategy will be described. It is based on the physical description of the different source, path attenuation and site effects which modify the signal radiated by seismic sources. Then a description of inverse theory is made with a distinction between global and local search methods. Finally, it will be given a more detailed description of the inversion method used in the thesis to estimate the source parameters, that is the method of Levenberg - Marquardt. This is a linearized inversion method combining the Hessian and gradient descent.

2.1 Inversion strategy: iterative, multi-step approach

We have adopted an iterative, multi-step approach for the inversion of P- and S-displacement spectra; in this approach source, attenuation and site response models are determined by applying progressive corrections for attenuation and site effects to the source spectral function.

Using the theoretical model in (1.14) we first estimated the attenuation parameter t_{ij}^* and the constant γ and after the spectral parameters Ω_0^{ij} and ω_c^{ij} (i and j are indexes of the event and station respectively) by a non-linear best-fitting method applied to the observed displacement spectra. Specifically, we applied the non-linear Levenberg-Marquardt least-square algorithm (Marquardt, 1963), implemented in the software package GNU PLOT (Janert, 2009), for curve fitting and parameters estimation.

Assuming that γ and t_{ij}^* follow a unimodal distribution with mean values equal to $\langle \gamma \rangle$ and $\langle t^* \rangle$ respectively, we applied the iterative procedure shown in the flowchart of figure 1.2, i.e.:

1. assuming $\langle \gamma \rangle = 2$ as initial guess, the spectral parameters Ω_{ij} , ω_c^{ij} , t_{ij}^* are estimated;
2. fixing the values of Ω_{ij} and ω_c^{ij} at the event-average estimates, the parameter t_{ij}^* is estimated. In this step we obtain new values of $t_{ij}^* \equiv t_{ij}^{*NEW}$. In order to be consistent

with the relationship between seismic moment and moment magnitude ($M_w \propto \text{Log} M_0$) (Hanks and Kanamori, 1979), for Ω_0^{ij} the geometric mean $\Omega_0^i = \left(\prod_{j=1}^{M_i} \Omega_0^{ij} \right)^{1/M_i}$ has been computed while for ω_c^{ij} the arithmetic mean $\omega_c^i = \sum_{j=1}^{M_i} \omega_c^{ij} / M_i$ has been computed (where M_i is the number of stations that have recorded the event i).

3. fixing the value of t_{ij}^* at the mean value $\langle t_{ij}^{* \text{NEW}} \rangle$ the displacement spectra are inverted for Ω_{ij} , ω_c^{ij} , γ_{ij} . So, new values of γ_{ij} for each displacement spectra are estimated and its mean value is denoted as $\langle \gamma^{\text{NEW}} \rangle$. Assuming $\langle \gamma \rangle = \langle \gamma^{\text{NEW}} \rangle$, the procedure is iterated until no changes in mean values of t_{ij}^* and γ are observed.

The iterative multi-step procedure should converge to a stable value of the average quantities, since t^* and γ are related only to that part of displacement spectrum with frequencies greater than corner frequency ω_c^{ij} ; furthermore t^* is independent of γ for frequencies less than ω_c^{ij} .

By fixing the best values of γ_{ij} and t_{ij}^* for each pair station-event obtained from the previous procedure, the site transfer functions $R(\omega)$ for P - and S -waves are determined through an iterative procedure. For each station j the site transfer function $R_j(\omega)$ is obtained from the average of the transfer functions inferred from each event i recorded at the station j :

$$R_j(\omega) = \frac{1}{N_j} \sum_{i=1}^j \frac{U_{ij}(\omega)}{S_{oij}(\omega) Q_{ij}(\omega)} \quad (2.1)$$

where N_j is the number of earthquakes recorded by the j -th station and $U_{ij}(\omega)$ is the observed P - or S -wave displacement spectrum for the event i . The same equation is applied for P - and S -wave displacement spectra, so that two site transfer functions specific for the analyzed seismic phase are retrievable. It is worth to note that the site transfer functions obtained from equation (2.31) account for both the constant and frequency dependent site amplification/attenuation effect and for the differences in the instrumental response between accelerometers and velocimeters.

The source spectrum $S_{0j}(\omega)$ for the event i , is obtained from equation (1.15), using the event average values Ω_0^i and ω_c^i defined above and the values of γ_{ij} for each pair station-event. The attenuation spectrum $Q_{ij}(\omega)$ is obtained from equation (1.29) using the parameter t_{ij}^* obtained from the second step of final iteration as described above.

In order get more refined estimations of the source spectrum, the observed P- and S-wave displacement spectra are then corrected for the estimated site response and attenuation functions :

$$U_{ij}^{SC}(\omega) = \frac{U_{ij}(\omega)}{Q_{ij}(\omega)R_j(\omega)} \quad (2.2)$$

where $U_{ij}^{SC}(\omega)$ is the site and attenuation corrected displacement spectrum. By fixing the mean value of t^* (obtained from the iterative procedure described above), the displacement spectra $U_{ij}^{SC}(\omega)$ are therefore inverted for γ_{ij} , Ω_0^{ij} and ω_c^{ij} to get new estimations of the spectral parameters Ω_0^{ij} and ω_c^{ij} .

The procedure to estimate the site response function can be iterated by recomputing the site functions $R_j(\omega)$ with equation (2.1), using the updated event source models. The iterative procedure is stopped when 1) the overall spectral misfit does not change significantly, 2) the retrieved average source parameters do not change significantly

2.1.1 Influence of noise

As we can see from the first part of the flowchart (Fig. 2.1), after the correction of displacement spectra for the overall instrument curve, the signal to noise S/N ratio is calculated in the whole range of frequency. The noise N is calculated in a 2.56-second time window before the arrival of P-wave. The signal is calculated in a 2.56-second time window around the manual P/S pick starting 0.25 s before the pick P/S.

The S/N ratio is used as a weighting factor in the inversion procedure.

In fact, the noise in the data introduces high-frequency oscillations in the displacement spectra, masking the corner frequency and the low frequency spectral amplitudes. To overcome this problem we "weigh" the amplitudes in the displacement spectra rather

than selecting a band to the inversion in which the signal-to-noise ratio is less than a priori fixed threshold value. In figure 2.2a the displacement spectrum of an event with moment magnitude $M_w=0.5$ is shown. We can observe that for frequency less of 6 Hz the S/N assumes low values, so this means the signal is strongly contaminated by noise. The noise is responsible of artificial low frequency plateau that give us an incorrect estimate of spectral amplitude and therefore of seismic moment. To avoid this problem, for events with local magnitude $M_L \leq 1.5$ the minimum frequency in the inversion is set equal to 6 Hz (Fig. 2.2b), while for events with $M_L > 1.5$ it is set equal to 0.5 Hz. In figure 2.2c an example of fit between the observed and calculated displacement spectrum of event with $M_w = 3.5$ is shown, together with the signal to noise ratio.

Moreover in the inversion procedure only the records with mean value of S/N less of 2 are selected to calculate the displacement spectra. In this way we impose that the spectrum of noise and of signal are dissimilar.

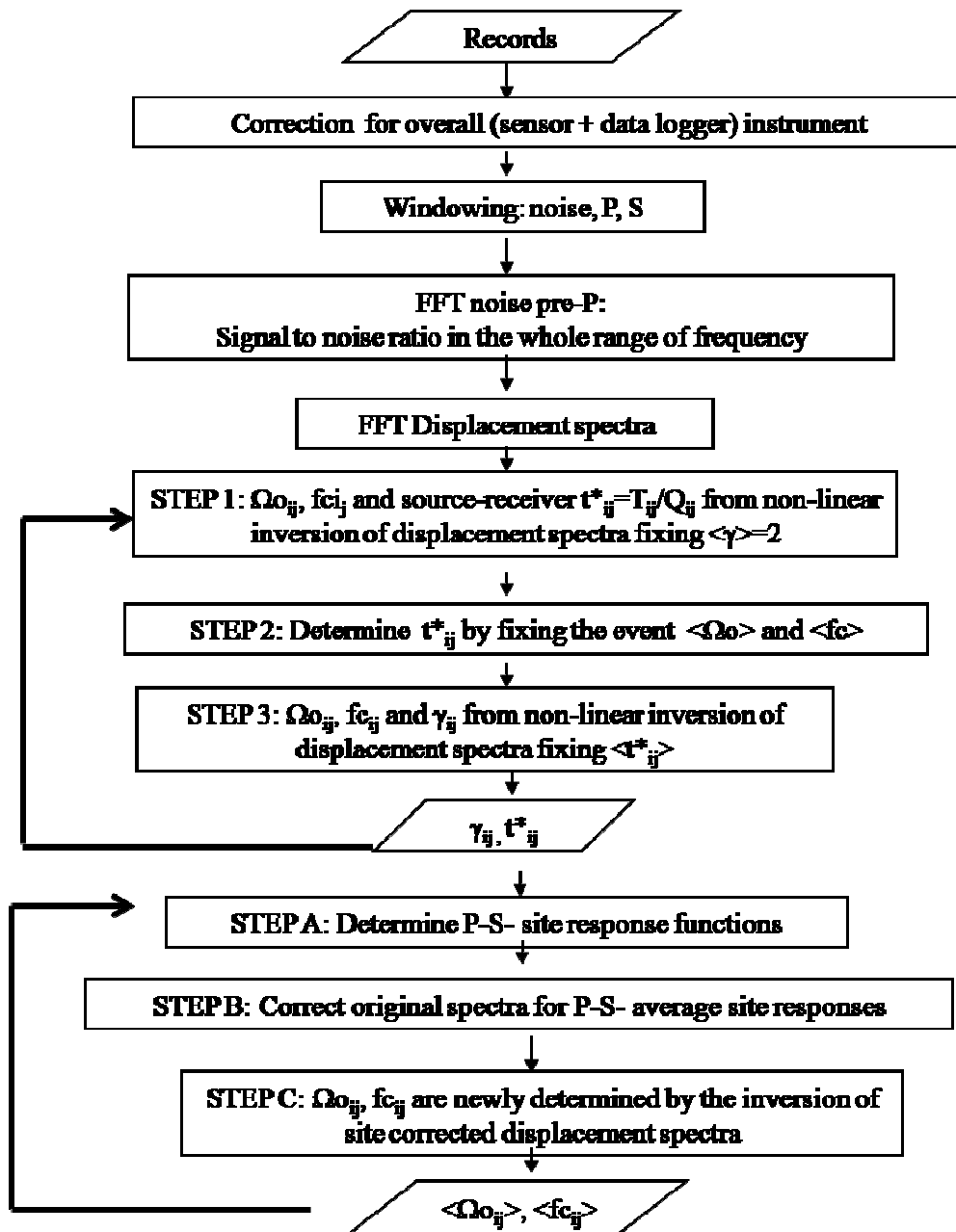


Figure 2.1: Flow chart of iterative multi-step approach.

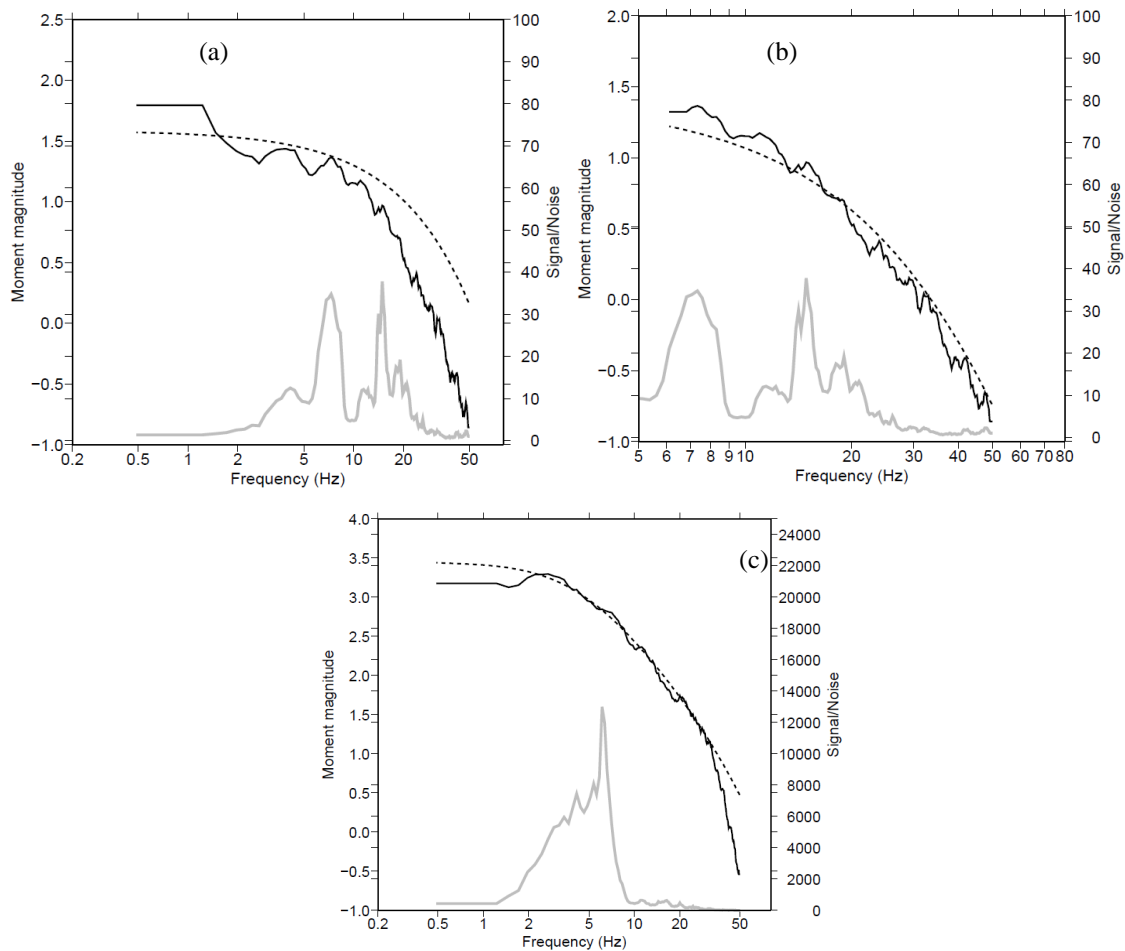
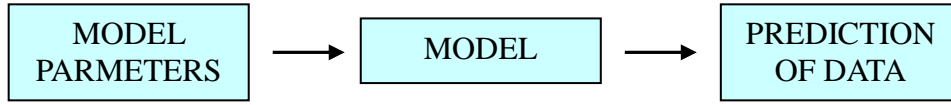


Figure 2.2: Fit between observed (black line) and calculated (dashed line) displacement spectra for event with $M_w=0.5$ in the range of frequency [0.5-50] Hz (a) and [6-50] Hz (b). The same is shown for an event with $M_w=3.5$ (c). In all graphics, the signal to noise ratio is also shown (grey line).

2.2 Introduction to inverse theory

Inverse theory is an organized set of mathematical techniques used for reducing data to obtain useful information about the physical world on the basis of inferences drawn from observation. Observations of physical quantities (measures) are the data. It is assumed that there is a specific method, usually a mathematical theory or model, that relates the model parameters to the data. Inverse theory addresses the reserve problem: starting with data and a general principle or model, it determines estimates of the model parameters (Fig. 2.3).

FORWARD PROBLEM



INVERS PROBLEM

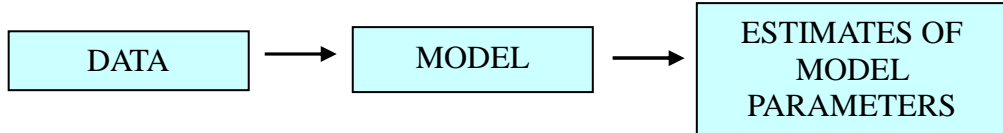


Figure 2.3: Outline of the forward and inverse problems.

Note that the role of inverse theory is to provide information about unknown numerical parameters to be used into the model, not to provide the model itself.

The starting point in the definition of inverse problems is the description of the data. In general, the data are a set of numerical values and, therefore, a vector provides a convenient way for their representation. If N measurements are made in a particular experiment, you can consider them as the elements of a vector \vec{d} of dimension N :

$$\vec{d} = [d_1, d_2, d_3, \dots, d_N]^T \quad (2.3)$$

where T denotes the transpose.

Similarly, the model parameters can be represented as the elements of a vector \vec{m} , whoselength is M :

$$\vec{m} = [m_1, m_2, m_3, \dots, m_M]^T \quad (2.4)$$

In general, the relationship between data and model is represented by one or more implicit equations of the type:

$$\begin{aligned} f_1(d, m) &= 0 \\ f_2(d, m) &= 0 \\ &\vdots \\ f_L(d, m) &= 0 \end{aligned} \quad (2.5)$$

where L is the number of equations.

So we can write:

$$\vec{f}(\vec{d}, \vec{m}) = 0 \quad (2.6)$$

These equations summarize what is known about the relationship between measured data and model parameters (unknowns).

The purpose of inverse theory is therefore to solve, or “invert”, these equations to derive the model parameters from the data available.

There are three types of inverse problems: linear, non linear and linearized inverse problems.

The linear inverse problems are problems where it is possible to separate the data from the model parameters and to obtain linear equations with respect to the data, for which (2.6) can be written as:

$$\vec{f}(\vec{d}, \vec{m}) = 0 = \vec{d} - G \cdot \vec{m} \quad (2.7)$$

Thus:

$$G \cdot \vec{m} = \vec{d} \quad (2.8)$$

where G is a $M \times N$ matrix.

If we denote by \vec{e} the vector whose elements are the errors on the data, then equation (2.8) becomes:

$$\vec{d} = G \cdot \vec{m} + \vec{e} \quad (2.9)$$

Indicating with \vec{m}^{est} the vector whose components are the estimates of parameters obtained by inversion, we can write:

$$\vec{m}^{est} = G^{-g} \cdot \vec{d} \quad (2.10)$$

where G^{-g} is the matrix called *generalized inverse*.

By introducing equation (2.9) in (2.10) we get:

$$\vec{m}^{est} = G^{-g} G \vec{m} + G^{-g} \vec{e} \quad (2.11)$$

The matrix $G^{-g} G \equiv R$ is called the *resolution matrix*.

Equation (2.11) can be written as:

$$\vec{m}^{est} = \vec{m} + (G^{-g} G - I) \vec{m} + G^{-g} \vec{e} \quad (2.12)$$

If the estimated model is equal to the true model ($\vec{m}^{est} = \vec{m}$), each parameter will be estimated independently. In equation (2.12) the operator $(G^{-g} G - I)$ means that any component of the estimated parameter of vector is a linear combination of different components of the vector of true parameters \vec{m} . If the matrix resolution coincides with the identity matrix I, all parameters are well resolved. The last term in equation (2.12) describes the effect of measurement errors on parameter estimation. These errors are determined from data errors. In fact, when data are uncorrelated and all have variance σ_{d_j} , the standard deviation of the estimated parameter σ_{m_i} , resulting from the propagation of data errors, is given by:

$$\sigma_m^2 = \sum_j (G_{ij}^{-g} \sigma_{d_j}) \quad (2.13)$$

In the linearized problem we assume that, locally, around a trial solution, the relation data-parameters is approximated by a linear relationship.

In the non-linear inverse problems the data and parameters of the model are linked by non-linear relationships. As will be seen in the next section, to solve these problems we can proceed following a linearization approach or by using optimization techniques.

2.3 Non linear inverse problem

The nonlinear problems are solved by a direct exploration of the cost function, defined as a measure of the difference between observed and predicted data. The search of

the absolute minimum of the cost function $E(m)$ is made difficult by the presence of secondary minimum (Fig. 2.4) (Menke, 1989).

These non-linear inversion's methods can be divided into two main categories:

- global search methods that investigate the whole parameter space (e.g., genetic algorithm, simulated annealing);
- local search methods looking for the minimum of the cost function in around of a trial solution (e.g., hill climbing methods, downhill simplex).

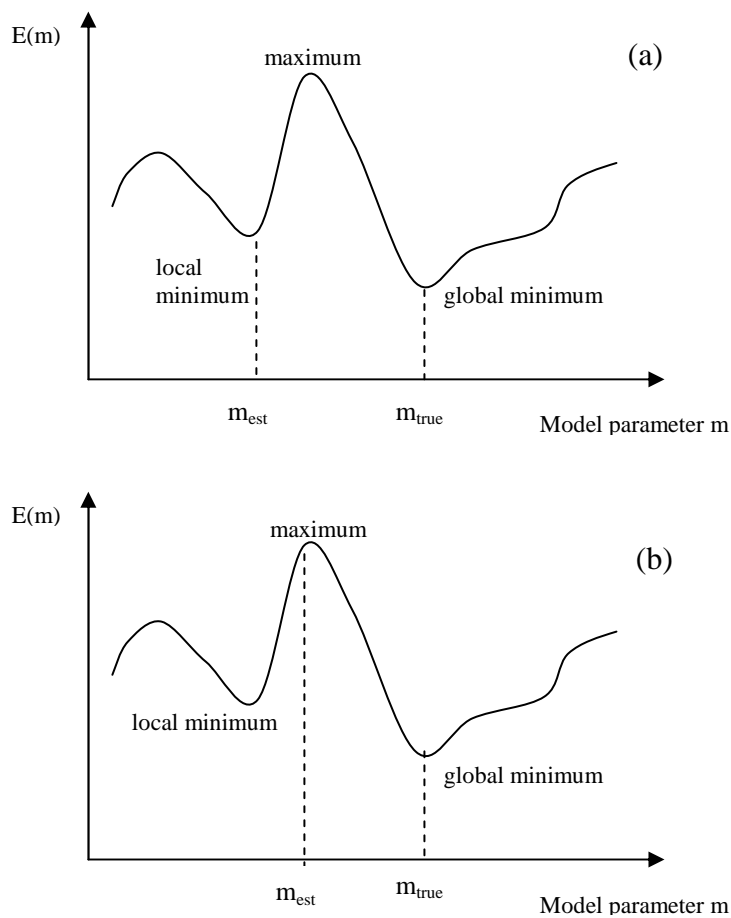


Figure 2.4: If the trial solution is too far from the global minimum, the method may converge to a local minimum (a) or to a maximum (b).

The *Simulated Annealing* is based on the analogy between the way in which a metal cools and freezes at a minimum energy of the crystal structure (annealing process) and the search for a minimum in a more general system (Davis, 1987).

The algorithm uses a random search which accepts not only those changes that lead to a

decrease of the function E , but also some changes that will lead to an increment of E . The implementation of simulated annealing is relatively simple. It is necessary to give the following “ingredients”: a representation of the possible solutions, a generator of random variations of solutions, a method to evaluate the function E of the problem and an annealing schedule, i.e. the initial temperature and rules for E decrease to the progression of research.

Regarding the genetic algorithm, the solution to the optimization problem is obtained on the basis of an evolutionary process, based on the principle of natural selection developed in the Darwinian theory (Goldberg, 1989). This principle asserts that individuals with more adaptability to the environment leave on average more numerous progeny. The basic properties necessary to carry out the evolutionary process are: heredity (each individual carries the genetic characteristics that have made it more suitable for the parent) and variability (different individuals must co-exist in a different manner suitable to the environment, so that the natural selection can act). Taking advantage of the terminology of genetics, chromosome is defined as a string of parameters chosen to describe the model and the population is a set of chromosomes. *Fitness*, which expresses the individual's ability to adapt to its surroundings, is connected to the value of the cost function: the search for the absolute minimum of the cost function consists in the choice of the chromosome that, within a given population, is characterized by the highest fitness.

The *Hill Climbing* search algorithm is an iterative algorithm that starts with an arbitrary solution to a problem, then attempts to find a better solution by incrementally changing a single element of the solution. If the change produces a better solution, an incremental change is made to the new solution, repeating until no further improvements can be found.

The *Downhill Simplex*, proposed by Nelder and Mead (1965), is a technique that requires only to evaluate the cost function and its derivatives. A simplex is a geometrical figure consisting, in N dimensions, $N + 1$ points (or vertices) and by interconnect all segments, polygonal faces, etc.. For example, in 2D the simplex is a triangle, a tetrahedron in 3D, and so on. This method optimizes the cost function E making a series of purely geometrical operations (reflections, expansions, contractions).

The optimization procedure is stopped if the vector distance covered in a cycle is a

fraction of a tolerance tol established a priori. Alternatively, it is possible to request that the improvement of the minimum value of the function in the stopping step is a fraction of a certain tolerance $ftol$ established a priori.

2.4 The Levenberg-Marquardt algorithm

Let us consider N points for a model characterized by a set of M unknown parameters $k, k = 1, 2, \dots, M$. The prediction error or misfit (χ^2) is defined as the difference between the observed data (d^{obs}) and predicted data (d^{pre}):

$$\chi^2(\vec{a}) = \sum_{i=1}^N \left(\frac{d_i^{obs} - d_i^{pre}}{\sigma_{d_i}} \right)^2 \quad (2.14)$$

where each measurement is weighted by the reciprocal of its variance. This function give more weight to more accurate data. To minimize χ^2 and estimate the parameters of best-fit it is possible to use an iterative process. Selected some trial values for the parameters, we evaluate the trial solution and the procedure is repeated until the variation of χ^2 is no longer significant. Assuming for χ^2 a quadratic form, expanding in a Taylor series around the minimum and stopping the expansion at second order we get:

$$\begin{aligned} \chi^2(\vec{a}) &= \chi^2(a_k) + \sum_i \frac{\partial \chi^2}{\partial a_i} a_i + \frac{1}{2} \sum_{i,j} \frac{\partial^2 \chi^2}{\partial a_i \partial a_j} a_i a_j + \dots \\ &\approx \gamma - \vec{d} \cdot \vec{a} + \frac{1}{2} \vec{a} \cdot D \cdot \vec{a} \end{aligned} \quad (2.15)$$

where

$$\gamma \equiv \chi^2(a_k) \quad \vec{d} \equiv -\nabla \chi^2 \Big|_{a_k} \quad [D]_{i,j} = \frac{\partial^2 \chi^2}{\partial a_i \partial a_j} \Big|_{a_k} \quad (2.16)$$

\vec{d} is a M -vector and D is a $M \times M$ matrix.

If the approximation is a good one, we know how to jump from the current trial parameters \vec{a}_{cur} to the minimizing ones \vec{a}_{min} in a single leap, namely:

$$\vec{a}_{\min} = \vec{a}_{cur} + D^{-1} \cdot [-\nabla \chi^2(\vec{a}_{cur})] \quad (2.17)$$

On the other hand, (2.15) might be a poor local approximation to the shape of the function that we are trying to minimize at \vec{a}_{cur} . In that case, a new step is considered with a new trial parameter \vec{a}_{next}

$$\vec{a}_{next} = \vec{a}_{cur} - costante \cdot \nabla \chi^2(\vec{a}_{cur}) \quad (2.18)$$

To use equation (2.17) or (2.18) we must be able to calculate the gradient of the function χ^2 at any set of parameters. In particular, using equation (2.17), we need the matrix D , which is the matrix of second derivatives of the error of prediction (Hessian matrix) for each \vec{a} . The matrix D is known because the form of χ^2 is precisely known. This allows us to use both relationships. The equation (2.18) is only used when the equation (2.17) does not minimize the prediction error.

Let us see how to calculate the gradient and the Hessian of χ^2 .

Suppose that we have N points (x_i, y_i) , for $i = 1, \dots, N$. If the fitting model is

$$y = y(\vec{x}; \vec{a}) \quad (2.19)$$

the misfit function will be:

$$\chi^2(\vec{a}) = \sum_{i=1}^N \left(\frac{y_i - y(x_i; \vec{a})}{\sigma_i} \right)^2 \quad (2.20)$$

where σ_i is the standard deviation associated with each point, and y_i and $y(x_i; \vec{a})$ are the observed and predicted model, respectively.

The gradient of χ^2 compared to vector \vec{a} is zero in correspondence of minimum and has components:

$$\frac{\partial \chi^2}{\partial a_k} = -2 \sum_{i=1}^N \frac{[y_i - y(x_i; \vec{a})]}{\sigma_i^2} \frac{\partial y(x_i; \vec{a})}{\partial a_k} \quad k = 1, 2, \dots, M \quad (2.21)$$

The mixed partial derivative is given by:

$$\frac{\partial^2 \chi^2}{\partial a_k \partial a_l} = 2 \sum_{i=1}^N \frac{1}{\sigma_i^2} \left[\frac{\partial y(x_i; \vec{a})}{\partial a_k} \frac{\partial y(x_i; \vec{a})}{\partial a_l} - [y_i - y(x_i; \vec{a})] \frac{\partial^2 y(x_i; \vec{a})}{\partial a_l \partial a_k} \right] \quad (2.22)$$

Then we put

$$\beta_k \equiv -\frac{1}{2} \frac{\partial \chi^2}{\partial a_k} \quad \alpha_{kl} \equiv \frac{1}{2} \frac{\partial^2 \chi^2}{\partial a_k \partial a_l} \quad (2.23)$$

In this way $[\alpha] = 1/2 D$ and the equation (2.17) can be rewritten as the set of linear equations:

$$\sum_{l=0}^{M-1} \alpha_{kl} \delta a_l = \beta_k \quad (2.24)$$

This set is solved for the increments δa_l that, added to the current approximation, give the next approximation.

The equation (2.18), the gradient descent formula, translates to:

$$\delta a_l = \text{costante} \times \beta_l \quad (2.25)$$

Note that the components of the Hessian matrix (Eq. 2.22) depend both on the first derivative and on the second derivatives of the function with respect to their parameters. Some treatments proceed to ignore the second derivative whose multiplicative term in equation (2.22) is $[y_i - y(x_i; \vec{a})]$. For a good model, this term represents the random error on the measurement of each point, and that error could be either positive or negative. It may be generally unrelated to the model and then the second derivative term tends to zero when the sum of i is considerate.

The inclusion of the second derivative term can in fact be destabilizing if the model reproduces the data badly, or if it is contaminated by outliers, then α_{kl} can be defined

through the formula:

$$\alpha_{kl} = 2 \sum_{i=1}^N \frac{1}{\sigma_i^2} \left[\frac{\partial y(x_i; \vec{a})}{\partial a_k} \frac{\partial y(x_i; \vec{a})}{\partial a_l} \right] \quad (2.26)$$

The condition of minimum for χ^2 , i.e. $\beta_k = 0$, is independent by matrix $[\alpha]$.

A combination of the Hessian method (Eq. 2.23) and the method of descent gradient (Eq. 2.25) is the method of Levenberg - Marquardt. It is based on two elementary, but important observations. Let us consider the “constant” in the equation (2.25). The first observation is that the components of the Hessian matrix provide information on the order of magnitude of the problem.

Equation (2.20) shows that the quantity χ^2 is dimensionless. β_k has the dimensions of $1/a_k$, whose unit of measure is cm^{-1} , or kW, or any other measure. In fact, according to the problem you are solving, each component of β_k can have different dimensions. The constant of proportionality between β_k and δa_k must therefore have a size of a_k^2 and the only quantity that has this size is the reciprocal of the diagonal element, i.e. $1/\alpha_{kk}$. So the scale of constant must be assigned: so that this constant is not too large, it is divided by a dimensional factor λ , with the possibility to assign $\lambda \gg 1$ to stop the step. So the equation (2.25) is replaced by:

$$\delta a_l = \frac{1}{\lambda \alpha_{ll}} \beta_l \quad \text{or} \quad \lambda \alpha_{ll} \delta a_l = \beta_l \quad (2.27)$$

Is also necessary that α_{ll} is positive, but this is guaranteed by the definition (2.26): this is another reason for adopting this equation.

The second observation is that the equations (2.24) and (2.27) can be combined if a new matrix α' is defined:

$$\begin{aligned} \alpha'_{jj} &\equiv \alpha_{jj}(1 + \lambda) \\ \alpha'_{jj} &\equiv \alpha_{jk} \quad (j \neq k) \end{aligned} \quad (2.28)$$

and then replace both equations (2.24) and (2.27) with

$$\sum_{l=0}^{M-1} \alpha'_{kl} \delta a_l = \beta_k \quad (2.29)$$

When λ is very large, the matrix α' is reduced to diagonal element, so equation (2.29) becomes identical to equation (2.27). If λ instead tends to zero, equation (2.29) becomes identical to equation (2.24).

From an operational viewpoint, given an initial set of parameters, the Marquardt algorithm is based on the following steps:

- a. compute χ^2 ;
- b. pick a modest value for λ , say $\lambda = 0.001$;
- c. solve the linear equation (2.29) for $\delta \bar{a}$ and evaluate $\chi^2(\bar{a} + \delta \bar{a})$;
- d. if $\chi^2(\bar{a} + \delta \bar{a}) \geq \chi^2(\bar{a})$, increase λ by a factor of 10 (or another substantial factor) and go back to step c;
- e. if $\chi^2(\bar{a} + \delta \bar{a}) \leq \chi^2(\bar{a})$, decrease λ by a factor of 10, update the trial solution $\bar{a} \leftarrow \bar{a} + \delta \bar{a}$ and go back to step c.

Chapter 3 Applications

3.1 Resolution test: Laviano sequence

Here we propose a resolution test aimed at estimating the minimum moment magnitude value above which source parameters can be effectively estimated. For this test we consider a microearthquake sequence started on May 25, 2008 in Irpinia region, nearby the village of Laviano, at about 800 m distance from the 1980 epicenter (Fig. 3.1). The moment magnitude M_w and local magnitude M_L of the events ranged from 0.8 to 2.9 and from 0.3 to 2.7, respectively, with the largest magnitude earthquake occurring at the middle of the sequence (Stabile et al., submitted to *Scientific Reports*).

We chose that sequence for two principal reasons. 1) The striking waveform similarity and the coherence of the P-wave first motion polarity at different stations indicate that events are co-located and share the same focal mechanism and site effects. As an example of this strong likeness across all the events, band-pass filtered (1-20 Hz), amplitude-normalized waveforms of the velocimetric vertical component records at COL3, SNR3, and VDS3 stations for all microearthquakes in the sequence are shown in figure 3.2. 2) The range of moment magnitude of these events covers the range of M_w of the whole dataset.

The iterative multi-step approach described in Chapter 2 was applied to Laviano sequence for S- waves. Five iterations were considered and for each iteration the hypotheses of unimodal distributions for the high-frequency falloff rate γ and attenuation parameter t_{ij}^* were tested. In fact in figure 3.3 the histograms of γ and t_{ij}^* obtained from inversion of S- displacement spectra are shown; the inverse triangles represents the mean values of γ and t_{ij}^* . The trade-off between attenuation parameter t_{ij}^* and corner frequency ω_c^{ij} is solved through the two inversions of displacement spectrum, that is, *step1/* the displacement spectra are inverted to estimate Ω_{ij} , ω_c^{ij} and t_{ij}^* ; *step2/* fixing the values of Ω_{ij} and ω_c^{ij} at the event-average estimates in the *step1*, the displacement spectra are inverted to estimate t_{ij}^* (flow chart 2.1). We can observe in figure 3.4 that in each iteration at *step2* the attenuation parameter and corner frequency are not correlate.

Moreover we have verified that any correlation between γ and ω_c^{ij}/t_{ij}^* is introduced, as shown in figure 3.5.

The iterative multi-step procedure converges to a stable value of the average quantities $\langle \gamma \rangle$ and $\langle t_{ij}^* \rangle$ after the third iteration (Fig. 3.6). In table 1 the average of γ and t_{ij}^* obtained from each iteration are listed.

In this test the site response functions $R_{ij}(\omega)$ are not calculated, thus the displacement spectra are not corrected for $R_{ij}(\omega)$. But, as mentioned above, the events are co-located and share the same site effects. Figure 3.7 shows a log-log representation of the corner frequency vs seismic moment for S-waves along with the associated uncertainties. These parameters were obtained by *step3* of fourth iteration (flow chart 2.1), where the average of γ and t_{ij}^* become stable and any correlation between γ/t_{ij}^* and ω_c^{ij} is observed. The constant stress drop lines at values 0.1 to 100 MPa are shown (Kanamori and Anderson, 1975) in figure 3.7, where stress drop is estimated using the Madariaga's model for the earthquake rupture radius. A clear deviation from a self-similar scaling of the corner frequency is observed for seismic moments M_0 smaller than about 10^{11} Nm ($M_w \approx 1$), above which the static stress drop $\Delta\sigma$ remains constant with a value of (3.9 ± 2.2) MPa (red line). We verified that the events belong to the same distribution with constant $\Delta\sigma$ by the χ^2 statistical hypothesis test. The grey line indicates the minimum values of seismic moment (and therefore moment magnitude) above which we can obtain reliable estimates of source parameters, that is corner frequency and seismic moment. The vertical arrows indicate corner frequencies greater than our maximum resolution threshold, while the horizontal arrows indicate that the seismic moments of these events are indeterminate. Then for S-wave the source parameters can be effectively estimated from $M_0 \geq 10^{11}$ Nm. By assuming that the estimates of seismic moment obtained from P- and S- waves are the same, we can conclude that the resolution threshold $M_0 \geq 10^{11}$ Nm is also valid for P-waves.

Table 1: Average of high-frequency falloff rate γ and attenuation parameter t_{ij}^* obtained from each iteration

Iteration	$\langle \gamma \rangle$	$\langle t_{ij}^* \rangle$
1	1.76 ± 0.61	0.020 ± 0.010
2	1.56 ± 0.68	0.023 ± 0.010
3	1.52 ± 0.68	0.024 ± 0.011
4	1.51 ± 0.68	0.024 ± 0.012
5	1.51 ± 0.68	0.024 ± 0.012

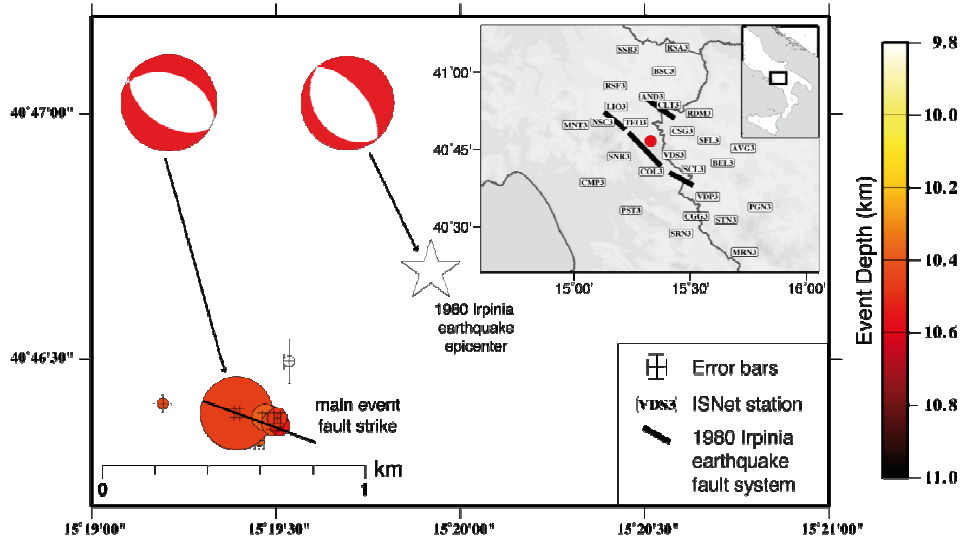


Figure 3.1: Map of the May 25-28, 2008 microearthquake sequence located nearby the village of Laviano (Southern Italy). The events of the sequence are extremely concentrated in a volume less than 300 m per side and the swarm is about 800 m distance from the 1980 Irpinia earthquake epicenter. The fault plane solution of the mainshock is consistent with the 1980 Irpinia earthquake fault plane. The dimension of circles is the Madariaga' circular rupture area of events while the color represents the event depth. Horizontal location errors are also reported in the figure for each event. (Stabile et al., submitted to *Scientific Reports*).

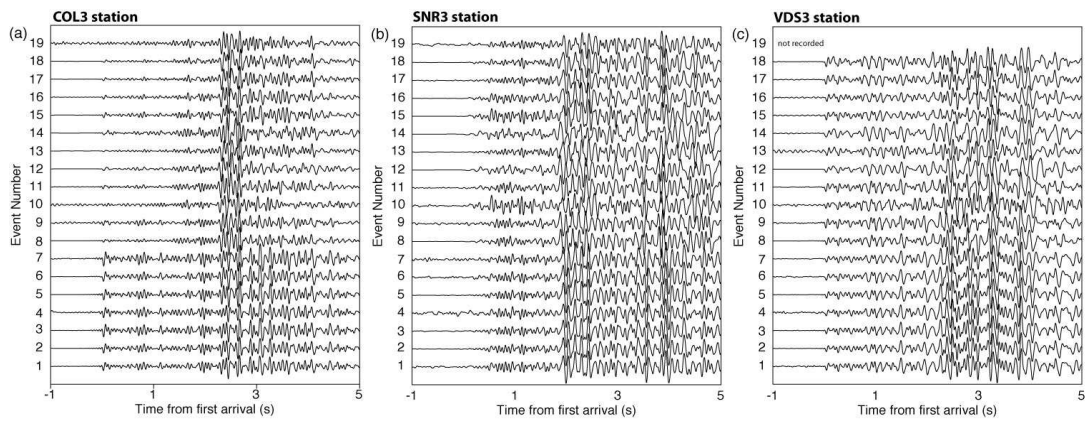


Figure 3.2: Vertical-component velocity records of the seismic sequence at (a) COL3, (b) SNR3, and (c) VDS3 stations. The waveforms are band-pass filtered from 1 Hz to 20 Hz and are amplitude-normalized. Events are ordered in time from below to above and the event number increases with the event origin-time. Waveforms are aligned respect to the first P-wave arrival (Stabile et al., submitted to *Scientific Reports*).

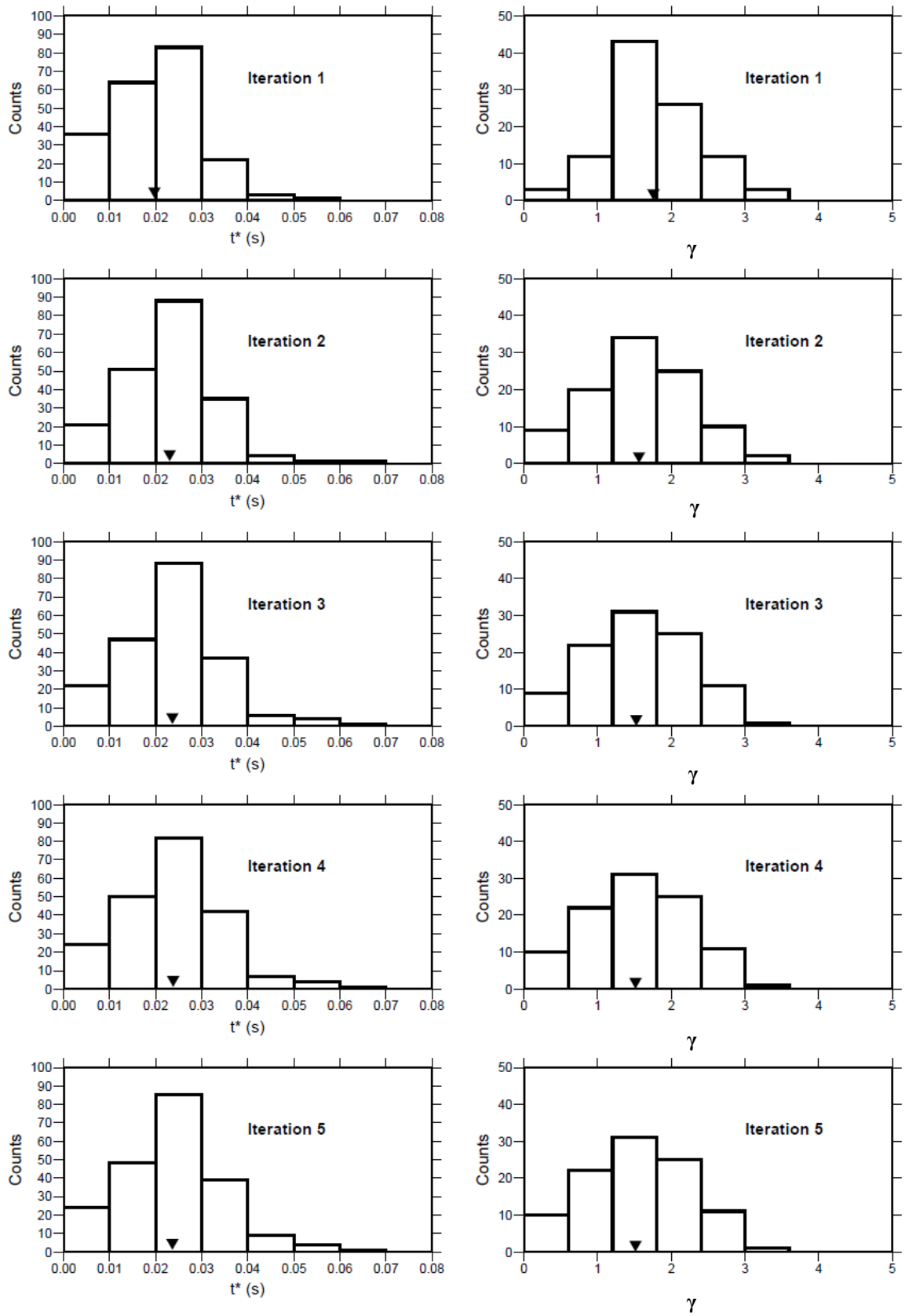


Figure 3.3: Distributions of high-frequency falloff rate γ and attenuation parameter t^* obtained from each iteration. The inverse triangles represent the average of γ and t^* .

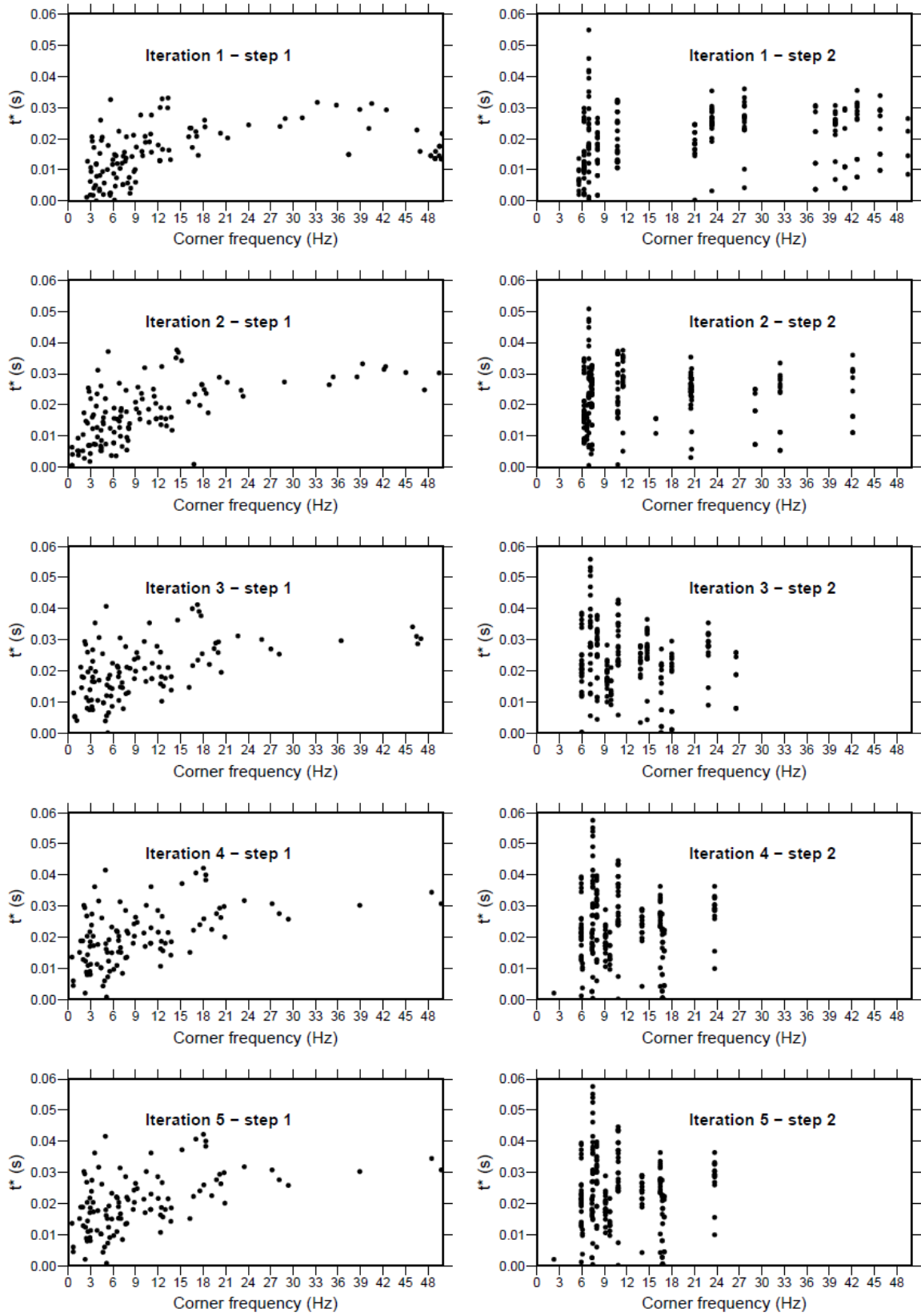


Figure 3.4: Correlation between attenuation parameter t^* and corner frequencies at step1 and step2 of iterative multi-step procedure.

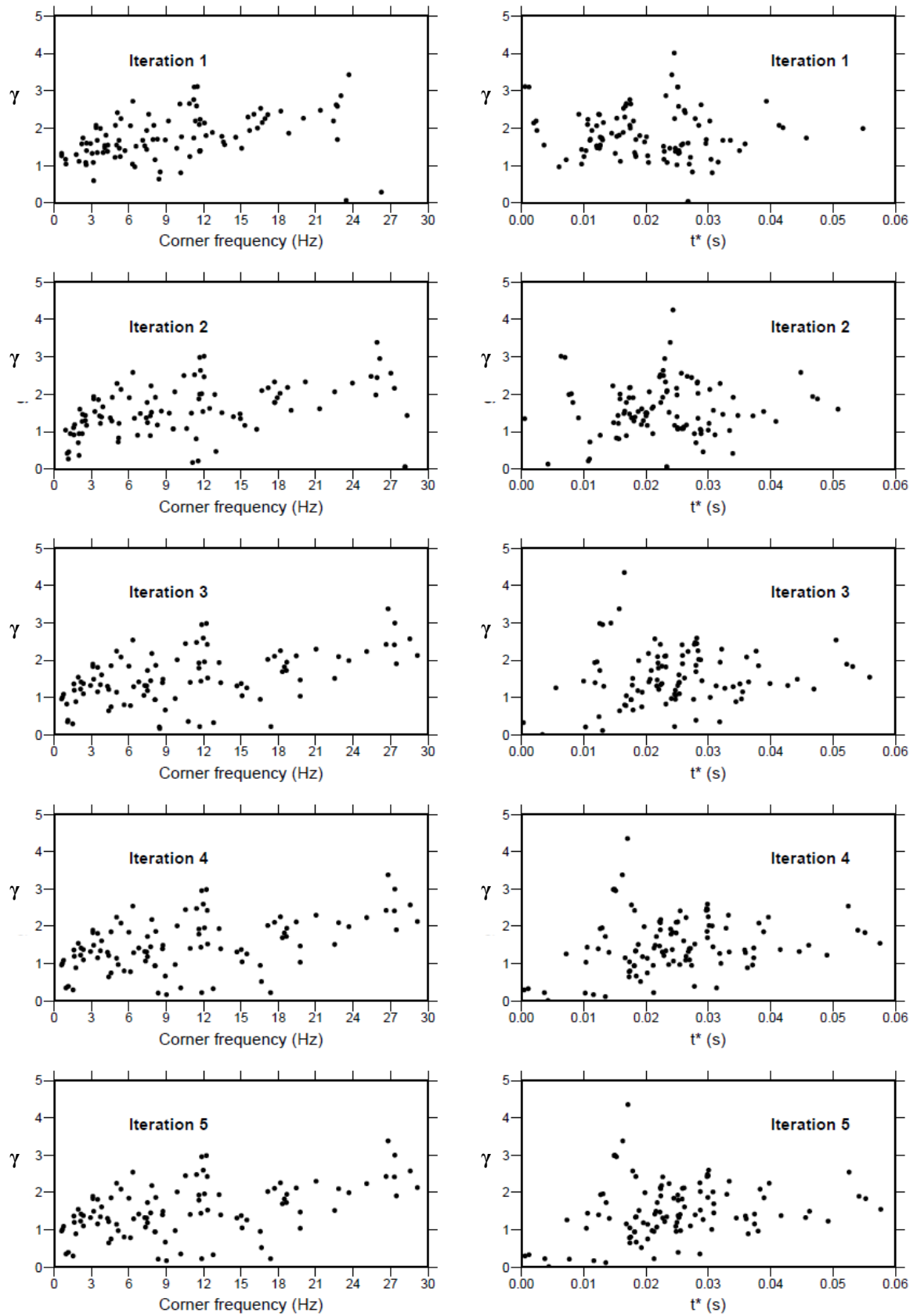


Figure 3.5: Correlation between high-frequency falloff rate γ and corner frequencies/attenuation parameter t^* at each iteration.

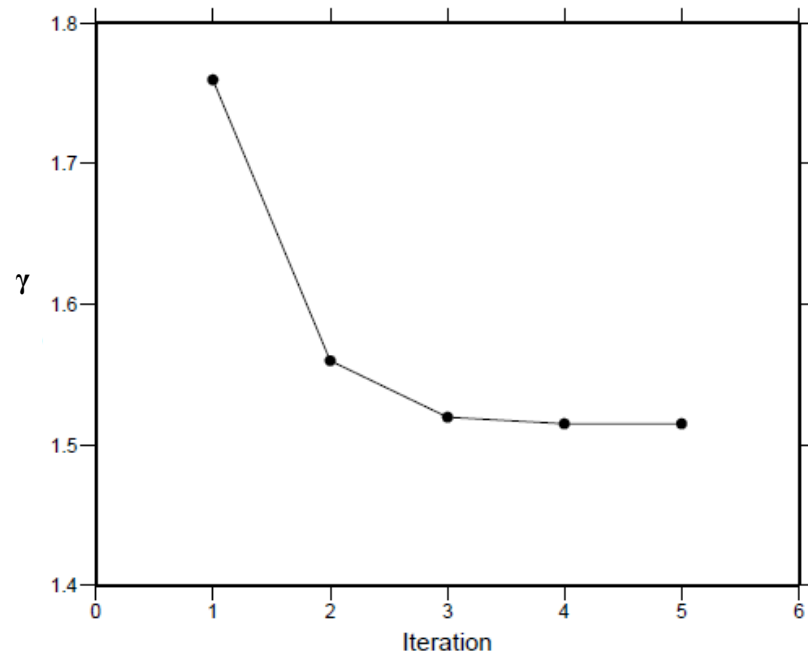
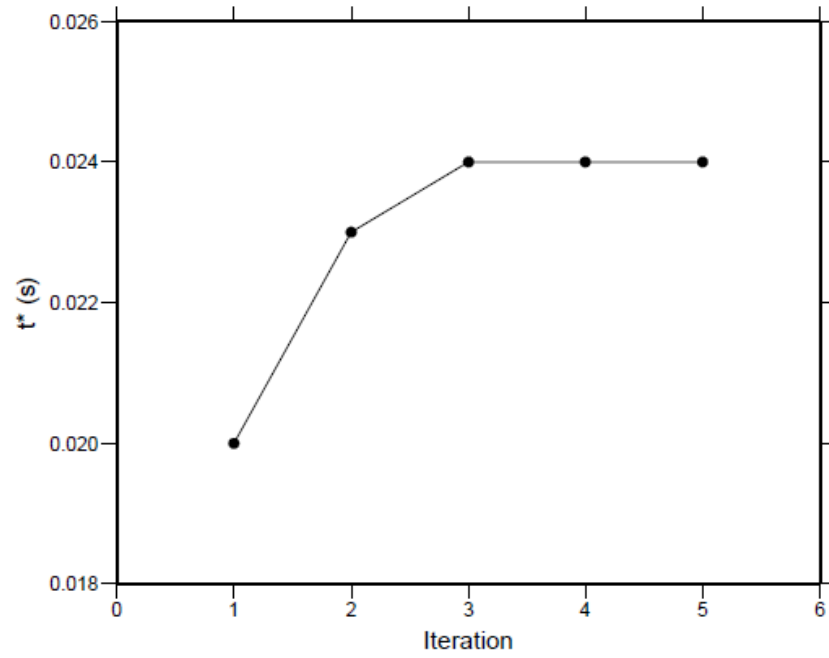


Figure 3.6: Variation of average of parameters γ and t^* estimated by each iteration.

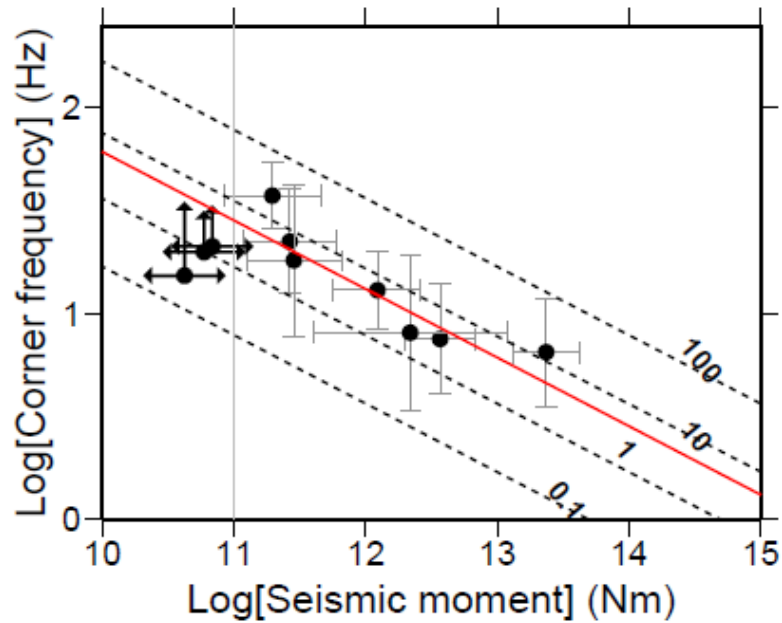


Figure 3.7: Measured seismic moments and corner frequencies for S-wave and associated uncertainties. Dashed lines refer to constant stress-drop values expressed in MPa. The red line indicates the mean value of static stress drop, while the grey line indicates the minimum value of seismic moment above which we can obtain reliable estimates of source parameters. Estimates of corner frequencies and seismic moment below the resolution threshold are plotted with arrows.

3.2 Scaling laws

In this paragraph the relationships between the source parameters estimated through the multi-step inversion procedure are shown.

3.2.1 Data collecting and processing

For the analysis proposed in the present study, the dataset collected by ISNet is further extended and integrated by the inclusion of the closest stations of the Italian Seismic Network, managed by Istituto Nazionale di Geofisica e Vulcanologia (INGV). The total number of available three-component records is 25436, relative to 689 microearthquakes with local magnitude ranging between 0.2 and 3.7 and located inside ISNet network (Fig. 3.8). These earthquakes were located using the code NLLoc (Lomax et al., 2000) and 1D velocity model of Matrullo et al. (in preparation).

Among all the available recordings only those with accurate pick P/S are selected. In

fact, after associating a weight w at pick P/S based on the uncertainties on onset time (Table 2), the following procedure is applied (Fig. 3.9):

- a) If there is manual pick P on vertical component with $w \leq 2$, the relative horizontal and vertical records are selected for the analysis, otherwise these components are removed from the database.
- b) If there is manual pick S on horizontal component with $w < 2$, then this component is considered for the calculation of displacement spectra.
- c) If the pick S does not exist or its weight is ≥ 2 , the error on hypocentral distance R is evaluated as:

$$\sigma R = \sqrt{\sigma R h^2 + \sigma R x^2} \quad (3.1)$$

where Rh and Rx are the errors along horizontal and vertical direction, respectively, obtained from the location procedure.

If $\sigma R < 2$ km, the theoretical arrival time T_s of S- phase is calculated as:

$$T_s = T_p + \frac{R}{V_p} \cdot \left(\frac{V_p}{V_s} - 1 \right) \quad (3.2)$$

where T_p is the manual pick P that satisfies the condition a), V_p and V_s are the velocity of P and S waves, respectively. The ratio V_p/V_s is set equal to 1.85 and $V_s=3$ km/s (Matrullo et al., in preparation); so V_p is equal to 5.6 km/s.

So in this case the horizontal component is used in the analysis.

If $\sigma R \geq 2$ km, the theoretical S-pick is not calculated and the analysis is done only for the P-waves.

From this procedure an optimal database with accurate P and S manual picks is obtained. This dataset is used to calculate the displacement spectra on which the multi-step

inversion procedure is applied. The signal is calculated in a 2.56-second time window around the manual P/S pick starting 0.25 s before the pick P/S (Fig. 3.10). In order to reduce distortions due to the windowing of the signals, a cosine taper function with a fraction of tapering equal to 10% is applied to the *P*- and *S*-wave time series before computing the amplitude spectrum. Next, an average moving window with a half width of 3 points is used to smooth the spectra. Finally, the *P*- and *S*-displacement spectra from velocity/acceleration time series are computed from integration/double-integration of velocity/acceleration in frequency domain. The chosen frequency band for the spectral analysis is 0.5-50 Hz and 6-50 Hz for events with local magnitude $M_L \leq 1.5$ and $M_L > 1.5$, respectively, constrained by the data-logger, the overall (sensor + data logger) instrumental response curve and by the relatively small signal-to-noise amplitude at low frequencies.

Table 2: Weight associated to onset time P/S

Weight	Uncertainties on onset time (s)
0	≤ 0.05
1	0.05 – 0.1
2	0.1 – 0.2
3	0.2 – 0.5
4	> 0.5

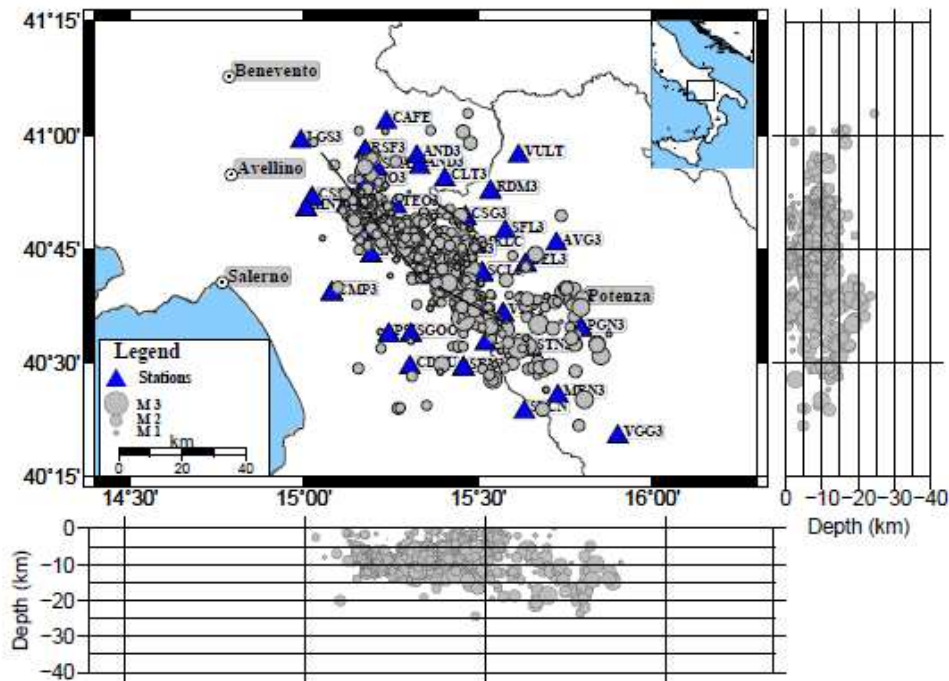


Figure 3.8: Map showing the microearthquakes analyzed in this study (grey circles) and stations of ISNet and INGV networks (solid triangles). Events are plotted with a symbol whose size is proportional to the magnitude. The three main rupture segment of the M_S 6.9, 1980 Irpinia earthquake are also drawn as from Bernard and Zollo, (1989).

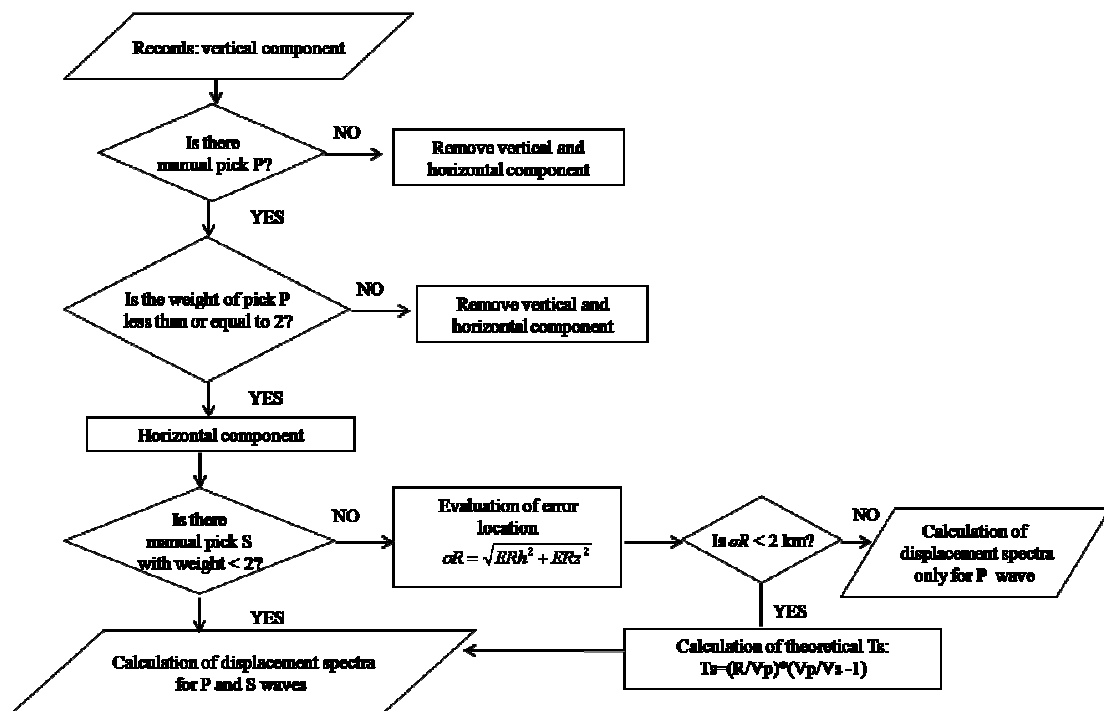


Figure 3.9: Flow chart of waveforms processing to select the best manual pick P and S.

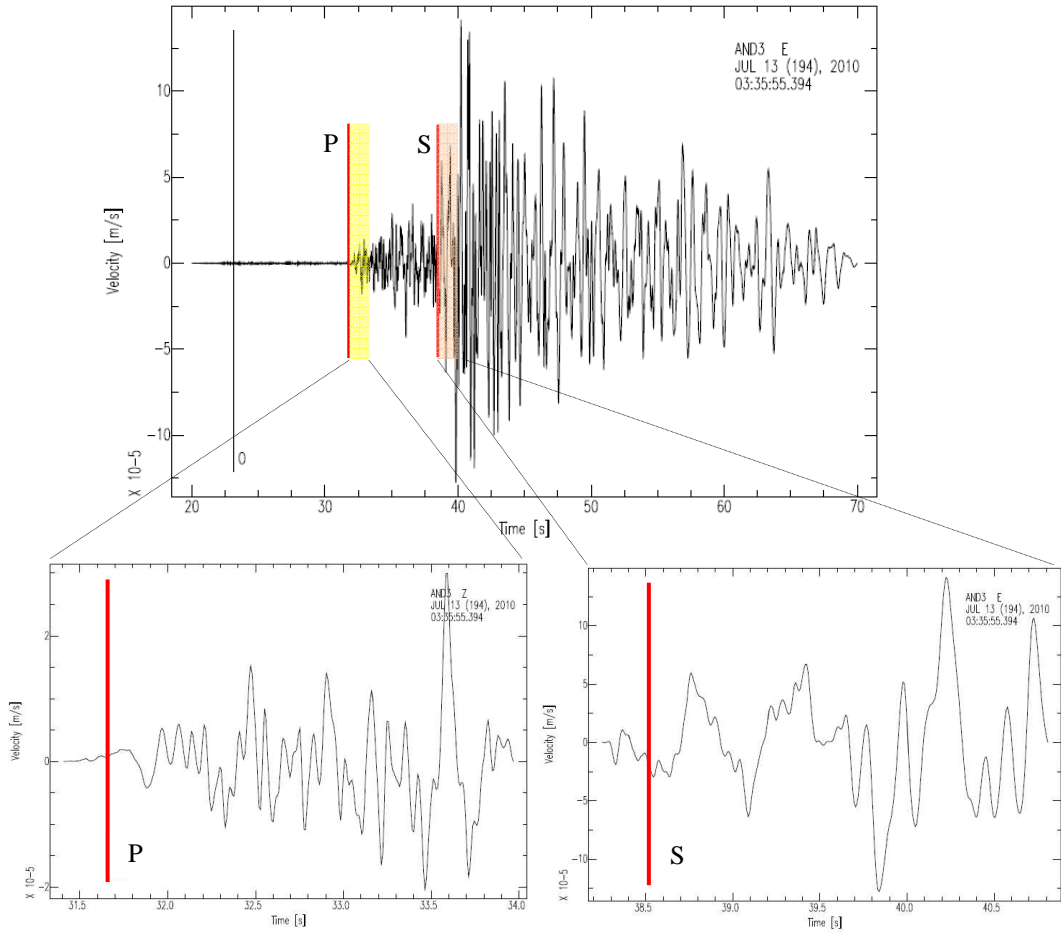


Figure 3.10: In the upper panel, yellow and red shaded areas identify the used time-windows for P- and S-wave, respectively. A zoom of these area is shown in the bottom panels.

3.2.2 P- and S- path attenuation

In the present study, it is assumed that in the analyzed frequency band (0.5-50 Hz), the parameter Q is not frequency-dependent. This hypothesis has been first verified through two analyses (Zollo et al., 2011):

1. Qualitative analysis. In particular, the displacement spectra of smallest events ($M_L < 1.2$) contained in the available dataset, at frequencies larger than the theoretical corner frequency ($> 25\text{Hz}$), have been considered. With this assumption the source spectrum can be assumed as constant and the recorded spectrum, in a log-lin representation is reduced to a linear function of frequency. As an example, figure 3.11 shows displacement spectra, corresponding to three waveforms recorded at three different stations, and five attenuation functions $t^*(\omega)$ characterized by different

values of n (cfr equation (1.21)). From a qualitative analysis, it can be noted that the case $n=0$, that is, the Q -constant model provides a better fit of the spectra with respect to the other models.

2. Statistical test. In order to obtain a more robust comparison, the differences in the fit between the attenuation models have been statistically tested. In practice, assuming the omega-square model, two different inversions have been carried out. In the first one, the displacement spectra were inverted for determining the three parameters M_o , f_c and t^* assuming a Q -constant model (which corresponds to assuming $n=0$ in equation 1.21). In the second one, a frequency-dependent Q model has been assumed for estimating the four parameters M_o , f_c , t^* and n . To establish which model best reproduces the data, we estimated the variance of the residuals (E), that is a measure of the discrepancy between the observed and theoretical displacement spectra. Finally, the best-fit model has been discriminated by using the Akaike Information Criterion (AIC) (Akaike, 1974). The criterion states that, among the best-fit models described by a different number of parameters, the one that minimizes the following function has to be selected: $AIC=2Np + N[\ln(2\pi E) + 1]$. In this equation, Np is the number of parameters used for modelling the displacement spectrum and the attenuation model while $N=N_t \cdot N_s \cdot N_c$ is the number of data. Specifically, N_t is the number of frequency samples in each spectrum, N_s is the number of analyzed displacement spectra, and N_c is the number of components (=1). As for the qualitative analysis, the results of the statistical test indicated that the Q -constant model results in the minimum of the AIC and has therefore to be considered as the best compromise between model simplicity and adherence to data (Akaike, 1974).

After the study on the frequency dependence of quality factor, the iterative multi-step procedure shown in figure 2.1 has been applied. We obtain for P- and S-wave that $\langle t_{ij_p}^* \rangle = (0.022 \pm 0.014)$ s and $\langle t_{ij_s}^* \rangle = (0.026 \pm 0.017)$ s, respectively. Figure 3.12 shows the distributions of values of t_{ij}^* .

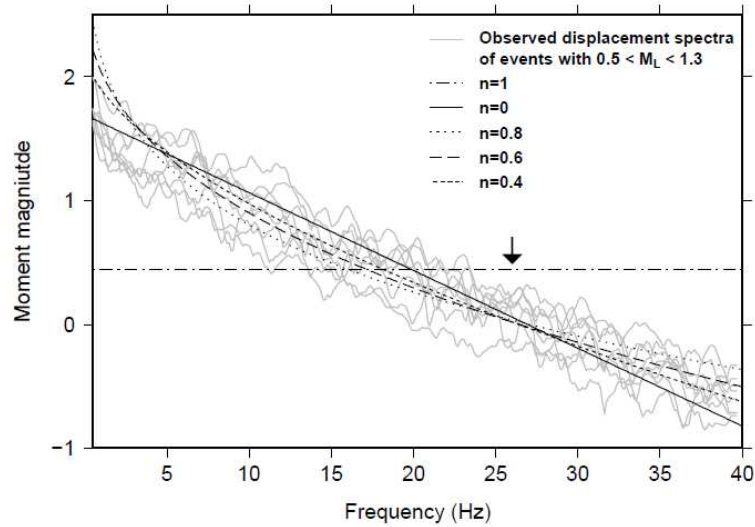


Figure 3.11: Log-lin representation of scaled displacement spectra corresponding to S waveforms recorded at 7 different stations (grey lines). Black lines correspond to five attenuation functions $t^*(\omega)$ characterized by different values of n (cfr equation (1.21)) used to test the frequency dependence of Q model against the Q -constant model corresponding to $n=0$ (black continuous line). Note that the comparison has to be done in the frequency range lower than 26 Hz (black arrow) where, in the adopted representation the source spectra is constant and the attenuation model dominates (Zollo et al., 2011).

Assuming an uniform anelastic attenuation model for the upper crust in the investigated region of southern Apennines, the estimated average values for the P- and S-wave quality factors are $Q_P = 266 \pm 254$ and $Q_S = 361 \pm 287$. Then the crustal Q_S is higher than Q_P . According to laboratory measurements, a larger P- than S-wave attenuation, corresponding to $Q_S / Q_P > 1$, is a marker for a partially fluid-saturated crust, while the inverse (e.g. $Q_S / Q_P < 1$) is expected for dry or full-saturated rock layers, (Winkler and Nur, 1979; Toksoz et al., 1979). This seismic attenuation behavior is analogous to that of shear to compressional velocity ratio, with values of V_P/V_S ratio around 1.8 or slightly larger, for partially fluid-saturated materials (Ito et al., 1979). For the analyzed area the value of ratio V_P/V_S is included in the range 1.8-1.9 (Maggi et al., 2008; Matrullo et al., 2011). Based on the mentioned results of laboratory measurements, we suggest that the observations of relatively large values of the V_P/V_S and Q_S/Q_P ratios in the analyzed region of southern Apennines, are the evidence for a highly fractured, partially fluid-saturated medium embedding the Irpinia fault zone, down to crustal depths of 15-20 km.

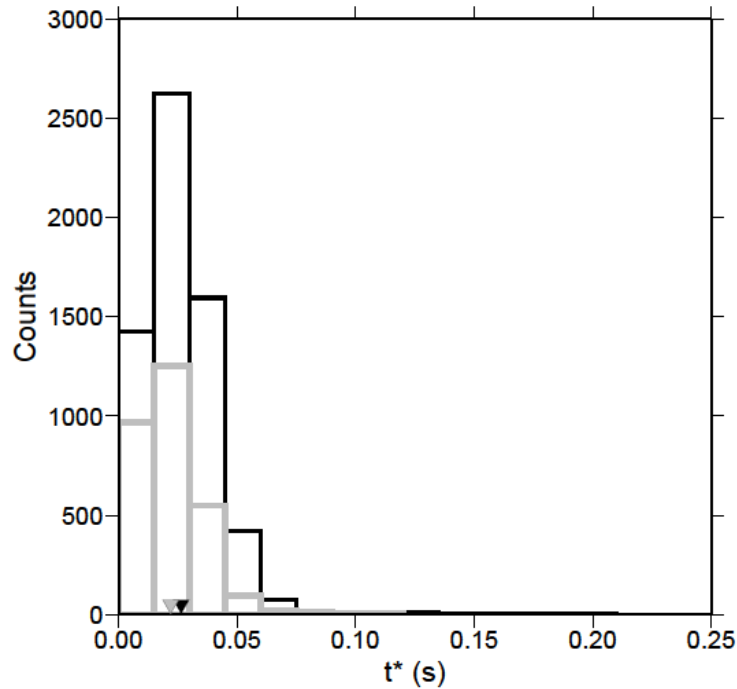


Figure 3.12: Distribution of parameter t^* for P-wave (grey) and S-wave (black). The mean values of t^* is plotted as inverse triangle (black for S-wave and grey for P-wave).

3.2.3 P- and S- site transfer functions

Given the used recursive procedure for site and attenuation correction of displacement spectra, the P and S site transfer functions account for all the effects which systematically modify the spectral shape at a given receiver, including the instrument response, local site geology, ambient noise and signal processing artifacts due to filtering or inadequate base-line corrections. For this reason we expect that the P- and S- transfer functions could be different at the same site given the different frequency content and signal-to-noise level. Figure 3.13 shows the S-site transfer functions at 8 stations of ISNet network, obtained analyzing the signals recorded by velocity and accelerometer sensors. Except at very low frequencies ($f < 1$ Hz), the transfer functions obtained from accelerometers and velocimeters look very similar. In each panel, the continuous lines refer to the average transfer function obtained from all the earthquakes recorded at that station while the dashed lines delimitate the $1-\sigma$ standard error.

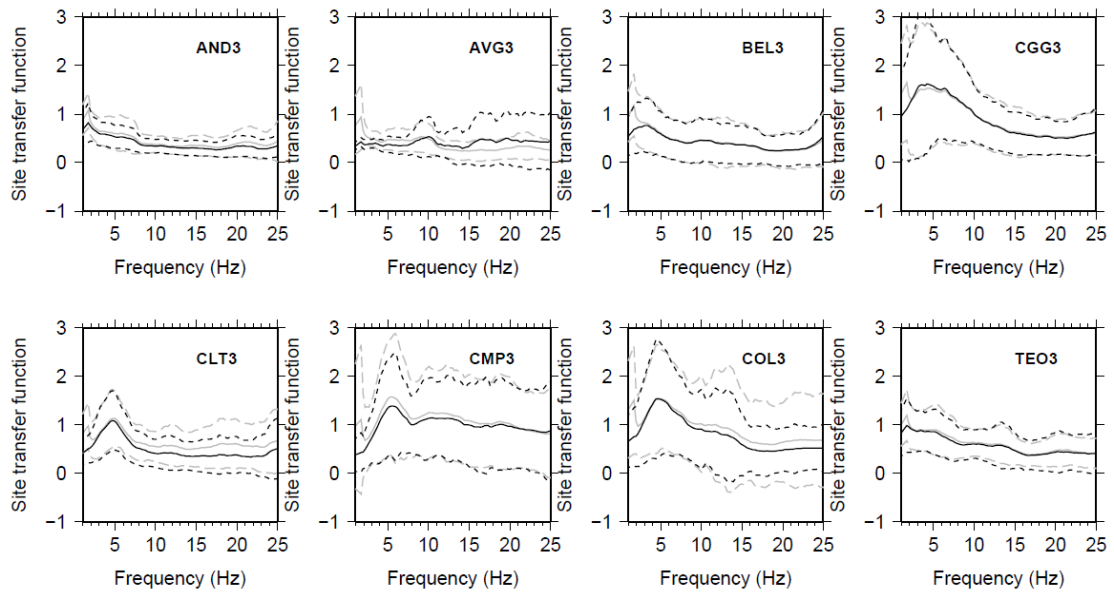


Figure 3.13: S-wave site transfer functions at 8 stations of ISNet network, obtained analyzing the signals recorded by both velocity (black lines) and accelerometer (grey lines) sensors. In each panel, the continuous lines refer to the average transfer function obtained from all the earthquakes recorded at a given station while the dashed lines delimitate the $1\text{-}\sigma$ standard error.

Almost all the sites show a constant level of amplification or attenuation with exception of stations CLT3 and CMP3 showing at least one clear peak at frequencies around 5 Hz with amplifications larger than 1.5. The presence of characteristic resonance peaks at ISNet stations due to local site amplification effects have been also pointed by Cantore et al., (2010) using H/V spectral ratio technique. P-wave transfer functions (not reported in figure) show similar resonance peaks of S waves but, due to the higher frequency content, a number of secondary peaks are also observed.

In order to verify the effect of having properly accounted for the attenuation model and site transfer functions, we compared the displacement spectra corrected and uncorrected for the attenuation and site functions. As an example, figure 3.14 shows the S-wave displacement spectra of 4 earthquakes recorded at two stations of ISNet (CMP3 and TE03) before and after the correction for path attenuation and site functions. It can be noted that the correction affects spectra both at low and high frequencies. An average variation of 0.25 unit in the moment magnitude can be noted at the two selected stations together with a shift in the corner frequency values which is more effective for the smallest earthquakes.

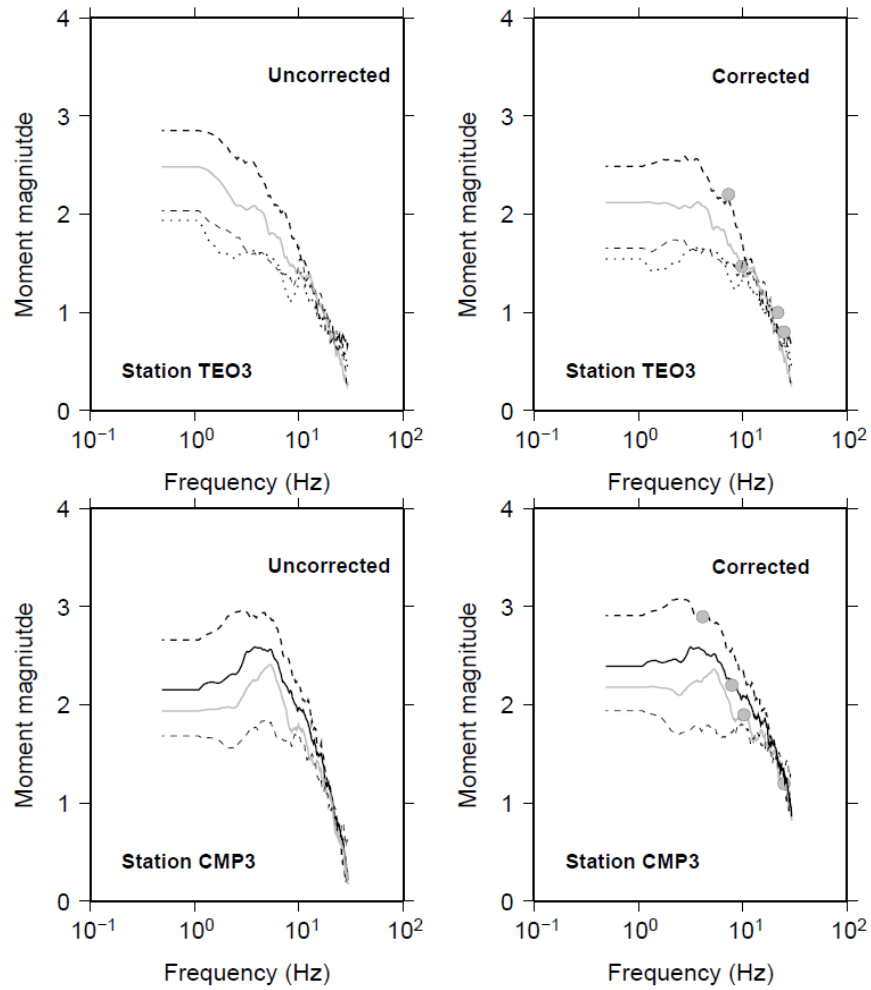


Figure 3.14: S-wave displacement spectra of 4 earthquakes recorded at two stations of the ISNet network. Upper panel refers to the station TEO3 and lower panel refers to the station CMP3. For both the two stations left panel refer to scaled spectra before the correction for the attenuation and site effect obtained from the iterative procedure. Right panels refer to the same spectra corrected for the attenuation and site effect and superimposed grey dots identify the corner frequencies.

3.2.4 Seismic moment, source radius and static stress drop

Once we have obtained the spectral parameters low-frequency spectral level and corner frequency, we can calculate the seismic moment, the source dimension and the stress released by faulting.

In order to account for the results of resolution test, the scaling laws are shown only for events with seismic moment $M_0 \geq 10^{11}$ Nm. Moreover, only events recorded at a

minimum of 5 stations have been considered. Figure 3.15 shows a log-log representation of the corner frequency vs seismic moment for S-waves (top panel) and P-waves (bottom panel). The grey dots indicate the estimations of source parameters obtained for each analyzed event, while the black/white circles with the associated uncertainties are obtained by averaging the data grouped in a 0.3 logarithm of seismic moment bin. This value of bin has been chosen by considering the average of uncertainty associated with the logarithm of seismic moment. The constant stress drop lines at values 0.1 to 100 MPa are shown in the same figure, where stress drop is estimated using the Madariaga's model for the earthquake rupture radius. We observe the self-similar scaling of the corner frequency in the whole range of seismic moment for both P- and S-waves.

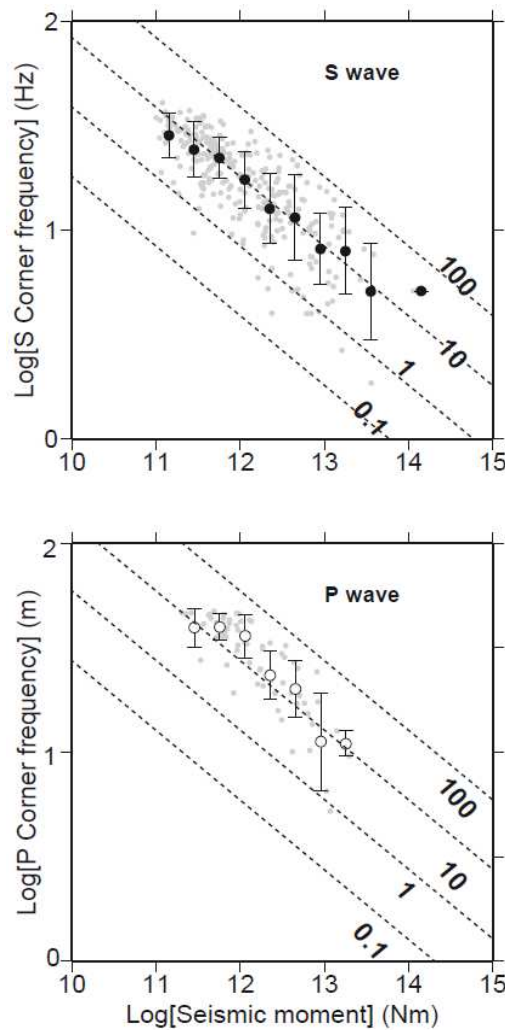


Figure 3.15: Log of corner frequency versus log of seismic moment for S-waves (top panel) and P-waves (bottom panel). The black/white circles with the associated uncertainties are obtained by averaging the data (grey dots) grouped in a 0.3 logarithm of seismic moment bin.

The earthquake source radius is then determined by the arithmetic mean of all the available corner frequency estimates (ref. relation 1.23). Source radii decrease with decreasing moment, confirming the self-similarity (Fig. 3.16). P- and S-wave estimates of source parameters are very consistent, which is a further confirmation of the robustness of such estimates.

We estimate the static stress drop $\Delta\sigma$ from the seismic moment and source radius using the relation (1.24). Stress drops appears to be invariant with earthquake moment (Fig. 3.17), with a value of (8.9 ± 2.0) MPa which corresponds to an average Brune's static stress drop value of (1.6 ± 0.4) MPa. A self-similar scaling of static stress drop has been found in southern California by Abercombrie et al. (1995) from recording at depth of 2.5 km Cajon Pass and Prieto et al. (2004) from Earth surface recordings of microearthquakes by the Anza seismic network. In Central Apennines, Italy, in a dominant normal faulting tectonic environment, several studies analyzed the source parameter scaling relationships from the aftershock recordings of the 1997 Umbria-Marche seismic sequence. Using different modeling approaches and sub-sets of the same data archive, Bindi et al., (2001) found a self-similar scaling of static stress drop (Brune's stress drop 2.6 MPa).

For a limited number of events, we compared P and S corner frequencies as shown in figure 3.18. Here the black circles with the associated uncertainties are obtained by averaging the data grouped in a 2 Hz S-corner frequencies bin. We find that the P corner frequencies are systematically higher than those estimated for S waves from the same earthquakes. The ratio f_c^P/f_c^S is about 2.0 ± 0.5 , consistent within the error with the model of Madariaga (1976). In fact, Molnar et al. (1973) and Madariaga (1976) present source model with $1.5 < f_c^P/f_c^S < 1.73$, whereas Savage (1974) and other argue that such a shift is incompatible with Haskell-type source models and must result from attenuation. Accounting for attenuation, in this study $f_c^P > f_c^S$ and we can assert that the corner frequency shift observed here is principally a source effect, as proposed by Hanks (1981).

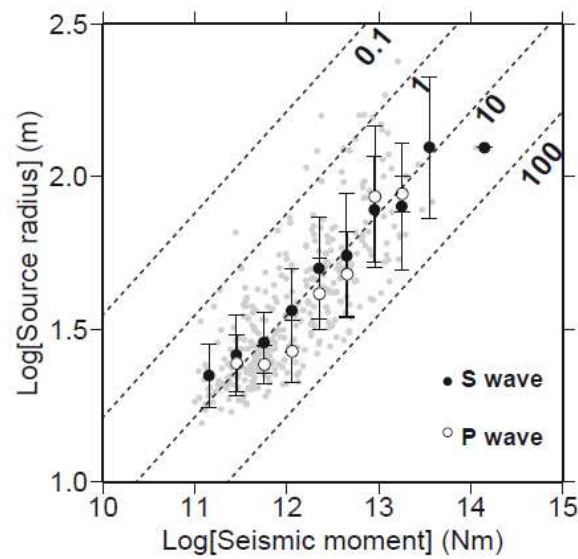


Figure 3.16: Log of source radius versus log of seismic moment. Dashed lines show the constant stress-drop values expressed in MPa. The black/white circles with the associated uncertainties are obtained by averaging the data (grey dots) grouped in a 0.3 logarithm of seismic moment bin.

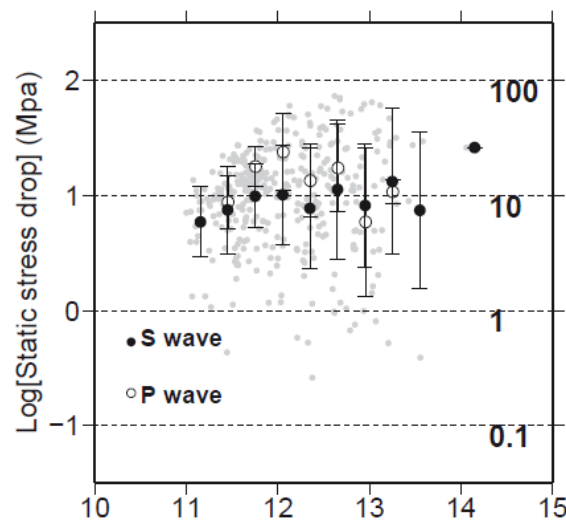


Figure 3.17: Log of static stress drop versus log of seismic moment. Dashed lines show the constant stress-drop values expressed in MPa. The black/white circles with the associated uncertainties are obtained by averaging the data (grey dots) grouped in a 0.3 logarithm of seismic moment bin.

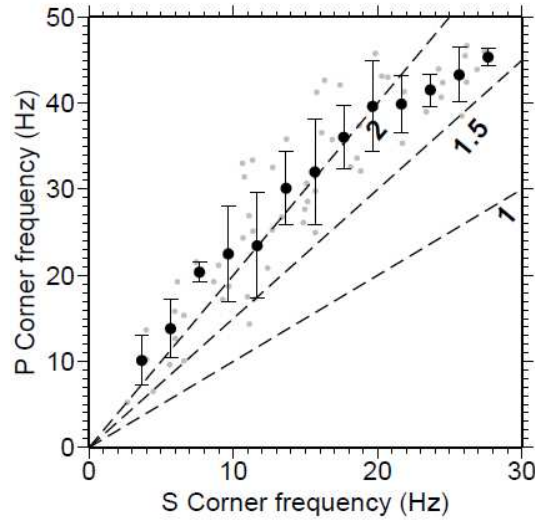


Figure 3.18: P-wave and S-wave measured corner frequencies for a limited portion of the analyzed dataset. Dashed lines show different P/S corner frequencies ratio.

3.2.5 Moment and local magnitude

In figure 3.19 the values of moment magnitude M_w (calculated for S-wave) as a function of local magnitude M_L are shown. The values of local magnitude for earthquakes recorded by the network ISNet were obtained from Bobbio et al. (2009). The data (grey dots) are grouped in a 0.3 local magnitude bin (black circles). The black line represent the line of best fit, while the dotted line corresponds to $M_w = M_L$. The resulting relationship between moment and local magnitude is:

$$M_w = 0.63 (\pm 0.04) M_L + 0.95 (\pm 0.09) \quad (3.3)$$

We observe a systematic underestimation of moment magnitude by local magnitude.

In theory, M_w and M_L should provide the same value which means that

$$M_w = \frac{2}{3} (\text{Log} M_0 - 9.1) = M_L \quad (3.4)$$

According to Deichmann (2006), due to inappropriate correction of instrumental and

attenuation effects, the local magnitude causes the underestimation of moment magnitude.

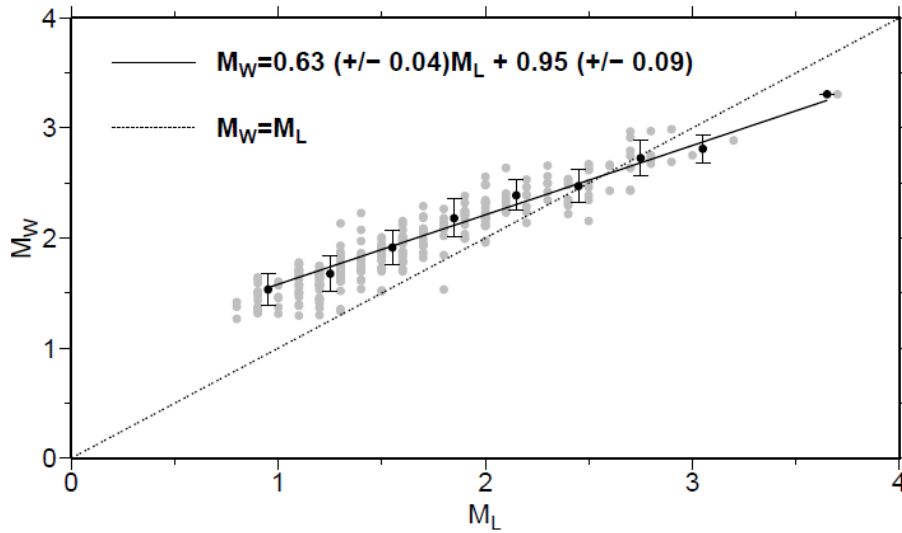


Figure 3.19: Moment magnitude (M_w) versus local magnitude (M_L) relationship obtained from a best fit analysis. The black circles with the associated uncertainties are obtained by averaging the data (grey dots) grouped in a $0.3 M_L$ bin. The dotted line corresponds to $M_w = M_L$.

3.3 Conclusion

Important findings can be summarized as follows:

1. By the resolution's test we obtained the minimum values of seismic above which we can obtain reliable estimates of source parameters, that is $M_0 \geq 1e11 \text{ Nm}$ ($M_w \approx 1$)
2. Frequency-independent attenuation model: through statistical test we verified that the constant-Q model has to be preferred to frequency dependent Q -models
3. Earthquake self-similarity: we observed a constant stress-drop scaling of source parameters. The average Madariaga's static stress drop is about 8.9 MPa, which corresponds to Brune's stress drop of about 1.6 MPa. The ratio between P- and S- corner frequencies is comparable with the theoretical value.
4. We observed the discrepancy between local and moment magnitude: M_L causes the underestimation of M_w .

Section C Time domain

Chapter 4 Empirical Green Function's (EGF) Approach

4.1 Introduction

Knowledge of the seismic source requires modeling the propagation between the source and the receiver (Green's functions). Under the hypothesis of linear wave propagation, the Green's functions may also be replaced by the records of small earthquakes occurring on the same fault with the same focal mechanism and the same stress drop, commonly referred to as Empirical Green's functions (EGFs).

As seen in the previous section, the analysis of the source parameters is often complicated by their spectral properties at high frequencies, where path and site effects are not easily distinguished from the source characteristics. One way to overcome this problem is to determine the EGFs that consent to represent the contribution of propagation and site effects to signal avoiding the use of approximate velocity models. In fact, the displacement spectra of small events are characterized by high corner frequency below than the source can be assimilated to spatial and temporal function delta of Dirac. Then, in this range of frequency, the signal is the response of the medium to impulses in the source region.

The use of small events as EGFs was first proposed by Hartzell (1978). It was subsequently used and developed by Mueller (1985), Fukuyama and Irikura (1986), Mori and Frankel (1990), Ammon et al. (1993), Velasco et al. (1994), Courboux et al. (1997a), and Ihmlè (1996). The idea is to deconvolve the mainshock from the smaller event (EGF) to obtain a relative source time function (RSTF) at each considered station. The durations of each RSTF are then examined to retrieve some interesting properties regarding the extent and rupture velocity of the event.

In this chapter the deconvolution method (Vallée, 2004) is explained. It takes into account various physical constraints of the RSTF to stabilize the deconvolution. The method is based on the projected Landweber method, introduced in seismology by Bertero et al. (1997), to which we have added an important constraint: the area of the

RSTF, which represents the scalar moment of the earthquake, has to remain the same at all stations.

4.2 Theory of EGF analysis

By starting from the representation theorem, for a large earthquake of moment M_1 , we can write:

$$U_i^1(\vec{x}, \omega) = -M_{pq} M_1 i k_q G_{ip}(\vec{x}, \vec{\xi}_0, \omega) \int_S f(\vec{\xi}, \omega) e^{-i\vec{k} \cdot (\vec{\xi} - \vec{\xi}_0)} d^2 \xi \quad (4.1)$$

where G_{ip} denotes the spatial derivative of the Green function. Here we assume that 1) the Green function G_{ip} is the same for all the points of the fault except for a phase shift $\vec{k} \cdot (\vec{\xi} - \vec{\xi}_0)$ due to the varying distance between source and receiver (far-field approximation), 2) the earthquake has a constant mechanism. M is a unit tensor independent of $\vec{\xi}$ and ω , $f(\vec{\xi}, t)$, the inverse Fourier transform of $f(\vec{\xi}, \omega)$, is a causal, positive scalar function, monotonically increasing over $[0, D]$, where D is the unknown duration of the source, and constant elsewhere (for more details see Vallée 2004).

For a smaller earthquake of scalar moment M_0 , with same location and similar focal mechanism of large earthquake, $f(\vec{\xi}, \omega)$ can be approximated by

$$f(\vec{\xi}, \omega) = \delta(\vec{\xi} - \vec{\xi}_0) TF(H(t)) = \frac{\delta(\vec{\xi} - \vec{\xi}_0)}{i\omega} \quad (4.2)$$

where $TF(H(t))$ is the Fourier transform of the Heaviside function, which leads to

$$U_i^0(\vec{x}, \omega) = -M_{pq} \frac{M_0}{i\omega} i k_q G_{ip}(\vec{x}, \vec{\xi}_0, \omega) \quad (4.3)$$

Therefore, by deconvolving equation (4.1) from equation (4.3), we obtain the RSTF, defined as F_θ in the equations:

$$\begin{aligned}
F_{\theta}(\omega) &= \frac{M_1}{M_0} i\omega \int_s f(\vec{\xi}, \omega) e^{-i\vec{k} \cdot (\vec{\xi} - \xi_0)} d^2 \xi = \\
&= \frac{M_1}{M_0} i\omega \int_s f(\vec{\xi}, \omega) e^{-i\omega \frac{\vec{u}}{v_{\phi}} \cdot (\vec{\xi} - \xi_0)} d^2 \xi
\end{aligned} \tag{4.4}$$

where v_{ϕ} , the phase velocity and \vec{u} the wave propagation direction, are assumed constant. This assumption compels us to study separately each wave type in the EGF analysis. The RSTF is a positive, bounded-support function and its duration will also depend on the position of the station, the phase, and the rupture velocity but it will of course remain bounded. Another important property of the RSTF is that its integral value is independent of the stations or the wave type used in the deconvolutions and is equal to the relative moment between the mainshock and the EGF.

4.3 Projected Landweber method

The deconvolution method of Vallée (2004) is based on the approach of Bertero et al. (1997), who developed a simple method to include positivity and temporal constraints on the RSTFs, based on the Landweber method. It was shown by Bertero et al. (1995) that the latter method was slower but more accurate than conjugate gradient methods.

Called U^1 and U^0 the mainshock and EGF waveform, respectively, the problem is to identify the RSTF F_{θ} verifying

$$\|U^0 * F_{\theta} - U^1\| = \text{minimum} \tag{4.5}$$

or equivalently

$$U^{0*} * U^0 * F_{\theta} = U^{0*} * U^1 \tag{4.6}$$

(e.g., Bertero, 1989), where U^{0*} is the adjoint operator of U^0 . Through mathematical manipulations, equation (4.6) can thus be written as

$$F_\theta = F_\theta + U^0(-t) * (U^l - U^0 * F_\theta) \quad (4.7)$$

In an iterative scheme, the last equation becomes

$$F_\theta^{(n+1)} = F_\theta^n + \tau U^0(-t) * (U^l - U^0 * F_\theta^n) \quad (4.8)$$

where τ is the relaxation parameter which must satisfy the condition $0 < \tau \leq 2/(\sup_\omega |U^0(\omega)|)^2$ and is classically chosen equal to $1/(\sup_\omega |U^0(\omega)|)^2$.

Let us suppose that we know that the RSTF belongs to some closed and convex set C . Then equation (4.8) can be modified as follows:

$$F_\theta^{(n+1)} = P_c(F_\theta^n + \tau U^0(-t) * (U^l - U^0 * F_\theta^n)) \quad (4.9)$$

where P_c denotes the metric projection on C . In the absence of noise, F^n is shown to converge, but only weakly, toward the expected solution of

$$\|U^0 * F_\theta - U^l\| = \text{minimum}, \quad F_\theta \in C \quad (4.10)$$

Bertero et al. (1997) defined C as the set of nonnegative causal functions that are zero for $t > D$. However, we can be even more restrictive and let C be the set of nonnegative causal functions that are zero for $t > D$ and for which the integral over $[0D]$ is equal to M_1/M_0 . It can be immediately verified that the newly defined set that we call C_m is closed and convex. We now must define the projection P_{C_m} itself in order to compute equation (4.9). Given a function h , it can be shown that $P_{C_m}(h)$ can be naturally

computed, that is, we essentially add a proper, additive constant to h to derive $P_{Cm}(h)$ from h . it is shown that P_{Cm} is approximated by:

$$P_{Cm}h(t) = \begin{cases} P + \left(h(t) + k \frac{M' - M_1/M_0}{\alpha D} \right) & \text{if } t \in [0D] \\ 0 & \text{elsewhere} \end{cases} \quad (4.11)$$

where k is a positive real number.

Given P_{Cm} , the computation procedure is again completely as the one of Bertero et al. (1997): we start from $F_\theta^0 = 0$, compute equation (4.8) in the frequency domain, and come back to the time domain to use P_{Cm} as defined by equations (4.9) and (4.11). We then obtain F_θ^1 and repeat the operation, transforming into the frequency domain to compute again equation (4.8) and so on. The scheme (4.9) is semiconvergent, that is, it approaches the solution before diverging again. However, the minimum seems very flat, and good results are obtained after a few hundred iterations.

4.4 Conditions of applicability EGF method's

As mentioned above, an empirical Green's function is a recorded three-component set of time-histories of a small earthquake whose source mechanism and propagation path are similar to those of the master event. This definition requires that:

1. we must find a smaller earthquake than the mainshock so that equation (4.2) is verified. In reality, the small-event source time function has a finite duration, and therefore a high-frequency-limited spectrum. This high-frequency limit is represented by the corner frequency of the small event and corresponds to the maximum resolution that we can obtain on the large-event rupture process.

To establish how much is the difference in magnitude between the EGF and master event, a synthetic test was performed. It has been shown that the EGF optimal magnitude is about 1 units smaller than the mainshock.

2. The mechanism and location must be similar — in case of difference between both events, it is possible to correct for these effects (Ihmlè, 1996), but it adds some

complexity to the procedure. Consequently, waves that radiate from the nucleation points of the two events should cross exactly the same medium. In reality the two events are slightly shifted in space, and a heterogeneity in the source region can be detected by only one of the events. This is a restriction of the EGF method, but the resulting error is smaller than the one that would result from using a calculated Green's function.

3. The mainshock must have a constant mechanism so that the Green's function may be assumed to be consistent over the whole source zone.

The conditions listed above are very important in particular for near source data. In fact, for regional and/or teleseismic data the differences in focal mechanism and location are attenuated by large distances between seismic source and receiver, and so these conditions can be considered negligible. As we will see in this chapter, to identify potential EGF the near-source data processing provides several steps before the deconvolution, i.e. 1) localization using the NLLoc code (Lomax et al., 2000), 2) the calculation of focal mechanisms with FPFIT code (Reasenberget al., 1985) and 3) the study of the stability of the polarization for the optimal choice of range frequency to be used in the deconvolution process.

4.4.1 Difference in magnitude between master event and EGF: synthetic test

To determine the difference in magnitude between the mainshock (main) and EGF, synthetic seismograms were generated with a moment magnitude ranging between 0.5 and 3. We used the AXITRA code (Coutant, 1989) based on the discrete wavenumber method (Bouchon, 1981) to generate the synthetic seismograms.

For each moment magnitude a different discretization of the fault plane was chosen (Table 3), keeping fixed the distance D between the elementary sources to 9 m and with strike, dip and rake respectively equal to 285° , 40° and -110° . It is assumed a unilateral rupture with uniform velocity rupture $v_r=0.9\cdot\beta$ and the velocity model used is model of Amato and Selvaggi (1993). The hypocentral coordinates have been set equal to 40.7720°N , 15.3135°E and 17.25 km for all events generated by using the actual geometry of the Irpinia Seismic Network (ISNet) (Fig. 4.1).

The deconvolution code of Vallée (2004) was applied to the synthetic

seismograms. In particular, the following pairs main-EGF were considered:

Case 1. main of $M_w=1$ and EGF of $M_w=0.5$

Case 2. main of $M_w=3$ and EGF of $M_w=2$

Case 3. main of $M_w=3$ and EGF of $M_w=1$

Case 4. main of $M_w=3$ and EGF of $M_w=0.5$

For each pairs main-EGF the RSTF was determined for 21 stations in the S- and P- wave time window and the misfit between the real mainshocks and the reconstituted mainshock is evaluated. It is obtained by reconvolution of the RSTF with the EGF, as a function of the allowed duration of the RSTF. This misfit is a good indicator of the quality of the obtained deconvolution. The time at which the function becomes flat gives the simplest (i.e., shortest) RSTF able to well describe the seismic source (Fig. 4.2).

As it can be seen from figure 4.3, since in case 1 the difference in magnitude is 0.5, we are not able to distinguish the two events and therefore the misfit function is zero. In case 2 and 3, however, the misfit function becomes flat at $\tau = 0.1$ s. This value represents the optimal duration of RSTF. Increasing the difference in magnitude between the main and the EGF (*case 4*), the accuracy in the estimation of the optimal duration increases. In the latter case, τ is equal to 0.15 s.

So we can conclude that the minimum difference in magnitude between mainshock and EGF is equal to 1. Figure 4.4 shows the RSTFs of the main for each station obtained in the *case 3*. Therefore for $M_w=3.0$ we observe that the optimal duration is $\tau = 0.1$ s. It is essential to obtain accurate estimates of the source size.

Table 3: Discretization of fault for generated event with different moment magnitude

M_w	N° sources
0.5	2
1	3
2	10
3	21

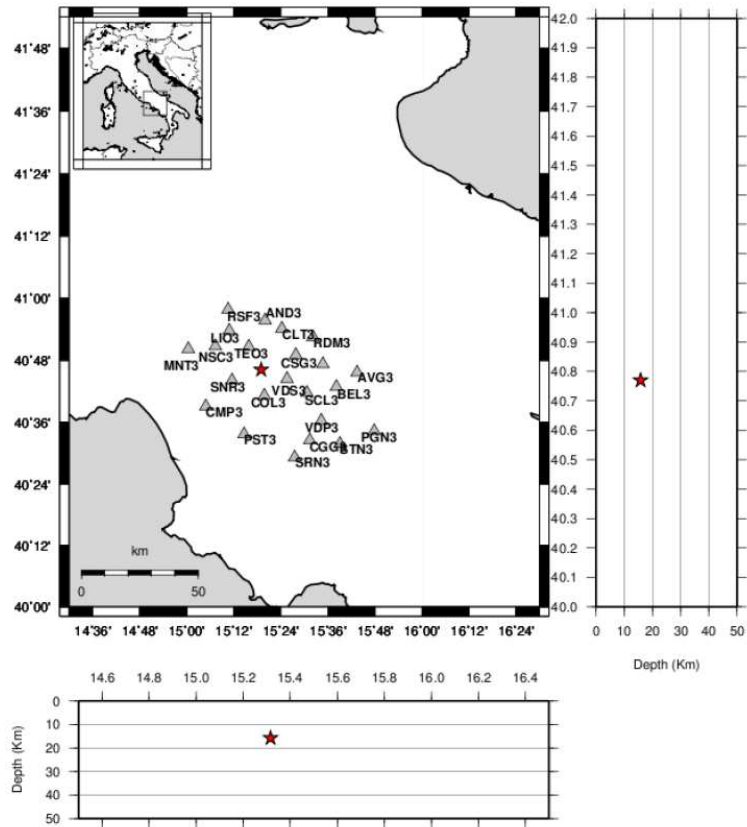


Figure 4.1: Map showing the location of generated event (star) with different magnitude and the stations of ISNet network.

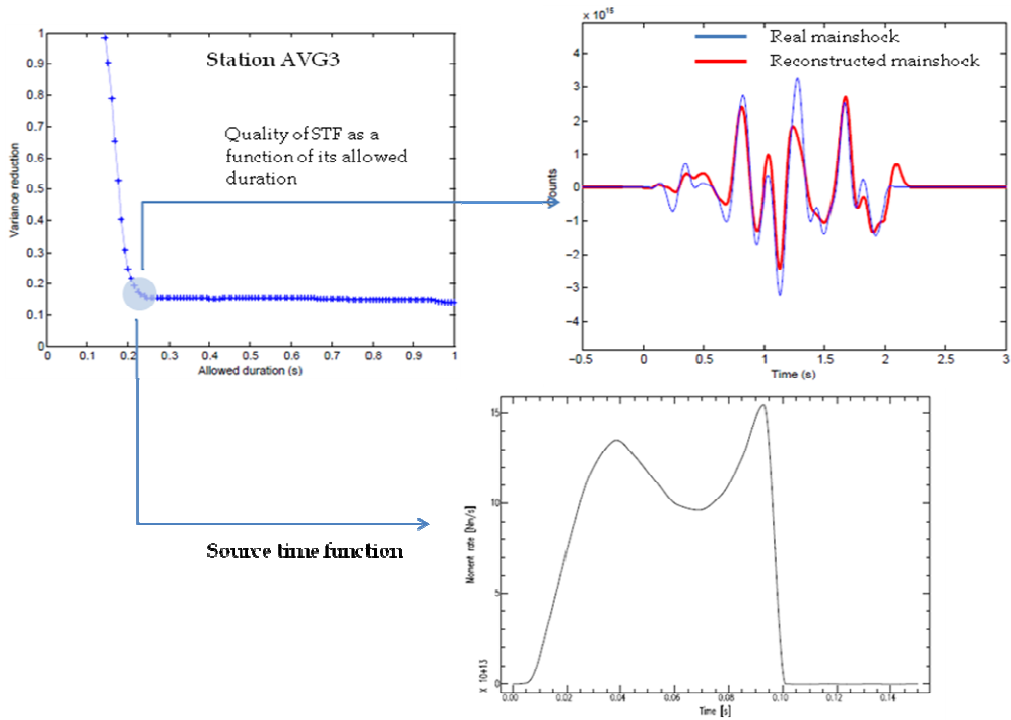


Figure 4.2: Illustration of the deconvolution technique for S-wave at station AVG3 of ISNet network.

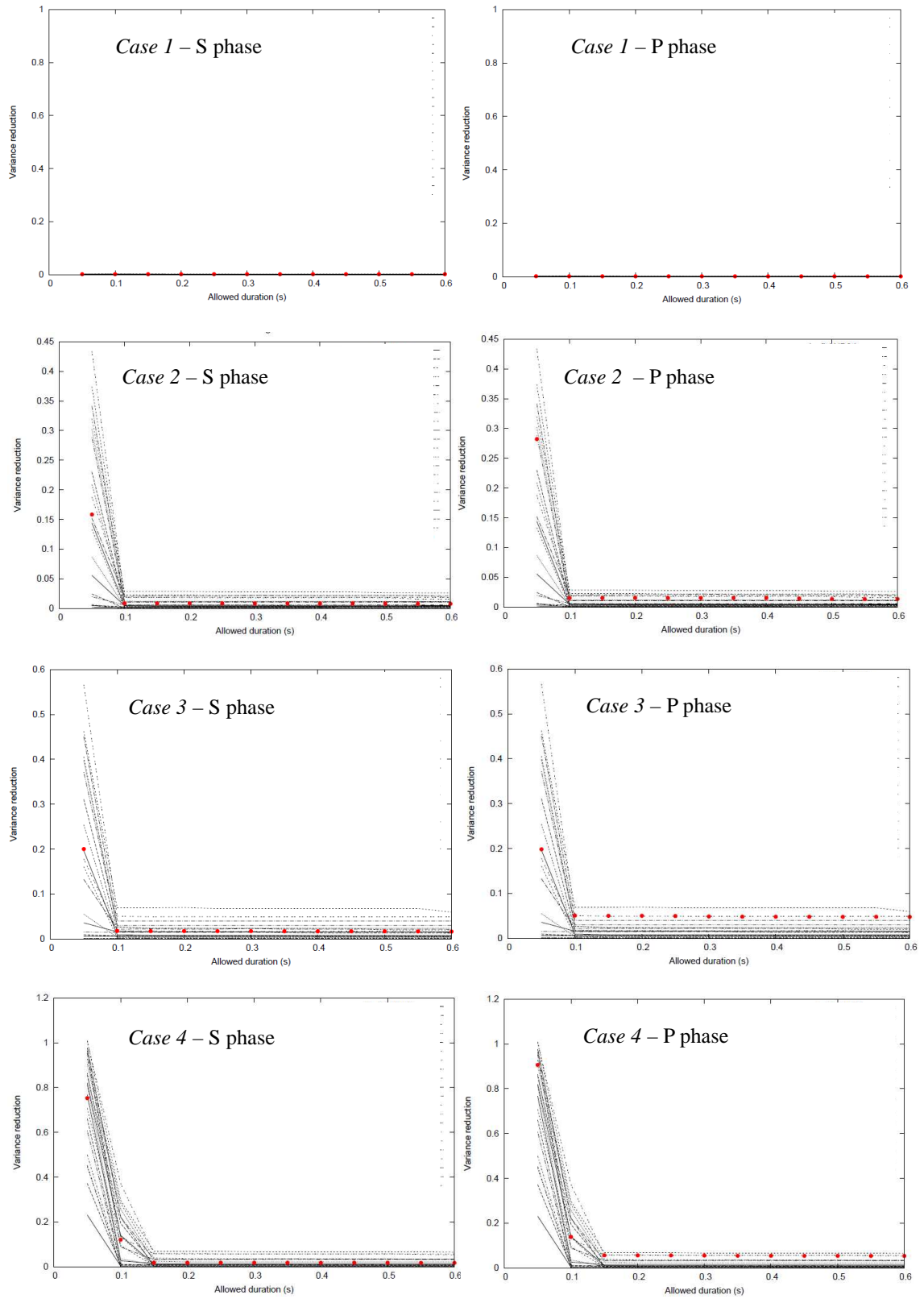


Figure 4.3: For each case the misfit between the real mainshocks and the reconstituted mainshock obtained from reconvolution of the RSTF with the EGF, is shown as a function of the allowed duration of the RSTF. Red dots represent the mean values of misfit curve obtained for each station.

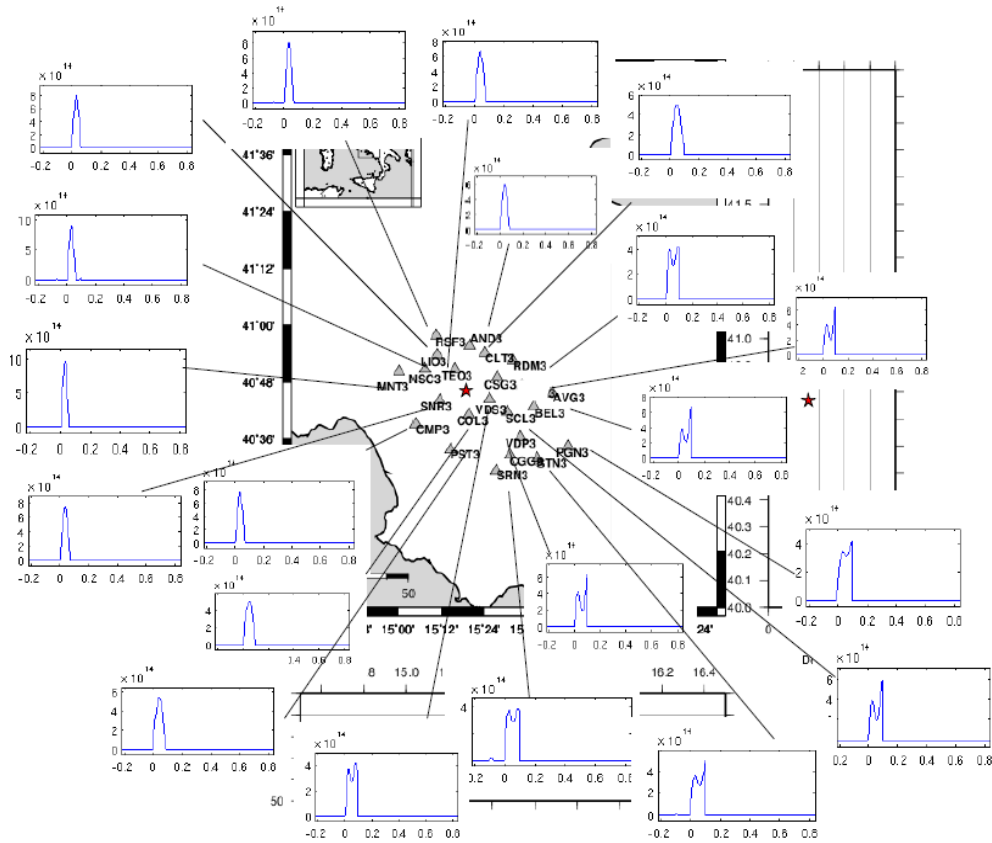


Figure 4.4: Map of RSTFs for each station.

4.4.2 Processing of near-source data

As mentioned in previous paragraphs the EGF approach suffers from certain limitations related to the selection of valuable Empirical Green Function, especially for small events. To select the best EGF, the data processing includes the estimation of the event location and the determination of the focal mechanism.

Considering only P-wave arrival time, first the NLLoc code (Lomax et al., 2000) has been applied to each pair master event – EGF, previously selected according to the difference in magnitude. After, the focal mechanisms were calculated using code FPFIT (Reasenberget al., 1985). Only the pair master event – EGF with similar location and focal mechanism have been chosen. Finally, the study of stability of polarization is done

to choose the optimal range of frequency to use in the deconvolution process.

To set the low-frequency f_{min} it is necessary to know the corner frequency of events pair. In fact, the low-frequency limit is represented by the corner frequency of master event f_c^{main} , i.e. $f_{min} \ll f_c^{main}$ (Fig. 4.5). In this way also the condition (4.2) is verified and so the source of EGF can be assimilated to spatial and temporal function delta of Dirac. Then, in this frequency range, the signal of EGF represents the response of the medium to impulses in the source region.

To set the high-frequency f_{max} we study the polarization. By applying different range of frequency, the stability of polarization is observed and the f_{max} at which it becomes stable in time is chosen as high-frequency limit. The polarization direction of the wave velocity is determined directly from the diagrams since it coincides with the azimuth of the motion associated with the first arriving wave. Figure 4.6 shows an example of the diagram of polarization obtained by horizontal components $sisE$ and $sisN$ for $f_{max} = 10$ Hz. This components are aligned according to the theoretical arrival time of S-wave (red lines). In this case it is clear that until about 3.8 s the polarization is stable indicating that 10 Hz is the optimal high-frequency limit.

This study also provides information on the time window to be selected from the S phase in the deconvolution process. In fact, as we can see in figure 4.6, the angle of polarization changes sharply after about 3.8 s indicating the presence of secondary phase. To obtain reliable RSTFs it is necessary not to introduce several phase in the time window. So in the case shown in figure 4.6 the optimal duration of time window to be selected from S-phase is about 3 s.

Selected the range of frequency, the deconvolution method is applied to each pair master event – EGF to obtain the RSTFs.

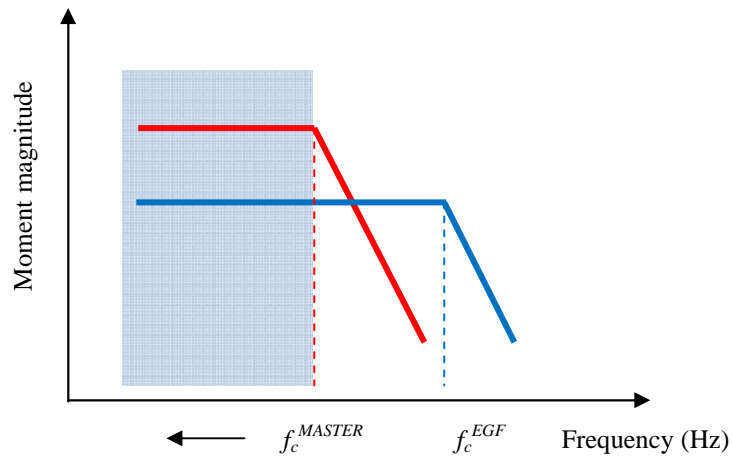


Figure 4.5: Scheme to understand the choice of low-frequency limit f_{min} . The displacement spectra of master event (red) and EGF (blue) are shown. The relative corner frequency are indicated. f_{min} must be smaller than f_{min}^{MASTER} where the two signal are equal (blue area).

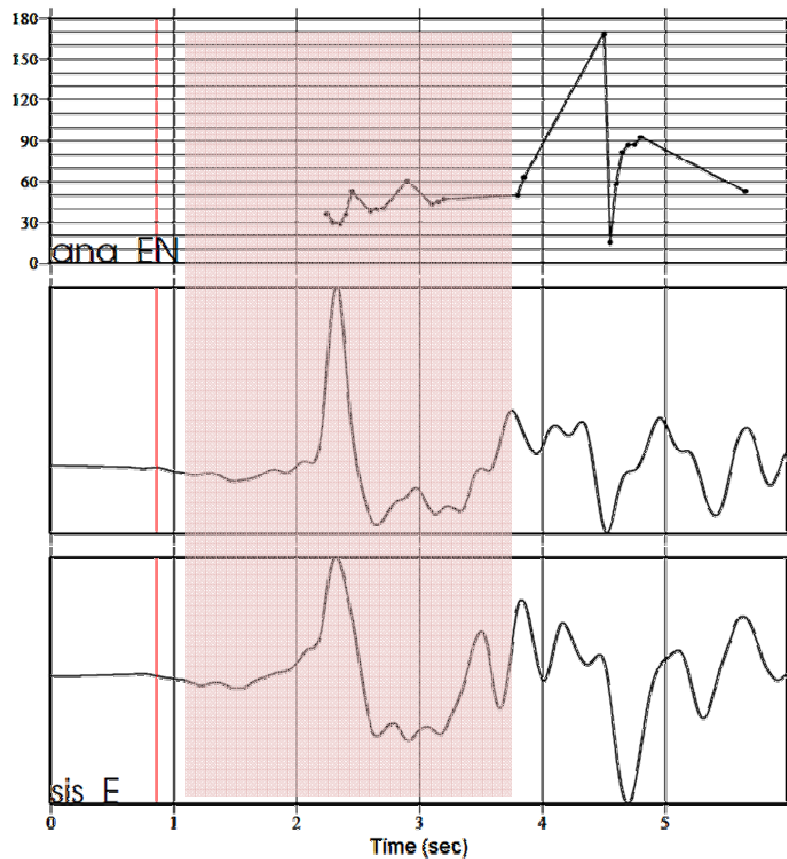


Figure 4.6: Example of stability of polarization. sisN and sisE are the horizontal components, while anaEN represents the angle of polarization as function of time. The pink area indicates the time window in which the polarization is stable.

Chapter 5 Source parameters from RSTFs

5.1 Introduction

As seen in the previous chapter, from the RSTFs it is possible to obtain the knowledge of the seismic source without modeling the propagation between the source and the receiver. The observables of RSTFs are:

- Duration
- Area
- Shape

These give us accurate estimations of source radius, and so corner frequency, seismic moment and rupture velocity. Moreover, the inversion of RSTFs allowed to constrain the fault plane and provided us with the estimation of the slip distribution, the rupture direction and the average velocity rupture. From estimates of source radius and seismic moment the static stress drop can be calculated with equation (1.24) and the scaling laws can be investigated.

Therefore, in this chapter the properties of RSTFs are illustrated and the relation between the duration and corner frequency are reported.

5.2 Effects of directivity: rupture duration and seismic moment

The first-order effect we expect to see on a deconvolved source time function at a particular station is directivity.

The source time function can be defined as the shape of the body-wave pulses which are caused by the earthquake rupture. At distances beyond a few fault lengths, the near-field effects are dominated by far-field effects, and so only these far-field terms are considered in this case.

For a small earthquake, the fault is considered to be a single point source. As a simple approximation, displacement on this fault can be considered to occur as a ramp function. The source time function arising from a ramp time history on a single point source is a box-car of length τ_r , which is the rise time of the ramp function. For finite

length faults, the rupture plane can be approximated as the summation of a number of earthquake point sources that rupture with the appropriate time delays considering the progressive rupture of the fault (Fig. 5.1). This simple line source is the Haskell Fault Model.

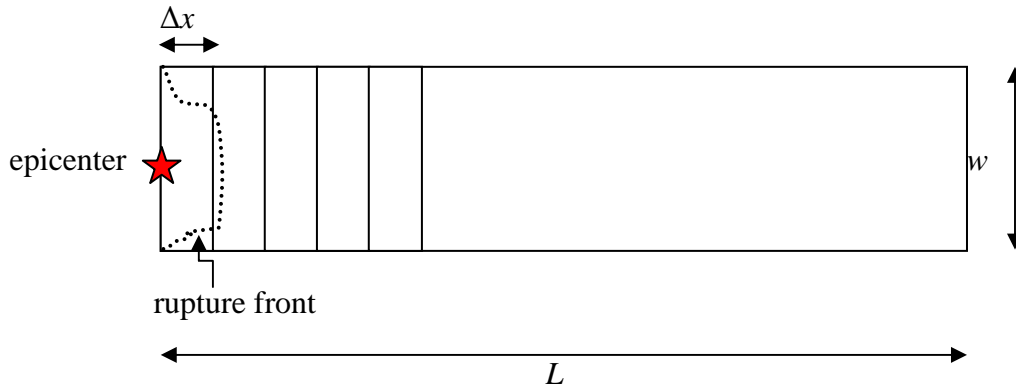


Figure 5.1: Simplified fault geometry for fault of width w and length L , with unilateral slip. Rupture plane is divided into sub-event slices of length Δx .

Figure 5.2 shows a fault of length L , rupturing from left to right. If the distance to the recording station is r ($r \gg L$), then the arrival time of a ray from the beginning of the faults is $t=r/c$, where c is the velocity of the wave type. The arrival time of waves from a faulting segment at point x on the fault is given by:

$$t_x = \frac{x}{v_r} + \frac{r - x \cos \theta}{c} \quad (5.1)$$

Thus the difference in time between energy arriving from the end of the fault, at position L and that arriving from the beginning of the fault can be used to define the time τ_c , the duration of rupture for this unilateral case, as observed at the station at (r, θ) :

$$\tau_c = \left[\frac{L}{v_r} + \frac{r - L \cos \theta}{c} \right] - \frac{r}{c} = \frac{L}{v_r} - \frac{L \cos \theta}{c} \quad (5.2)$$

Then the rupture time depends on the viewing azimuth. This azimuth dependence due to fault propagation is called *directivity*. If a station is located along the direction of rupture propagation, $\theta = 0^\circ$ and τ_c is short, especially in the case of the shear wave speed ($c = \beta$), as v_r is typically $\approx 0.8\beta$. A station behind the rupture propagation ($\theta = 180^\circ$) has a long τ_c and small amplitude. Stations located perpendicular to the rupture ($\theta = 90^\circ$) are not affected by the directivity.

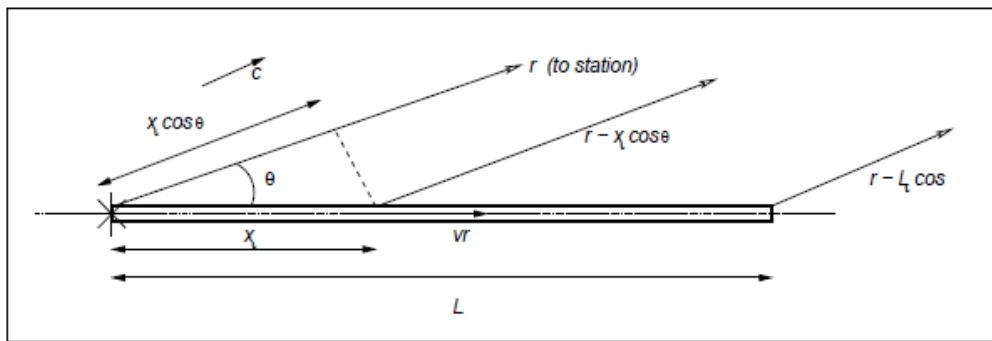


Figure 5.2: (from Clinton, 2004) Azimuthal dependency of arrival times, for fault plane rupturing from left to right.

A scheme showing how source time functions are affected by a unilaterally rupturing strike-slip fault is in figure 5.3.

The area under the time function is directly proportional to the seismic moment, which must be independent of azimuth. In fact, the area of the RSTFs is equal to the moment ratio between the mainshock and EGF and it must remain the same at all stations.

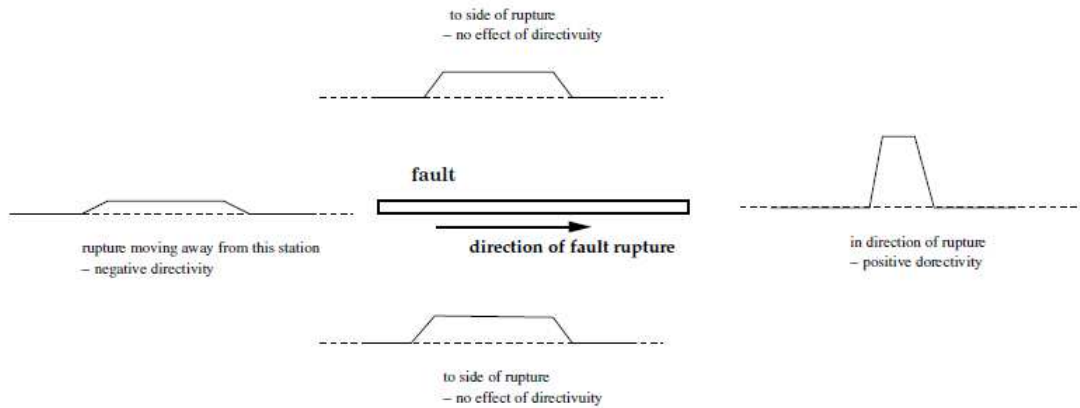


Figure 5.3: (from Clinton, 2004) Simplified azimuthal variations for source time functions in a unilaterally strike-slip fault rupture. Note that the area under the source time function (proportional to the seismic moment, M_0) is constant, but the time, and the amplitudes, vary widely.

The simple Haskell line source representation that we have considered involves *unilateral rupture*, or rupture in only one direction. For some earthquakes, unilateral rupture is a sufficient model of the faulting process, but many earthquakes nucleate in the center of a fault segment and spread in both directions. This known as *bilateral rupture*. The source time function for bilateral rupture varies much less with azimuth, and it is often impossible to distinguish bilateral rupture from a point source. Some faults appear to expand radially, as *circular rupture*. This model was introduced by several authors including Savage (1966), Brune (1970), and Keilis-Borok (1959) to quantify a simple source model that was mechanically acceptable and to relate slip on a fault to stress changes. Dislocation models such as Haskell's model produce nonintegrable stress changes due to the violation of material continuity at the edges of the fault. A natural approach to model earthquakes is to assume that the earthquake fault is circular from the beginning, with rupture starting from a point and then propagating self-similarly, until it finally stops at a certain source radius.

5.3 Corner frequency and rupture velocity

For a circular rupture the duration of rupture τ_c is given by:

$$\tau_c = \frac{r}{v_r} \cdot \left[1 + \frac{v_r \sin \theta}{c} \right] \quad (5.3)$$

where θ is the angle between the normal \vec{n} to the fracture plane and the direction of the ray (Fig. 5.4). By integrating (5.3) on the fault plane we get:

$$\begin{aligned} \Delta \tau_c &= \frac{2}{\pi} \int_0^{\pi/2} \frac{r}{v_r} \cdot \left[1 + \frac{v_r \sin \theta}{c} \right] d\theta = \\ &= \frac{r}{v_r} + \frac{2}{\pi} \cdot \frac{v_r}{c} = \frac{r}{v_r} \cdot \left[1 + \frac{2v_r}{\pi c} \right] \end{aligned} \quad (5.4)$$

As seen in the chapter 1, the source radius is related to corner frequency f_c through the relation (1.23), that is:

$$r = k_c \cdot \frac{c}{f_c} \quad (5.5)$$

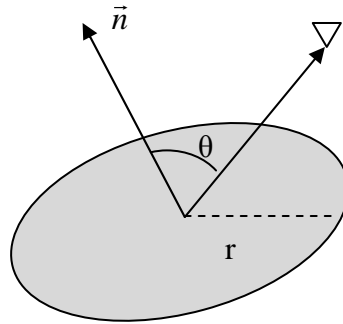


Figure 5.4: Circular fault plane with finite radius r . θ is the angle between the normal to the fault plane and direction of ray.

As mentioned above, k_c is a coefficient which depends on the adopted circular rupture model and wave type. By replacing (5.5) in (5.4) we obtain the relationship between the corner frequency and rupture duration:

$$f_c = k_c \frac{c}{v_r} \cdot \left[1 + \frac{2v_r}{\pi c} \right] \cdot \frac{1}{\Delta\tau_c} \quad (5.6)$$

Let us consider three circular source model:

➤ Sato and Hirasawa's model (1973), where the center of the expanding circular front coincides with the center of the circular fault. In Sato and Hirasawa's (1973) model, the stopping of slip occurs simultaneously over the entire surface of the crack when the rupture front stumbles on the edge of the fault. This model predicts higher corner frequency for P-waves than for S-waves, in accordance with observations. Their corner frequencies averaged over all directions are:

$$f_c^P = k_P^{SH} \cdot \frac{\alpha}{r} \quad ; \quad f_c^S = k_S^{SH} \cdot \frac{\beta}{r} \quad (5.7)$$

where α and β are P- and S- waves velocity, respectively. k_P^{SH} and k_S^{SH} are the coefficients for P- and S- waves equal to $1.85/2\pi$ and $1.53/2\pi$.

➤ Madariaga (1976). In this model, the slip does not stop simultaneously on the fault. Once the rupture front stops, a healing phase propagates inward from the edge of the fault causing the arrest of slippage. For Madariaga's model:

$$f_c^P = k_P^{MAD} \cdot \frac{\beta}{r} \quad ; \quad f_c^S = k_S^{MAD} \cdot \frac{\beta}{r} \quad (5.8)$$

where $k_P^{MAD} = 0.32$ and $k_S^{MAD} = 0.21$. In this equation the velocity of S-waves is considered also for P-waves.

➤ In Brune's model (1970) the stress pulse is applied instantaneously on the whole fault area. For this reason, there is no fracture propagation. The shear pulse generates a shear wave that propagates perpendicularly to the fault plane. Brune's model is commonly used to obtain fault dimensions from spectra of S waves, so the corner frequency is given by:

$$f_c^S = k_S^{BRU} \cdot \frac{\beta}{r} \quad (5.9)$$

where $k_S^{BRU} = 0.37$.

In this models, all the coefficients k_S were obtained by assuming the ratio between rupture velocity and S-waves velocity v_r/β equal to 0.9.

By rewriting equation (5.4) for P- and S- waves we obtain the following relations:

$$\frac{1}{r} = \frac{1}{v_r} \cdot \left[1 + \frac{2v_r}{\pi\beta} \right] \cdot \frac{1}{\Delta\tau_S} \quad \frac{1}{r} = \frac{1}{v_r} \cdot \left[1 + \frac{2v_r}{\pi\alpha} \right] \cdot \frac{1}{\Delta\tau_P} \quad (5.10)$$

The formula (5.10) can be used to obtain the estimate of rupture velocity v_r , comparing the ratio $\Delta\tau_S/\Delta\tau_P$:

$$\frac{\Delta\tau_S}{\Delta\tau_P} = \frac{1 + \frac{2v_r}{\pi\sqrt{3}\beta}}{1 + \frac{2v_r}{\pi\beta}} \quad (5.11)$$

by assuming $\alpha = \sqrt{3}\beta$.

So from source time functions calculated by P- and S-phases the rupture durations are obtained and by applying relation (5.11) the rupture velocity can be estimated.

Chapter 6 Applications

In this chapter we will see the results obtained by applying the deconvolution technique (Vallée, 2004) to the $M_w=6.3$ L'Aquila mainshock and cluster of aftershock and foreshock of L'Aquila sequence with moment magnitude ranging between 3.5 and 5.6. Finally the results obtained to $M_w=2.9$ Laviano mainshock are shown.

6.1 L'Aquila sequence

The 2009 L'Aquila earthquake (M_w 6.3) occurred in the Central Apennines (Italy) on April 6th at 01:32 UTC. The hypocenter is located at 42.35 N, 13.38 E at a depth of 9.5 km (<http://portale.ingv.it>). The earthquake caused nearly 300 casualties and heavy damages in the L'Aquila town and in several villages nearby. The mainshock was preceded by a seismic sequence starting a few months before and culminating with an M_L 4.1 event on March 30th 2009, followed by a M_L 3.9 and a M_L 3.5 foreshocks on April 5th 2009 – a few hours before the mainshock. The earthquake ruptured a northwest - southeast active segment of the normal fault system embedded in the mountain front of the central Apennines (Cirella et al., 2009; Walters et al., 2009).

The central Apennines (Italy), that belongs to the Lazio-Abruzzi Mesozoic carbonate platform domain, is dominated by the roll-back of the Adriatic subduction toward the east (Doglioni et al., 1998). This region shows an arc-like belt of seismicity in the upper crust that follows the mountain range and is characterized by normal faults directed along pre-existing compressive tectonic structures (Bigi et al., 2002). North-West striking segments are present and the largest seismic events are mainly related to normal faulting mechanisms (Fig. 6.1), consistent with the regional NE–SW trending extension (Selvaggi, 1998; Montone et al., 1999; Serpelloni et al., 2005; Devoti et al., 2008; D'Agostino et al., 2009) and likely controlled by deep crustal-scale decollements (Bigi et al., 2002).

One of goals of this work was the creation of an accelerometric waveform archive of 605 earthquakes recorded between 30 March 2009 and 30 April 2009 by DPC-RAN (National Accelerometric Network) (35 stations) and by INGV (29 stations) permanent and temporary seismic networks. All of the stations are equipped with Kinematics

Episensor FBA ES-T sensors with high dynamic range, from 108 to 130 dB. Several of the new stations installed after the L'Aquila mainshock, are equipped with the new instrumentation recently acquired by DPC: a three-component Syscom Instruments Force Balance Accelerometer, model MS2007.

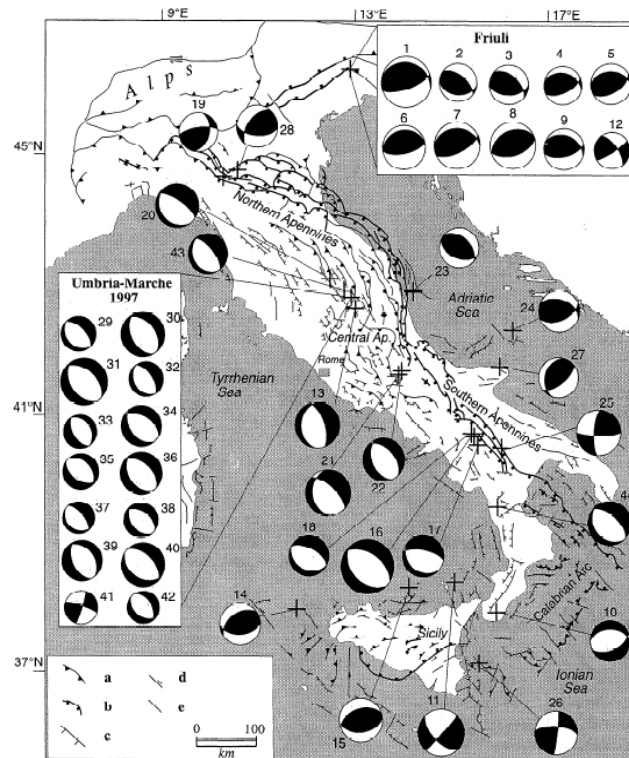


Figure 6.1: Sketch map of main tectonic features of Italy simplified from Bigi et al. (1990). CMTs for great earthquakes that occurred between 1976 and 1998 are shown. (a) thrust fault (pre-middle Pliocene); (b) thrust fault (middle Pliocene-Recent); (c) normal fault; (d) strike-slip fault; (e) undetermined fault (Montone et al., 1999).

The total number of three-component records is 32275 for events with local magnitude ranging between 2.5 and 5.9, and recorded by 3 to 41 stations. This dataset provides with a unique aftershock strong motion data bank covering a wide moment magnitude [2.6-6.3] and epicentral distance ranging from near-source (≤ 20 km) to far-field (100 km) (Fig. 6.2). For this reason these data can be very useful to determine refined ground motion prediction equations and models of the rupture processes.

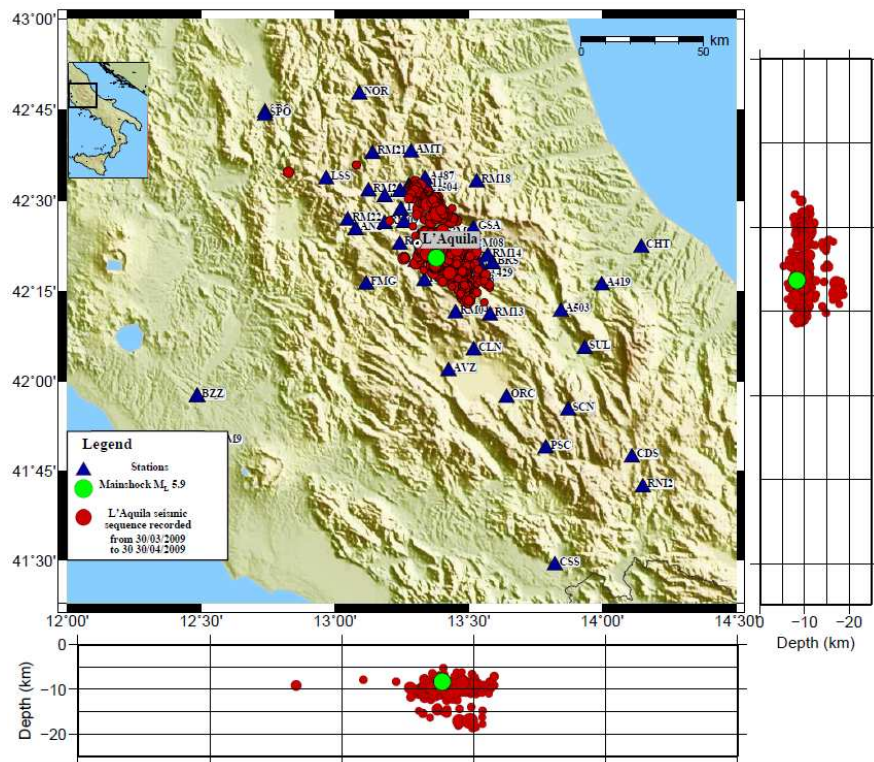


Figure 6.2: Map showing the stations of DPC-RAN and INGV networks (triangles). The hypocenters of the earthquakes considered in this study (size of circle is proportional to the local magnitude) are also plotted.

The creation of the database consists of three phases:

1. processing of binary files in ASCII files
2. converting ASCII files into SAC files format (Seismic Analysis Code, from Lawrence Livermore National Laboratory)
3. association of the waveform (in sac format) at each event.

In the last step the header of each event waveform is filled of location and local magnitude reported by catalog *Italian Seismic Instrumental and parametric Data-basE* (Iside, <http://iside.rm.ingv.it>).

A data quality parameter (Elia et al., 2009) is assigned to each waveform, automatically computed by evaluating the signal to noise ratio S/N of the signal level S of the recorded earthquake compared to the noise level N before the event. In figure 6.3 and 6.4 an example of waveforms with $S/N \geq 50$ and waveforms of a small earthquake are shown, respectively.

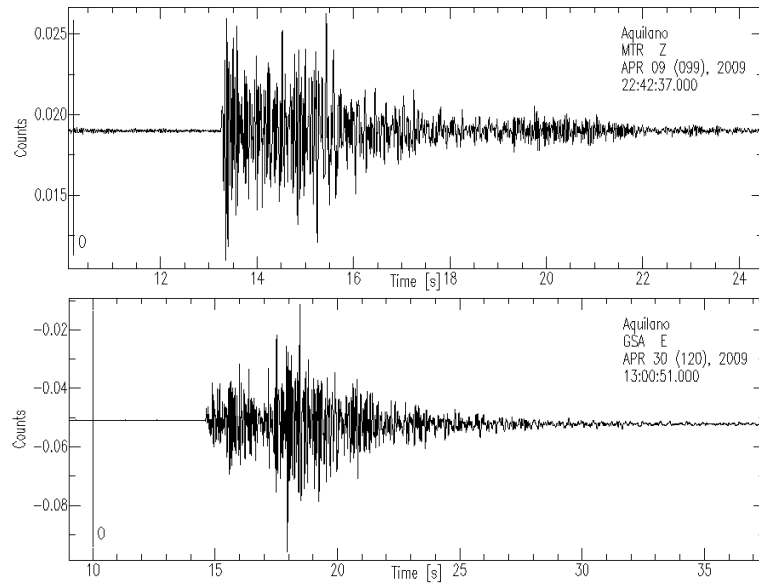


Figure 6.3: Examples of waveforms recording by RAN network. The seismogram relative to station MTR presents $S/N \approx 51$, while for station GSA it is equal to about 85.

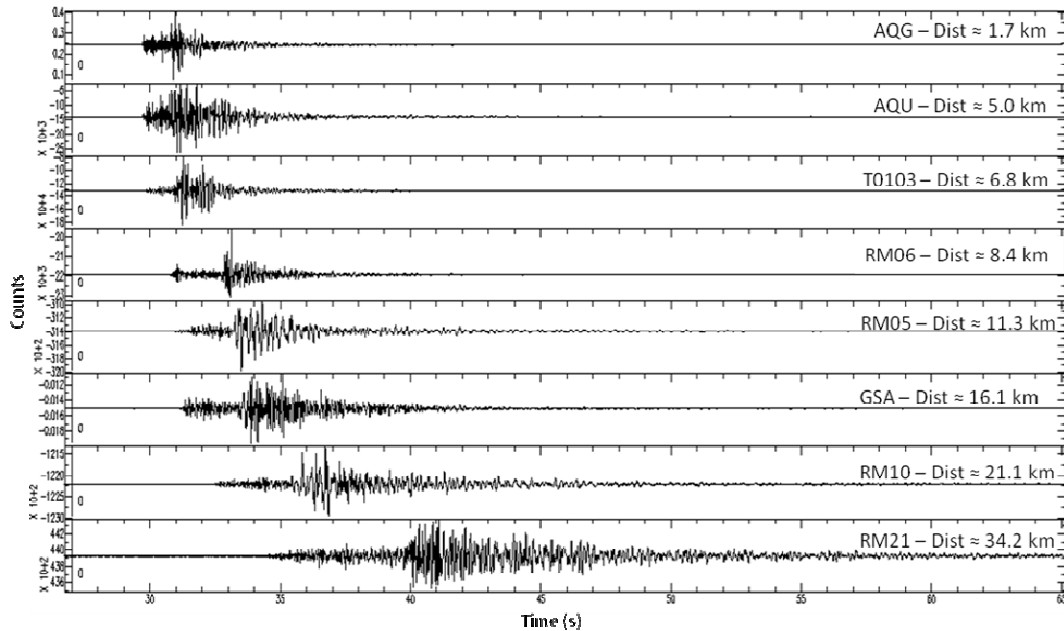


Figure 6.4: Waveforms of a small earthquake recorded up to a distance of about 30 km from epicenter. Date: 2009-04-30; Origin time $T_0 = 16:41:47$; Latitude ($^\circ$) = 42.35; Longitude ($^\circ$) = 13.342; Depth (km) = 8.6; Local magnitude $M_L = 2.5$.

6.1.1 M_w 6.3 L'Aquila mainshock

In this paragraph the RSTFs of $M_w=6.3$ L'Aquila mainshock are shown. As we will see, from RSTFs the fracture properties are analyzed.

Regional data

To determine the RSTFs the $M_w=4.9$ aftershock occurred on 2009-04-09 at 09:26:29 UTC was used as EGF. To get more information at different azimuths and to overcome the limitations of similar location and focal mechanism between master event and EGF, the waveforms of 39 broad band stations have been recovered by the following networks: MedNet (MN), ISNet (IN), INGV (IV), GEOFON (GE), French Broadband Seismological Network (FR), Austrian Seismic Network (OE), Aristotle University of Thessaloniki Seismological AUTH (HT), Slovenia (SL), BayernNetz, Germany (BW), Hungarian Seismological Network (HU).

These stations are located at a distance greater than about 200 km and less than about 80 km (Fig. 6.5).

In case of a large earthquake, the waves considered in the deconvolution process are surface waves. They constitute the best choice, since they are sensitive to long periods and they do not suffer from the wave mixing of body waves. Data has been windowed in the Love and Rayleigh waves and filtered between 0.05 Hz and 1 Hz (Fig. 6.6).



Figure 6.5: Map of seismic stations used in this study. The location of $M_w=6.3$ mainshock (red star) and EGF (white circle) are also shown. The information on location and focal mechanism are taken by catalogue Iside and INGV, respectively.

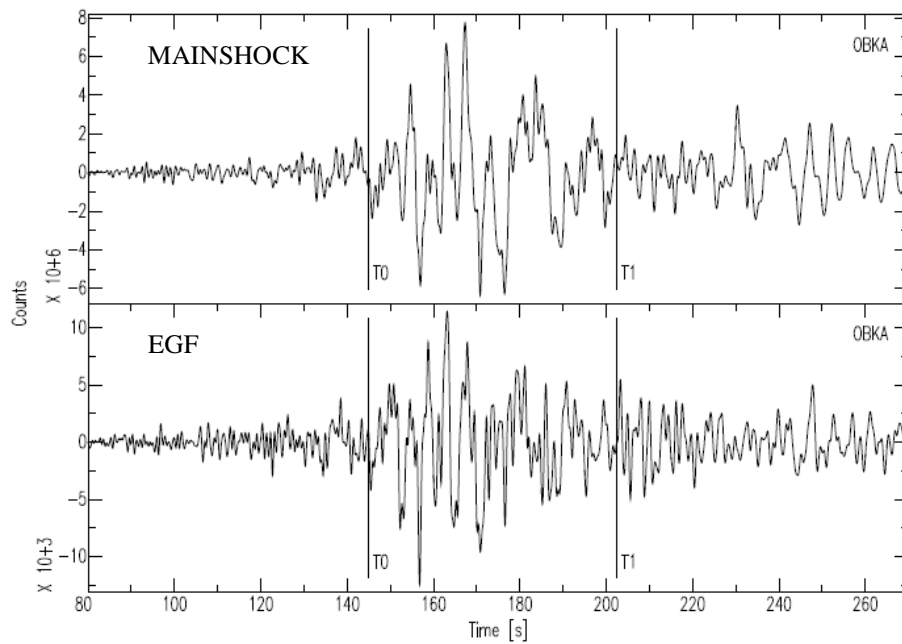


Figure 6.6: Example of time window $[T_0, T_1]$ on Love wave for the station OBKA.

Estimate of fracture properties: modeling of RSTFs

Figure 6.7 shows the RSTFs obtained for all the considered stations with increasing azimuth from left top to right bottom.

It is clear the presence of two bumps in the RSTFs as well as the effects of directivity. In fact, the RSTFs of station located along the direction of rupture propagation, i.e. stations of ISNet network (AND3, CLT3, etc.) show short duration and big amplitude, while the RSTFs of station behind the rupture propagation, i.e. stations of Austrian seismic network (DAVA, RETA), have long duration and small amplitude.

In other words, proceeding from stations behind the rupture propagation (station ROBS) to stations along the direction of rupture propagation (station COL3) we observe in RSTFs that the distance between the two bumps becomes increasingly smaller and their amplitude increasingly small.

The two bumps may mark off an anomaly zone due to the presence of eventual fluid. To confirm this hypothesis, a careful study of the geology of the area should be done.

Since the two bump are well localized, we considered the difference $\Delta\tau$ between the arrival times of first and second bumps to obtain accurate estimates of rupture velocity V_r and length L of fault plane. In this case the estimated length is the segment of faults between the two bumps. For the event in study we assumed the following unilaterally propagating rupture model

$$\Delta\tau = \frac{L}{V_r} \left(1 - \frac{V_r}{c} \cos \alpha \right) \quad (6.1)$$

where c is the velocity of wave used in the deconvolution process and α is the directivity angle between the rupture direction and the Love-wave ray leaving the source. For this analysis we used only the RSTFs calculated by Love waves. So, the Love - waves phase velocity is set equal to 4.5 km/s. From fit between the observed data $\Delta\tau$ and theoretical model (6.1) we obtain that $V_r = 1.85 \pm 0.09$ km/s and $L = 5.6 \pm 0.3$ km (Fig. 6.8). This value of V_r corresponds to about 60-70% of the velocity of shear waves to the depth of the source and it is consistent with a slow rupture propagation as well as inferred

from kinematic inversion models obtained by the combined inversion of teleseismic, accelerometer and GPS data (Balestra et al., 2010, Yano et al., 2009). In fact figure 6.9a shows the observed RSTFs (filled curves) together with the RSTFs computed (red curve) from slip model of Balestra et al. (2010) inverting strong motion, broadband teleseismic, GPS, and InSAR data (Fig. 6.9b). We can observe from this model that the rupture propagates in two directions, updip and toward the SE, exhibiting two or three asperities. Balestra et al. (2010) estimate a value of rupture velocity equal about 1.9 km/s and the total rupture length is between 14 and 16 km. So, the estimate $L=5.6$ km obtained in our study represents the distance between the two patch of highest values of slip in the slip model. The good agreement between observed and computed RSTFs is a strong indicator of the realness of our results.

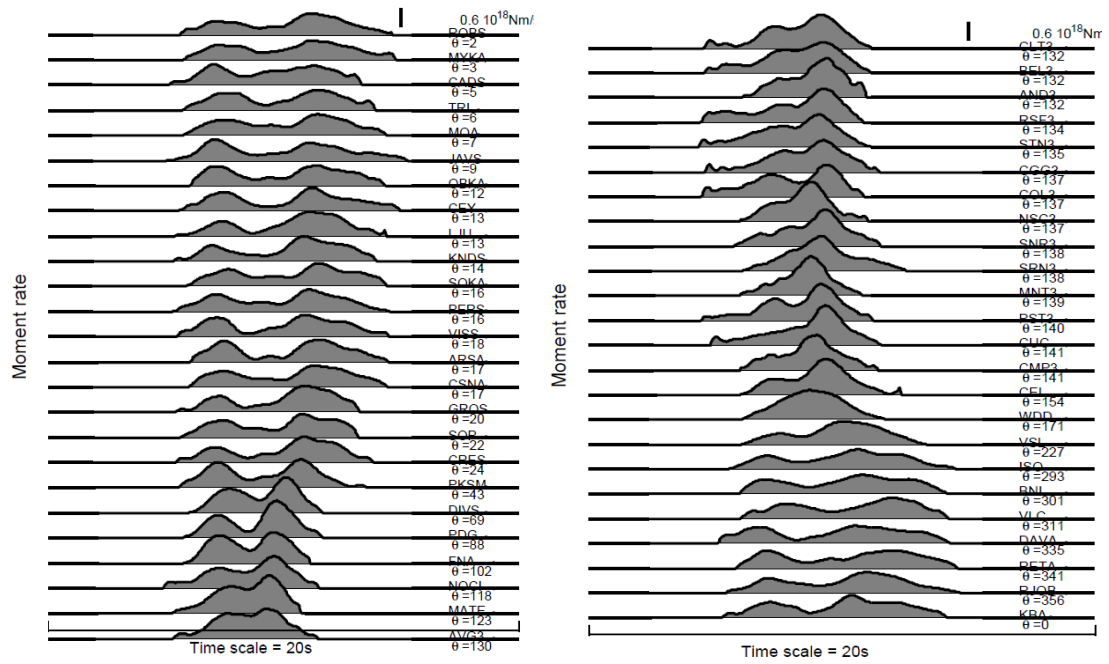


Figure 6.7: RSTFs obtained by stabilized deconvolution of Mw=6.3 L'Aquila mainshock.

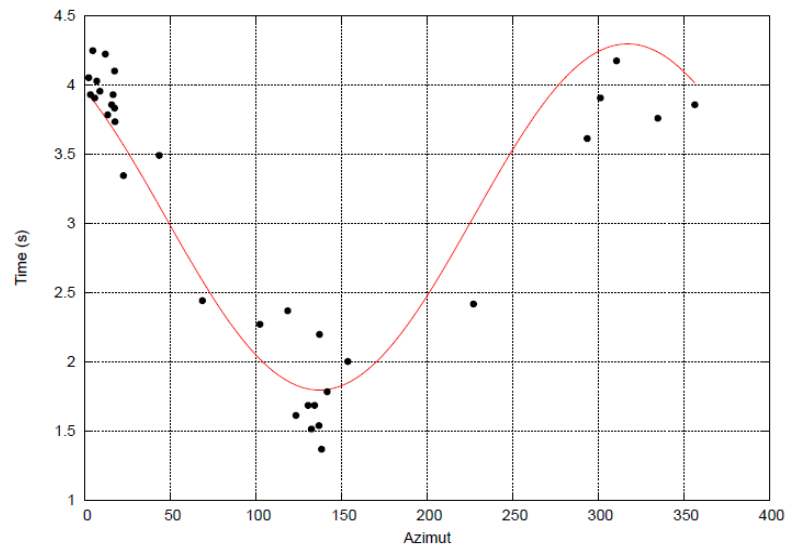


Figure 6.8: Fit between the observed data (black circles) and theoretical model (red curve). The observed data are the difference between the arrival times of first and second bumps.

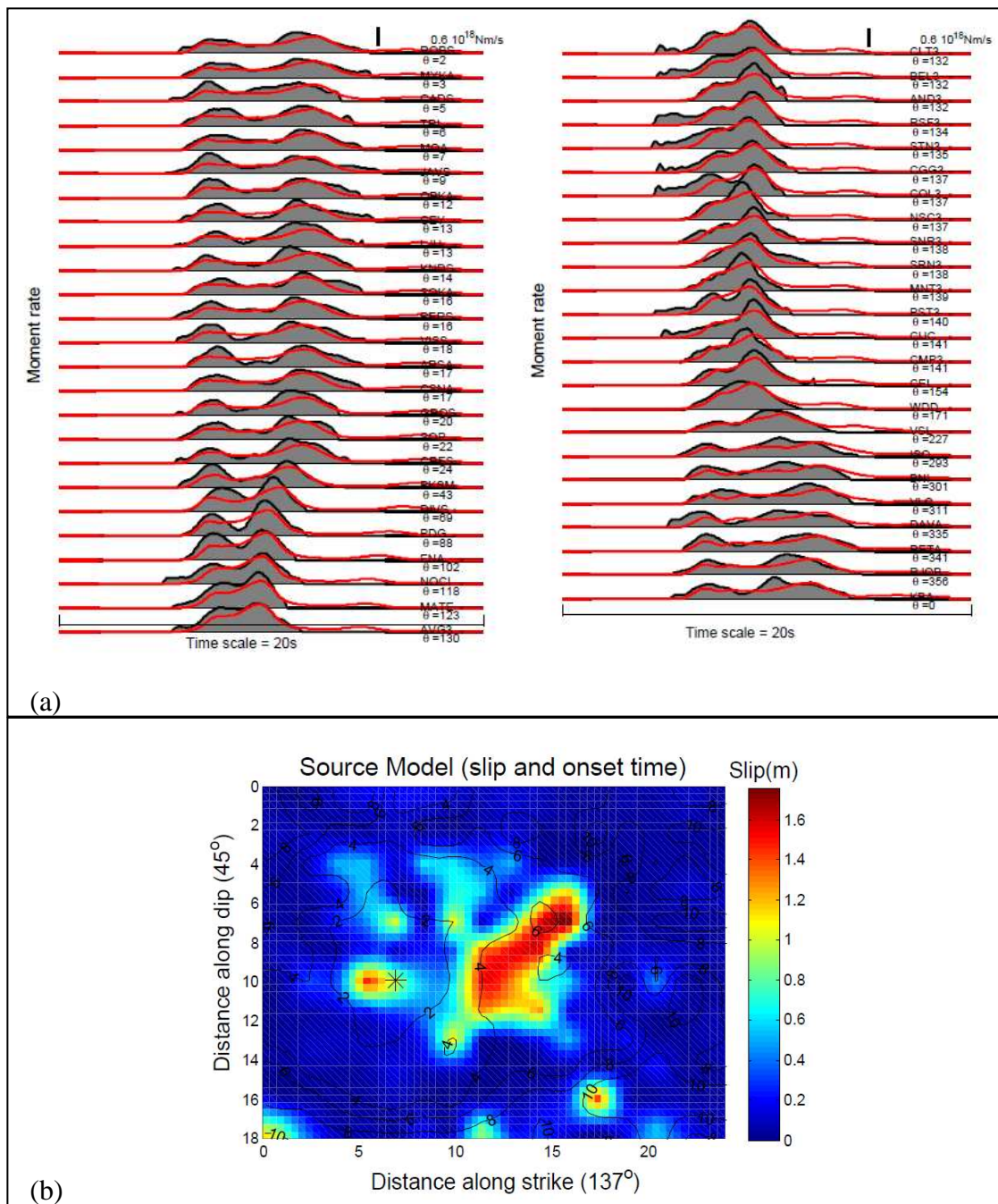


Figure 6.9: Comparison between observed and computed RSTFs (a). Observed RSTFs (filled curves) are obtained by deconvolution approach. Computed RSTFs (red curves) are computed from rupture process model (b) of Balestra et al. (2010).

6.1.2 Cluster of events with $M_w \geq 3.0$

After the study of fracture properties of $M_w=6.3$ L'Aquila mainshock, the events of L'Aquila sequence with moment magnitude $3 < M_w < 5.6$ are analyzed to retrieve information on kinematic parameters of fractures, in particular, on rupture velocity and its relationships with corner frequency.

Near source data

From the data set described in paragraph 1 a cluster of 32 events with $M_w \geq 3$ has been selected. The accelerometric waveforms of this events have been integrated with velocimeter data recorded by INGV network.

As seen in paragraph 4.4.2, the near-source data processing requires several steps before the deconvolution. In the first and second steps the 32 events are located using the code NLLoc (Lomax et al, 2000) and the focal mechanisms are calculated with FPFIT (Reasenberg et al, 1985). The focal mechanisms are prevalently of normal type, consistent with the extensional tectonics active in the central Apennines since the Pliocene (Walters et al., 2009) (Fig. 6.10).

From this cluster of events, 15 pairs master event-EGF with similar location and focal mechanism have been selected. Finally the study of the stability of the polarization is performed to the optimal choice of the frequency range to be used in the deconvolution process.

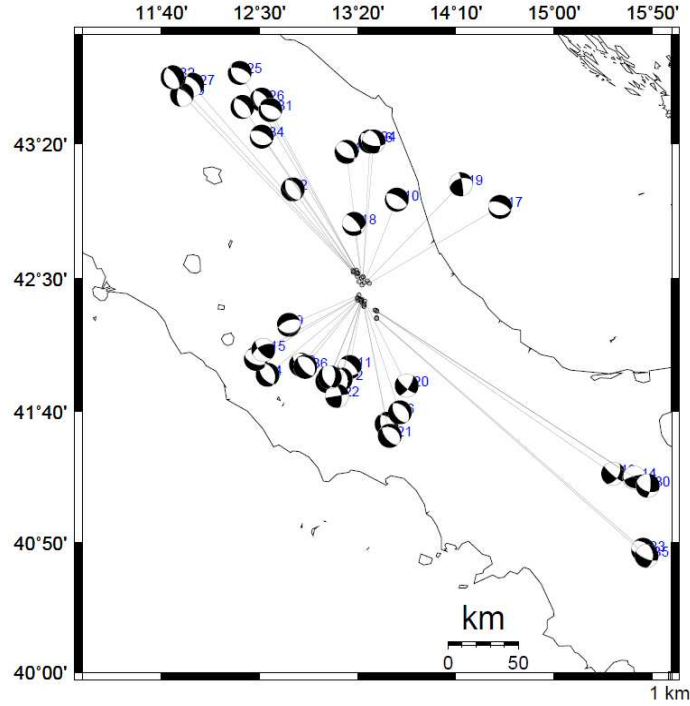


Figure 6.10: Hypocenter (dots) and focal mechanisms of cluster of 32 events with moment magnitude ranging between 3 and 5.6.

Rupture duration, corner frequency and rupture velocity

For each selected pair master event-EGF, the RSTFs are calculated for P- and S- phase using the deconvolution method (Vallée, 2004). Figure 6.11 shows the RSTFs of $M_w=4.0$ foreshock occurred in 2009-03-30 at 13:38 (UTC). Also the misfit between the real mainshock and the reconstituted mainshock for any stations is shown as a function of the allowed duration of the RSTF. As EGF the $M_w=3.0$ 11 April 2009 at 13:57 UTC was used. The range of frequency used in the deconvolution process is [0.05-4] Hz.

Once the RSTFs are known, the relationship between the corner frequencies f_c estimated through the inversion of the displacement spectra of S-waves (Orefice and Zollo, 2010) and the inverse of duration τ_c^{-1} has been investigated. For each master event the mean value of inverse duration $\Delta\tau_c^{-1}$ is calculated as arithmetic mean of τ_c^{-1} observed at each station.

In figure 6.12 the estimate of f_c with their uncertainties are plotted as function of $\Delta\tau_P^{-1}$ and $\Delta\tau_S^{-1}$, that is the arithmetic mean of τ_c^{-1} obtained by P- and S- phases, respectively. In order to estimate the best value for the f_c -to- $\Delta\tau_P^{-1} / \Delta\tau_S^{-1}$ ratio, a non-linear best-fitting

procedure which allows to account for the uncertainties on both the two variables has been applied (Reed 1989), assuming the linear model $\text{Log}(f_c) = \text{Log}(\Delta\tau_c^{-1}) + \text{Log}(a)$. The fitting problem is reduced to an optimization problem for the intercept $\text{Log}(a)$ by setting the slope to one. The estimated value for S-phase is $\text{Log}a_s \pm \sigma a_s = -3.32\text{e-}02 \pm 2.30\text{e-}02$ which yields $a_s \pm \sigma a_s = 0.93 \pm 0.05$. For P-phase we obtain $\text{Log}a_p \pm \sigma a_p = -7.41\text{e-}02 \pm 3.89\text{e-}02$ which yields $a_p \pm \sigma a_p = 0.84 \pm 0.08$. Therefore, the observed duration of RSTFs is in inverse proportion to corner frequency.

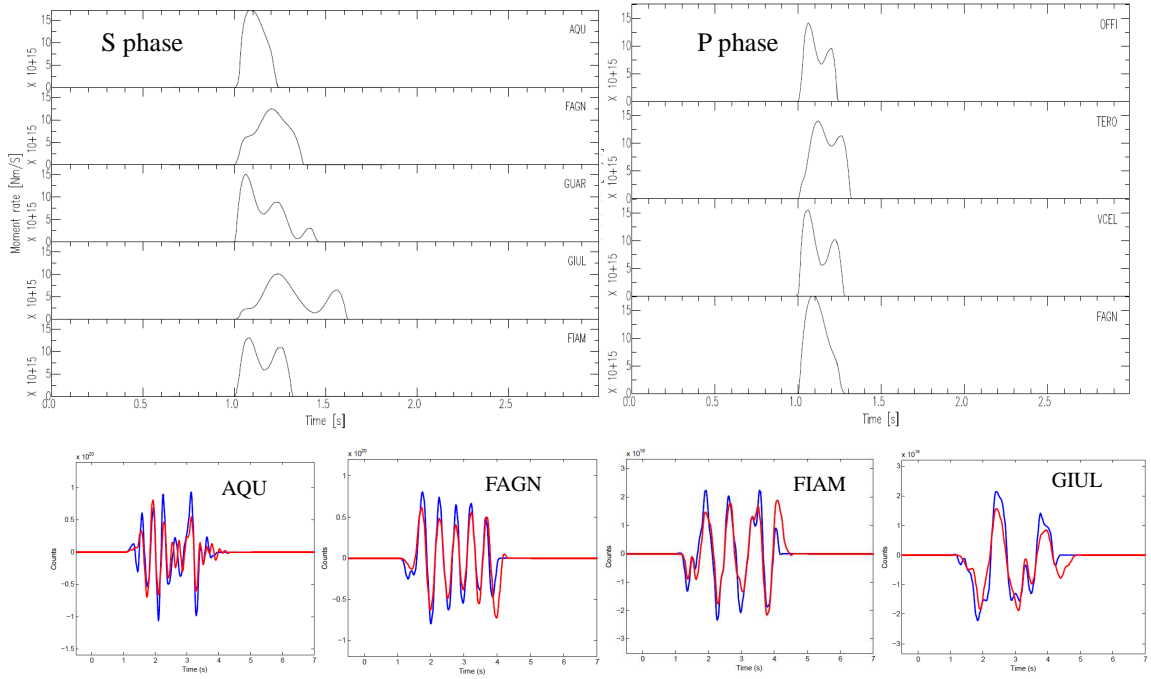


Figure 6.11: RSTFs of an event with moment magnitude $M_w=4$ obtained by S- and P- phase. Any example of misfit between real mainshock and the reconstituted mainshock are reported.

As seen in the paragraph 5.3, the theoretical coefficient a is given by the quantity

$$\Delta\tau_c \cdot f_c = a = k_c \frac{c}{v_r} \cdot \left[1 + \frac{2v_r}{\pi c} \right] \quad (6.2)$$

where $k_c \cdot c$ depends on the adopted circular rupture model and wave type.

In this study we considered three circular models, that is Madariaga's (1976), Brune's

(1970) and Sato & Hirasawa's (1973) model. In Table 4 the theoretical coefficients a for this models are reported for both P- and S- waves. We want remark that in these models, all the coefficients k_c and so the coefficients a are obtained by assuming the ratio between rupture velocity and S-waves velocity v_r/β equal to 0.9.

In figure 6.12 the theoretical lines obtained by using Madariaga's (red line), Brune's (green) and Sato and Hirasawa's (blue) model are also plotted. We can observe that none of the models in literature (circle rupture) explains the relationship f_c vs $\Delta\tau_P^{-1}/\Delta\tau_S^{-1}$. This could be due to the fact that the v_r/β ratio is not equal to 0.9, as these models assume. In fact, using the measurements $\Delta\tau_P$ and $\Delta\tau_S$ we can estimate the rupture velocity through relation (5.11) independently from the adopted rupture model. To estimate v_r we applied the same non-linear best fitting procedure implemented for the estimation of coefficient a . The best fitting line $\text{Log}(\Delta\tau_P^{-1}) = \text{Log}(\Delta\tau_S^{-1}) + \text{Log}(b)$ results $b \pm \sigma b = 1.16 \pm 0.08$ (Fig. 6.13). Assuming different values of v_r/β in equation (5.11), with $\beta = 3374$ m/s (Bagh et al, 2007), we obtain that $b \pm \sigma b = 1.16 \pm 0.08$ corresponds to ratio v_r/β ranging between 0.7 and 0.8. Therefore, the most probable value of v_r/β ratio is less than 0.9.

So, as obtained for the Mw = 6.3 L'Aquila mainshock, also the smallest events have low value of rupture velocity, indicating that v_r is a mechanical property of rocks where fractures are developed, regardless of the geometry of the fracture planes and the initial conditions of stress .

Table 4: Theoretical coefficient a for the circular model used in this study

Model	a^{theo} S wave	a^{theo} P wave
Madariaga (1976)	0.367	0.437
Brune (1970)	0.647	-
Sato and Hirasawa (1973)	0.627	0.515

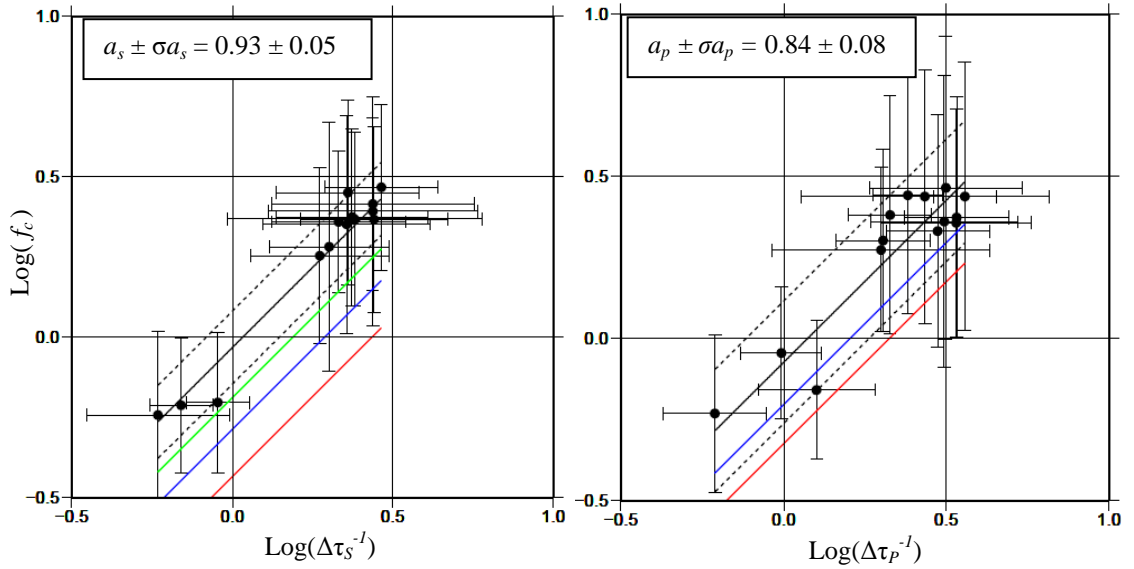


Figure 6.12: Corner frequency versus inverse of duration obtained by S- (on the left) and P- phases (on the right). The black lines are the best fitting lines, while the dashed lines correspond to plus/minus one standard deviation. The theoretical lines obtained by Madariaga's (red line), Brune's (green) and Sato and Hirasawa's (blue) model are also plotted.

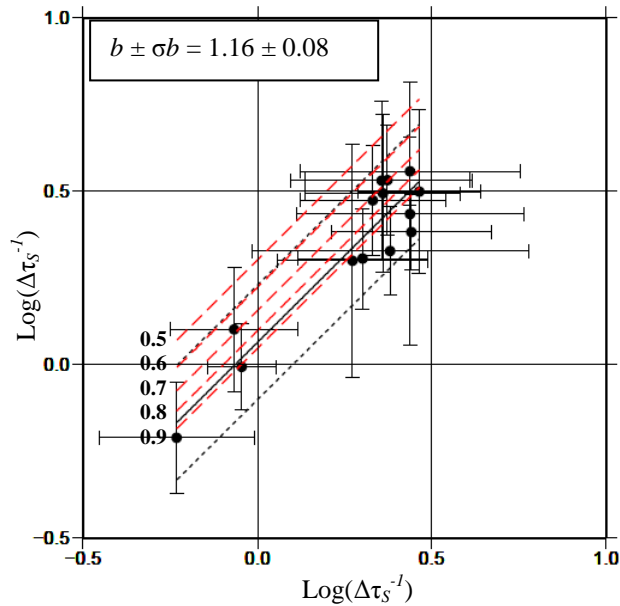


Figure 6.13: Inverse of duration obtained by S- phases versus inverse of duration obtained P- phases. The black lines are the best fitting lines, while the dashed lines correspond to plus/minus one standard deviation. The red lines are the theoretical lines obtained by assuming different values of ν_p/β in equation (3.30).

Scaling laws

As seen in the previous paragraphs, from the area and durations of RSTFs the seismic moment and source radius of events in study can be calculated, respectively. From estimates of source radius and seismic moment the static stress drop can be calculated with equation (1.24) and the scaling laws can be investigated.

As evidenced by previous analysis, the v_r/β ratio varies between 0.7 and 0.8. Exactly the value 1.16 of coefficient b corresponds to $v_r/\beta = 0.77$. So, by using this value the source radius is calculated by relation (5.10) for each events.

Figure 6.14a,b shows the log-log representation of source radius and static stress drop vs seismic moment, respectively, for P- wave (empty circles) and S- waves (solid circles), with the associated uncertainties. The constant stress drop lines at values 0.1 to 100 MPa are shown in the same figure. We observe the self-similar scaling of source radius with seismic moment. The mean value of static stress drop for P- and S- waves is (2.7 ± 1.2) MPa and (3.0 ± 1.7) MPa, respectively.

Thus, reliable source parameters can be estimated through RSTF without need to know velocity and attenuation model, and no assumptions are done on the shape of adopted spectral model.

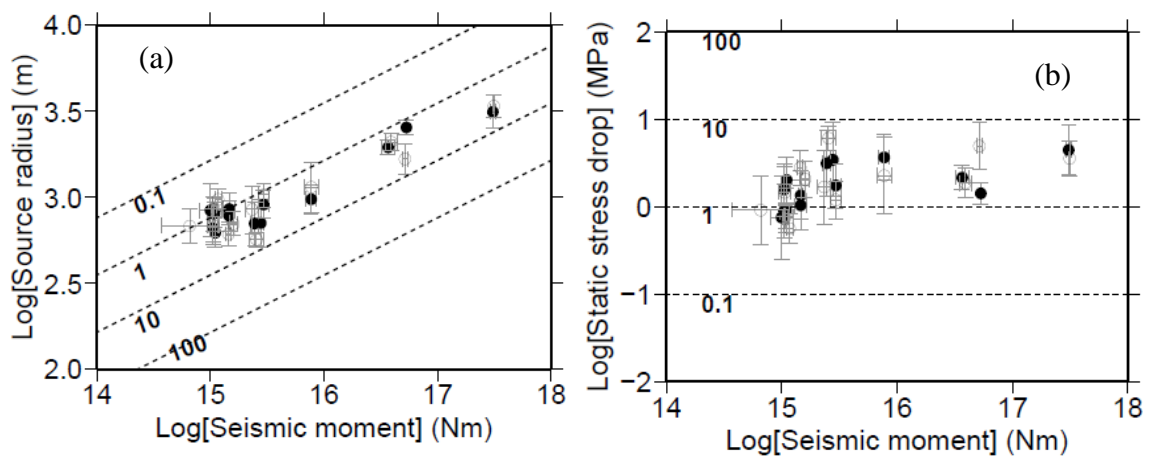


Figure 6.14: Log-log representation of source radius (a) and static stress drop (b) vs seismic moment, respectively, for P- wave (empty circles) and S- waves (solid circles), with the associated uncertainties. The constant stress drop lines at values 0.1 to 100 MPa are shown.

6.2 M_w 2.9 Laviano mainshock

We studied the rupture process of the largest magnitude event of Laviano sequence by performing a kinematic rupture modeling through the deconvolution by an empirical Green's function. The event of magnitude $M_w = 2.9$ is considered as the mainshock of the sequence since its seismic moment ($2.6 \cdot 10^{13}$ N·m), is about 4-5 times the cumulative seismic moment of all foreshocks and aftershocks ($6.5 \cdot 10^{12}$ N·m corresponding to $M_w = 2.5$). The main contribution to this latter value is due to the aftershocks which cumulated a seismic moment of $5.4 \cdot 10^{12}$ N·m ($M_w = 2.4$) while the one associated with the foreshocks was $1.1 \cdot 10^{12}$ N·m ($M_w = 2.0$).

Near source data

To retrieve the source time functions we applied the stabilized deconvolution technique of Vallée (2004) to $M_w=2.9$ Laviano mainshock recorded by ISNet network. In particular, the $M_w=1.9$ aftershock occurred on 2008-5-27 at 17:25 UTC was used as EGF. We estimated the RSTFs at 12 of recording stations (Fig. 6.15) in the S-wave time window: the duration ranges from about 0.07 s to about 0.11 s, evidencing a directivity effect.

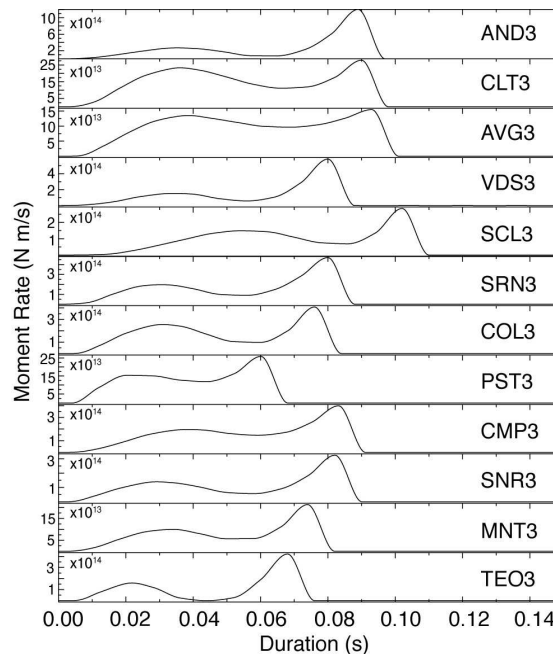


Figure 6.15: Apparent source time functions of the main event obtained at different stations of the ISNet network. Apparent source time functions are ordered from above to below respect to the station azimuth.

Inversion of RSTFs

We performed a kinematic rupture inversion of RSTFs by the use of isochrones back projection technique (Festa et al., 2006). The inversion of RSTFs allowed to constrain the fault plane and provided us with the estimation of the slip distribution, the rupture direction and the average velocity rupture.

For the main event we measured 26 P-wave first motion polarities. From these polarities we obtained by means of the FPFIT code the fault plane solutions of the main event. The two nodal planes have strike 290° , dip 40° , rake -100° , and strike 123° , dip 51° , rake -82° , respectively. The resulting focal mechanism is reported on figure 6.16a and indicates an almost pure normal faulting event. We investigated which of the two nodal planes is the more likely for the rupture of the main event by the use of the back-projection technique. For each plane and a fixed constant rupture velocity, we retrieved the best solution for the slip by minimization of the L^1 distance between the observed RSTFs and their synthetic estimations, the choice of the cost function trying to reproduce both the amplitude and the shape of the RSTFs. Results were plotted in figure 6.16b. The minimum of the cost function was obtained for a rupture with a velocity of 2.3 km/s along the nodal plane having strike 290° , and dip 40° . To check the sensitivity of the solution to the nodal plane and the rupture velocity, the vertical axis of the figure shows the normalized variation of the cost function with respect to the minimum value. By inspection of the curves, we found that the nodal plane generating the rupture is well constrained while the variation of the cost function with the rupture velocity is very small, indicating a large uncertainty on this parameter. The slip distribution (Fig. 6.16c) shows that the main event was principally a circular crack having a predominant updip direction of the rupture with an average velocity of 2.3 km/s, and a high slip patch of about 3.0 cm on the positive direction of the strike. The estimated average slip in this area is equal to 2.2 cm. In addition, we found that the other events mostly occurred on the left side (i.e. negative direction of the strike) of the main event, with average slips that range from 0.2 cm to 0.7 cm (Fig. 6.16c). These values are small compared to the average slip obtained for the main event.

The presence of structural or rheological discontinuities may be responsible of the strong heterogeneous slip distribution estimated for the main event and the asymmetrical

location of foreshocks and aftershocks. For this reason, an accurate spatiotemporal study of the crackling noise (in particular repeated earthquakes and swarms) in the Irpinia region should help to better understand the state of health of the fault and to possibly monitor also time variations. In particular, the accurate knowledge of the P- and S-wave arrival times with a large number of records, and refined location of events, allows to study V_p/V_s variations in space and time along the Irpinia fault to monitor fluid injections, which could play a key role in the preparatory phase of a large event (Chiodini et al., 2004; Lucente et al., 2010).

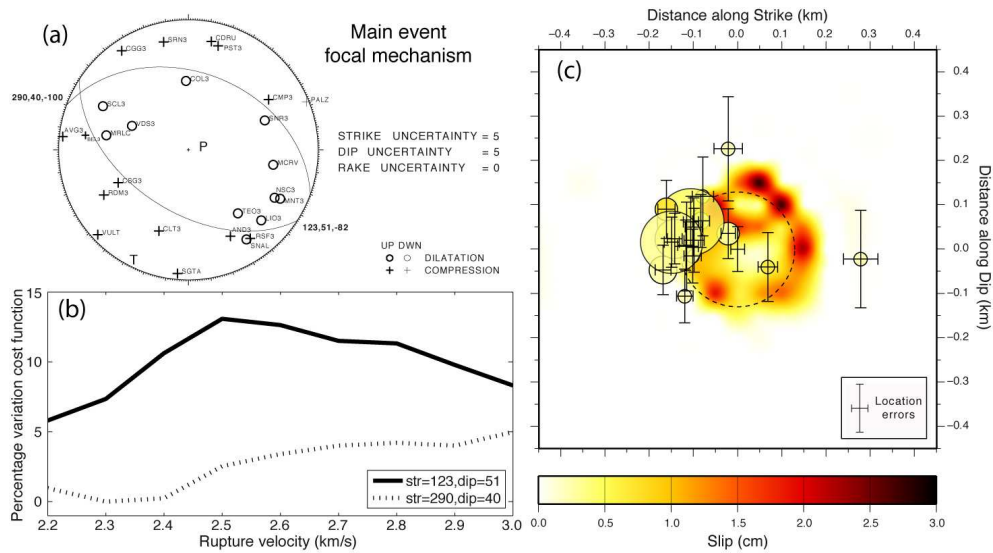


Figure 6.16: (a) Fault plane solutions of the main event. P and T denote the P- and T-axes positions. Open circles and crosses indicate dilatations and compressions, respectively. (b) Percentage variation of the normalized cost function against rupture velocity for both the nodal planes. The absolute minimum is obtained for the nodal plane with strike 290° , and dip 40° , and for a rupture velocity of 2.3 km/s. (c) Slip map of the main event and superimposed distribution of all microearthquakes in the swarm along the strike-dip plane. The dimension of circles is the Madariaga's circular rupture area of events inferred from corner frequencies, while the color of circles indicates the computed average slip Δu . Dotted circle at the center is the rupture area of the main event estimated by the RSTFs durations. Horizontal and vertical location errors are also displayed (Stabile et al., submitted to *Scientific Reports*).

6.3 Conclusions

From the RSTFs it is possible to get knowledge of the seismic source without modeling the propagation between the source and the receiver. In fact, from the observables of RSTFs, that is duration, area and shape, we have obtained:

1. presence of two bumps in the RSTFs of mainshock Mw 6.3;
2. low velocity rupture ($v_r \sim 1.9$ km/s) for $M_w=6.3$ L'Aquila mainshock, as well as, low value of v_r for smallest events of L'Aquila sequence;
3. the observed duration of RSTFs is in inverse proportion to corner frequency;
4. a constant stress-drop and apparent stress scaling of source parameters is observed. The average static stress drop for P- and S- waves is (2.7 ± 1.2) MPa and (3.0 ± 1.7) MPa, respectively. The apparent stress is equal to (2.7 ± 1.2) MPa and (1.7 ± 0.7) MPa for P- and S- waves, respectively.
5. For $M_w = 2.9$ Laviano mainshock the RSTFs were inverted to obtain maps of slip and velocity rupture: the slip distribution shows that the mainshock was principally a circular crack with a slip concentration in the updip and west directions, evidencing a possible directivity effect toward those directions.

Summary

The objective of this work of thesis is the refined estimations of source parameters. To such a purpose we used two different approaches, one in the frequency domain and the other in the time domain.

In frequency domain, we analyzed the P- and S-wave displacement spectra to estimate spectral parameters, that is corner frequencies and low frequency spectral amplitudes. We used a parametric modeling approach which is combined with a multi-step, non-linear inversion strategy and includes the correction for attenuation and site effects.

First of all a resolution test was applied in order to estimate the minimum moment magnitude value above which source parameters can be effectively derived. For this test we consider a microearthquake sequence started on May 25th 2008 in Irpinia region, nearby the village of Laviano (Southern Italy). By the resolution test we have obtained the minimum values of seismic above which we can obtain reliable estimates of source parameters, that is $M_0 \geq 10^{11}$ N·m ($M_w \approx 1$). Then the iterative multi-step procedure was applied to about 700 microearthquakes in the moment range 10^{11} - 10^{14} N·m and recorded at the dense, wide-dynamic range, seismic networks operating in Southern Apennines (Italy). Our results show that the constant-Q attenuation model is preferred to frequency dependent Q-models. Using the retrieved corner frequencies and the Madariaga's (1976) crack model to get the source radius, we computed the variation of the source radius and static stress release with seismic moment. The self-similarity of earthquake source parameters is observed over whole range of seismic moment, with a constant values of static stress drop.

The analysis of the source parameters is often complicated when we are not able to model the propagation accurately. In this case the empirical Green function approach is a very useful tool to study the seismic source properties. In fact the Empirical Green Functions (EGFs) consent to represent the contribution of propagation and site effects to signal without using approximate velocity models.

An EGF is a recorded three-component set of time-histories of a small earthquake whose source mechanism and propagation path are similar to those of the master event. To establish how much is the difference in magnitude between the EGF and master event, a

synthetic test was performed. It has been shown that the EGF optimal magnitude is about 1 units smaller than the mainshock.

Thus, in time domain, the deconvolution method of Vallée (2004) was applied to calculate the source time functions (RSTFs) and to accurately estimate source size and rupture velocity. This technique was applied to 1) large event, that is $M_w=6.3$ 2009 L'Aquila mainshock (Central Italy), 2) moderate events, that is cluster of earthquakes of 2009 L'Aquila sequence with moment magnitude ranging between 3 and 5.6, 3) small event, i.e. $M_w=2.9$ Laviano mainshock (Southern Italy).

From duration and area of RSTFs accurate estimations of source radius, and so corner frequency, seismic moment and rupture velocity were obtained. From estimates of source radius and seismic moment the static stress drop was calculated and the scaling laws were investigated for smallest events of L'Aquila sequence. For these events and also for L'Aquila mainshock a low velocity rupture was estimated in agreement with kinematic inversion models obtained by the inversion combined of teleseismic, accelerometer and GPS data (Balestra et al., 2010, Yano et al., 2009). Moreover, the inversion of RSTFs of Laviano mainshock allowed to constrain the fault plane and provided us with the estimation of the slip distribution, the rupture direction and the average velocity rupture.

References

Abercrombie, R. E. (1995), Earthquake source scaling relationships from -1 to 5 ML using seismograms recorded at 2.5 km depth, *J. Geophys. Res.*, 100, 24,015-24,036.

Abercrombie, R. E. and Rice, J. R. (2005), Can observations of earthquake scaling constrain slip weakening?, *Geophys. J. Int.*, 162, 406-424.

Akaike, H. (1974), A new look at the statistical model identification, *IEEE Trans. Autom. Control*, 6, 716–723.

Aki, K. (1987), Magnitude-Frequency Relation for Small Earthquakes: A Clue to the Origin of f_{max} of Large Earthquakes, *J. Geophys. Res.*, 92(B2), 1349–1355, doi:10.1029/JB092iB02p01349.

Aki (1967), Scaling law of seismic spectrum, *J. Geophys. Res.*, 72, 729-740.

Aki, K., and P. G. Richards (1980), *Quantitative Seismology, Theory and Methods* (2 volumes). W. H. Freeman, San Francisco, 932 pp.

Amato, A., Alessandrini, B., Cimini, G.B., Frepoli, A. and Selvaggi, G., (1993), Active and remnant subducted slabs beneath Italy: evidence from seismic tomography and seismicity, *Ann. Geofis.*, 36, 201-214.

Ammon, C. J., A. A. Velasco, and T. Lay (1993), Rapid estimation of rupture directivity: application to the 1992 Landers ($M_S=7.4$) and Cape Mendocino ($M_S=7.2$), California earthquakes, *Geophys. Res.Lett.* 20, 97–100.

Anderson, J. G. and S. E. Hough (1984), A model for the shape of the Fourier amplitude spectrum of acceleration at high frequencies, *Bull. Seismol. Soc. Am.*, 74, 1969-1993.

Archuleta, R.J., E.C. Cranswick, C. Mueller, and P. Spudich (1982), Source parameters

of the 1980 Mammoth Lakes, California, earthquake sequence, *J. Geophys. Res.*, 87, 4595-4607.

Azimi, S.A., Kalinin A.V., Kalinin V.V. Pivovarov, B.L. (1968), Impulse and transient characteristic of media with linear and quadratic absorption laws, *Izvestiya, Physics of solid Earth*, 88-93.

Balestra, J., M. Chlieh and B. Delouis (2010), Slip inversion of the L'Aquila (Italy) April 9, 2009 earthquake (Mw 6.3) from strong motion, teleseismic, and InSAR data, *Eos Trans. AGU*, 90(52), Fall Meet. Suppl., Abstract, S12A08.

Ben-Menahem, A., and S. J. Singh (1981), *Seismic Waves and Sources*, Springer-Verlag, New York.

Bernard P., and A. Zollo (1989), The Irpinia (Italy) 1980 earthquake: detailed analysis of a complex normal fault. *J. Geophys. Res.* 94, 1631-1648.

Bertero, M. (1989), Linear inverse and ill-posed problems, in *Advances in Electronics and Electron Physics*, Vol. 75, P. W. Hawkes (Editor), Academic, New York, 1–120.

Bertero, M., P. Boccacci, and F. Maggio (1995), Regularization methods in image restoration: an application to HST images, *Int. J. Imaging Systems Tech.* 6, 376–386.

Bertero, M., D. Bindi, P. Boccacci, M. Cattaneo, C. Eva, and V. Lanza (1997), Application of the projected Landweber method to the estimation of the source time function in seismology, *Inverse Problems* 13, 465–486.

Bigi, S., C. Doglioni, and G. Mariotti (2002), Thrust vs normal fault décollements in the Central Apennines, *Boll. Soc. Geol. Ital.*, 1, 161–166.

Bindi D., Spallarossa D., Augliera P., and M. Cattaneo (2001), Source Parameters Estimated from the Aftershocks of the 1997 Umbria–Marche (Italy) Seismic Sequence,

Bull. Seismol. Soc. Am., 91, 448-455; doi: 10.1785/0120000084.

Bindi D., S. Parolai S., Grosser H., C. Milkereit C., and S. Karakisa (2006), Crustal Attenuation Characteristics in Northwestern Turkey in the Range from 1 to 10 Hz, *Bull. Seismol. Soc. Am.*, **96**, 200-214, doi: 10.1785/0120050038.

Bobbio, A., M. Vassallo, and G. Festa (2009), A local magnitude scale for Southern Italy, *Bull. Seismol. Soc. Am.*, 99, 2461–2470, doi: 10.1785/0120080364.

Bouchon M., (1981), A simple method to calculate Green's functions for elastic layered media. *Bull. Seism. Soc. Am.*, 71(4), 959-971.

Brune J.N., (1970), Tectonic stress and the spectra of seismic shear waves from earthquakes. *J. Geophys. Res.* 75, 4997-5009.

Cantore L., V. Convertito, and A. Zollo (2010), Development of a site conditions map for the Campania–Lucania region (Southern Apennines, Italy), *Annals of Geophysics*, 53 (4); doi:837 10.4401/ag-4648.

Chiodini, G., C. Cardellini, A. Amato, E. Boschi, S. Caliro, F. Frondini, and G. Ventura (2004), Carbon dioxide Earth degassing and seismogenesis in central and southern Italy. *Geophys. Res. Lett.* 31(L07615). doi: 10.1029/2004GL019480.

Cirella, A., A. Piatanesi, M. Cocco, E. Tinti, L. Scognamiglio, A. Michelini, A. Lomax, and E. Boschi (2009), Rupture history of the 2009 L'Aquila (Italy) earthquake from non-linear joint inversion of strong motion and GPS data. *Geophys. Res. Lett.*, 36(19), L19304, doi:10.1029/2009GL039795.

Clinton, J., (2004), Modern Digital Seismology - Instrumentation, and Small Amplitude Studies for the Engineering world, *Ph.D. Thesis*.

Courboux, F., M. A. Santoyo, J. F. Pacheco, and S. K. Singh (1997a), The 14

September 1995 (*M* 7.3) Copala, Mexico, earthquake: a source study using teleseismic, regional, and local data, *Bull. Seism. Soc. Am.* 87, 999–1010.

Coutant, O. (1989), Programme de simulation numérique Axitra. *Rapport LGIT*, Grenoble.

Davis L. (1987), *Genetic Algorithms and Simulated Annealing*. Morgan Kaufmann Publishers, London.

D'Agostino, N., S. Mantenuto, E. D'Anastasio, A. Avallone, M. Barchi, C. Collettini, F. Radicioni, A. Stoppini, and G. Castellini (2009), Contemporary crustal extension in the Umbria –Marche Apennines from regional CGPS networks and comparison between geodetic and seismic deformation, *Tectonophysics*, 476 (2009) 3–12.

Deichmann, N. (2006), Local magnitude, a moment revisited, *Bull. Seismol. Soc. Am.* 96, 1267-1277, doi 10.1785/0120050115.

de Lorenzo, S., A. Zollo, and G. Zito (2010), Source, attenuation, and site parameters of the 1997 Umbria-Marche seismic sequence from the inversion of P wave spectra: A comparison between constant QP and frequency dependent QP models, *J. Geophys. Res.*, 115, B09306, doi:10.1029/2009JB007004.

Devoti, R., F. Riguzzi, M. Cuffaro, and C. Doglioni (2008), New GPS constraints on the kinematics of the Apennines subduction, *Earth Planet. Sci. Lett.*, 273, 163–174, doi:10.1016/j.epsl.2008.06.031.

Doglioni, C., F. Mongelli, and G. Pialli (1998), Boudinage of the Alpine belt in the Apenninic back-arc, *Mem. Soc. Geol.*, 52, 457– 468.

L. Elia, C. Satriano and G. Iannaccone (2009), SeismNet Manager - A web application to manage hardware and data of a seismic network. *Seismol. Res. Lett.*, 80(3), doi: 10.1785/gssrl.80.3.420.

Edwards, B., A. Allmann, D. Fäh and J. Clinton. (2010), Automatic Computation of Moment Magnitudes for Small Earthquakes and the Scaling of Local to Moment Magnitude, *J. Geophys. Res.*, 183, 407-420, doi: 10.1111/j.1365-246X.2010.04743.x

Festa, G., and A. Zollo (2006), Fault slip and rupture velocity inversion by isochrone backprojection. *Geophys. Journal International* 166(2), 745-756. doi:10.1111/j.1365-246X.2006.03045.x

Fletcher, J. B., J. Boatwright, L. C. Haar, T. C. Hanks, and A. McGarr (1984), Source parameters for aftershocks of the Oroville, California, earthquake, *Bull. Seismol. Soc. Am.*, 74, 1101-1123.

Fracassi, U., and G. Valensise (2003), The "layered" seismicity of Irpinia (Southern Italy): Important but incomplete lessons learned from the 23 November 1980 earthquake, in *The Many Facets of the Seismic Risk, Proceedings of the Workshop on Multidisciplinary Approach to Seismic Risk Problem*, edited by M. Pecce et al., pp. 46 - 52, CRdC AMRA, S. Angelo dei Lombardi.

Fukuyama, E., and K. Irikura (1986), Rupture process of the 1983 Japan Sea (Akita-Oki) earthquake using a waveform inversion method, *Bull. Seism. Soc. Am.* 76, 1623–1640.

Goldberg D. E. (1989), *Genetic algorithms in search, optimization and machine learning*. Addison-Wesley Publishing Company, New York.

Hanks, T. C., and H. Kanamori (1979), A moment magnitude scale, *J. Geophys. Res.*, 84, 2348 -2350.

Hanks, T. C. (1981), The corner frequency shift, earthquake source models and Q, *Bull. Seism. Soc. Am*, 71, 597-612.

Hartzell, S. H. (1978), Earthquake aftershocks as Green's functions, *Geophys. Res. Lett.* 5, 1–4.

Hough, S. E. (1997), Empirical Green's function analysis: taking the next step, *J. Geophys. Res.*, 102(B3), 5369–5384.

Ide, S., and G. C. Beroza (2001), Does apparent stress vary with earthquake size?, *Geophys. Res. Lett.*, 28, 3349-3352.

Ide S, Beroza GC, Prejean SG, Ellsworth WL (2003), Apparent Break in Earthquake Scaling Due to Path and Site Effects on Deep Borehole Recordings, *J. Geophys. Res.*, 108, B5, 2271, doi:10.1029/2001JB001617

Ihmlé, P. F. (1996), Frequency-dependent relocation of the 1992 Nicaragua slow earthquake: an empirical Green's function approach, *Geophys. J. Int.* 127, 75–85.

Janert K. P. (2009), Gnuplot in Action: Understanding Data with Graphs pp. 396 *Manning Publications Co.*

Kanamori, H., and Anderson, D. (1975), Theoretical basis of some empirical relations in seismology. *Bull. Seismol. Soc. Am.* 65, 1073-1095.

Keilis-Borok, V. I. (1959), On the estimation of the displacement in an earthquake source and of source dimensions, *Ann. Geophys.*, 12, 205-214.

Kjartansson, E. (1979), Constant Q Wave Propagation and Attenuation, *J. Geophys. Res.*, 84(B9), 4737–4748, doi:10.1029/JB084iB09p04737.

Lawson, C., and R. Hanson (1974), *Solving Least Square Problems*, Prentice Hall, New York.

Lin, G, Shearer, P.M. and E. Hauksson (2007), Applying a three-dimensional velocity model, waveform cross correlation, and cluster analysis to locate southern California seismicity from 1981 to 2007 *J. of Geophys. Res.*, 112(B12309), doi:10.1029/2007JB004986.

Lomax, A., J. Virieux, P. Volant, and C. Berge (2000), Probabilistic earthquake location in 3D and layered models: Introduction of a Metropolis-Gibbs method and comparison with linear locations, in *Advances in Seismic Event Location*, Thurber, C.H., and N. Rabinowitz (eds.), Kluwer, Amsterdam, 101-134

Lucente, F. P., P. De Gori, L. Margheriti, D. Piccinini, M. Di Bona, C. Chiarabba, N. P. Agostinetti (2010), Temporal variation of seismic velocity and anisotropy before the 2009 MW 6.3 L'Aquila earthquake, Italy. *Geology* 38 (11), 1015-1018. doi: 10.1130/G31463.1

Madariaga, R. (1976), Dynamics of an expanding circular fault, *Bull. Seismol. Soc. Am.*, 66, 639-666.

Madariaga, R. (2009), Earthquake scaling laws, in *Encyclopedia of Complexity and Systems Science*, R. A. Meyers ed., Part 5, 2581-2600, Springer, New York, DOI: 10.1007/978-0-387-30440-3_156

Maggi, C., A. Frepoli, G. B. Cimini, R. Console, and M. Chiappini (2008), Recent seismicity and crustal stress field in the Lucanian Apennines and surrounding areas (Southern Italy): Seismotectonic implications, *Tectonophysics*, 463, 130-144, doi:10.1016/j.tecto.2008.09.032.

Marquardt, D. (1963), An Algorithm for Least-Squares Estimation of Nonlinear Parameters, *SIAM Journal on Applied Mathematics* 11: 431–441. doi:10.1137/0111030.

Matrullo, E., O. Amoroso, R. De Matteis, C. Satriano, and A. Zollo (2011), 1D versus 3D velocity models for earthquake locations: a case study in Campania-Lucania region (Southern Italy). *Geophysical Research Abstracts* 13, EGU2011-9305, 2011

McGarr, A. (1986), Some observations indicating complications in the nature of earthquake scaling. In: Das, S., Boatwright, J. and Scholz, C.H., Editors, 1986. *Earthquakes Source Mechanics Am. Geophys. Union Monogr.*, p. 37.

Menke W. (1989), *Geophysical Data Analysis: Discrete Inverse Theory*. Academic Press, *International Geophysics series*, 45.

Molnar, P., B. E. Tucker, and J. N. Brune (1973), Corner frequencies of P and S waves and models of earthquake source, *Bull. Seismol. Soc. Am.*, 63, 2091-2104.

Montone, P., A. Amato, and S. Pondrelli (1999), Active stress map of Italy, *J. Geophys. Res.*, 104, 25,595– 25,610, doi:10.1029/1999JB900181.

Montone, P., M. T. Mariucci, S. Pondrelli, and A. Amato (2004), An improved stress map for Italy and surrounding regions (central Mediterranean), *J. Geophys. Res.*, 109, B10410, doi:10.1029/2003JB002703.

Mori, J., and A. Frankel (1990), Source parameters for small events associated with the 1986 North Palm Springs, California, earthquake determined using empirical Green functions, *Bull. Seism. Soc. Am.* 80, 278–295.

Morozov, I.B. (2008), Geometrical attenuation, frequency dependence of Q, and the absorption band problem, *Geophys. J. Int.*, 172, 239-252. DOI: 10.1111/j.1365-246X.2008.03888.x.

Mueller, C. S. (1985), Source pulse enhancement by deconvolution of an empirical Green's function, *Geophys. Res. Lett.* 12, 33–36.

Nadeau, R. M. and T. V. McEvilly (1999), Fault slip rates at depth from recurrence intervals of repeating microearthquakes, *Science*, 285, 718–721.

Nelder, J.A., and Mead, R. (1965), A simplex method for function minimization. *Computer Journal*, 7, p. 308.

Orefice, A. and A. Zollo (2010), *European Seismological Commission Abstracts*, ES5/P31/ID134, 32nd ESC GA Montpellier, France

Prieto, G:A., Shearer, P.M., Vernon, F.L. and Debi K. (2004), Earthquake source scaling and self-similarity estimation from stacking P and S spectra. *J. Geophys.Res.*, 109 (B08310), doi:10.1029/2004JB003084.

Reasenber, P., and D. Oppenheimer (1985), FPFIT, FPLOT and FPPAGE: Fortran computer programs for calculating and displaying earthquake fault plane solutions. *U.S. Geol. Surv., Open File Report*, 85-739.

Reed, C. (1989), Linear least-squares fits with errors in both coordinates, *Am. J. Phys.* 57 (7), 642-646.

Savage, J. C. (1966), Radiation from a realistic model of faulting, *Bull Seism. Soc. Am.* 56: 577–592.

Savage, J. C. (1974), Relation between P- and S-wave corner frequencies in the seismic spectrum, *Bull Seism. Soc. Am.* 64, 1621-1627.

Scandone, P. (1979), Origin of the Tyrrhenian Sea and Calabrian Arc., *Boll. Soc. geol. ital.*, 98, 27-34.

Schwartz, S. Y. (1999), Noncharacteristic behavior and complex recurrence of large subduction zone earthquakes, *J. Geophys. Res.* 104, 23,111-23,125.

Sato, T., and T. Hirasawa (1973), Body wave spectra from propagating shear cracks, *J. Phys. Earth* 21, 415–431.

Selvaggi, G. (1998), Spatial distribution of horizontal seismic strain in the Apennines from historical earthquakes, *Ann. Geofis.*, 41, 241–251.

Serpelloni, E., M. Anzidei, P. Baldi, G. Casula, and A. Galvani (2005), Crustal velocity and strain-rate fields in Italy and surrounding regions: new results from the analysis of permanent and non-permanent GPS networks, *Geophys. J. Int.*, 161, 861 – 880,

doi:10.1111/j.1365-246X.2005.02618.x.

Stabile, T. A., C. Satriano, A. Orefice, G. Festa, and A. Zollo (2011), Anatomy of an earthquake crackling sequence on an active normal fault, submitted to *Scientific Reports*

Toksoz, M.N., D.H. Johnson and A. Timur (1979), Attenuation of seismic wave in dry and saturated rocks-1. Laboratory experiments, *Geophysics*, 44, 681-690.

Vallée, M. (2004), Stabilizing the empirical Green function analysis: development of the projected Landweber method, *Bull. Seism. Soc. Am.* 94, 394–409.

Valensise, G., A. Amato, P. Montone, and D. Pantosti (2003), Earthquakes in Italy: Past, present and future, *Episodes*, 26(3), 245-249.

Velasco, A. A., C. J. Ammon, and T. Lay (1994), Empirical Green function deconvolution of broadband surface waves: rupture directivity of the 1992 Landers, California ($M_w=7.3$), *Bull. Seism. Soc. Am.* 84, 735–750.

Walters, R. J.; J. R. Elliott, N. D'Agostino, et al. (2009), The 2009 L'Aquila earthquake (central Italy): A source mechanism and implications for seismic hazard. *Geophys. Res. Lett.* 36, L17312, doi:10.1029/2009GL039337.

Warren, L. M., and P. M. Shearer (2002), Mapping lateral variations in upper mantle attenuation by stacking P and PP spectra, *J. Geophys. Res.*, 107(B12), 2342, doi:10.1029/2001JB001195.

Weber, E., V. Convertito, G. Iannaccone, A. Zollo, A. Bobbio, L. Cantore, M. Corciulo, M. Di Crosta, L. Elia, C. Martino, A. Romeo and C. Satriano (2007), An advanced seismic network in the southern Apennines (Italy) for seismicity investigations and experimentation with earthquake early warning, *Seismol. Res. Lett.*, 78, 622.

Winkler, K.W., and A. Nur (1979), Pore fluids and attenuation in rocks, *Geophys. Res.*

Lett., 6, 1-4.

Yano, T. E., G. Shao, Q. Liu, C. Ji and R. J. Archuleta (2009), Finite Fault Kinematic Rupture Model of the 2009 Mw6.3 L'Aquila Earthquake from inversion of Strong Motion, GPS and InSAR Data. *AGU*, Fall Meeting 2009, Abstract S34A-02.

Zollo, A., A. Orefice and V. Convertito (2011), Scaling Relationships for Earthquake Source Parameters Down to Decametric Fracture Lengths, submitted to *J. Geophys. Res.*